Shape Controlled Plasmonic Nanostructures for Light Harvesting Applications

By

William R. Erwin

Dissertation

Submitted to the Faculty of the

Graduate School of Vanderbilt University

in partial fulfillment of the requirements

for the degree of

DOCTOR OF PHILOSOPHY

in

Chemical Engineering

May, 2017

Nashville, Tennessee

Approved:

Rizia Bardhan, Ph.D.

G. Kane Jennings, Ph.D.

Paul E. Laibinis, Ph.D.

Cary L. Pint, Ph.D.

To Mom and Dad, thank you for always believing in me.

ACKNOWLEDGMENTS

This dissertation is the culmination of four years of work, and it would not have been possible without the help and support of many people. First, I would like to thank my research advisor, Professor Rizia Bardhan, who has provided me with a wealth of resources, taught me valuable lessons, and helped me develop as a scientist. I am thankful for the opportunity to to study under her guidance and be a part of her research team. I am thankful to the members of my Ph.D. committee, Professors Kane Jennings, Paul Laibinis, and Cary Pint, their insights into my research have been helpful towards my growth as a researcher.

To all of the chemical engineering department staff, thank you. None of the research that I have done would have been possible without the stable foundation that Mary Gilleran, Rae Uson, Julie James, Angie Pernell, and Mark Holmes have maintained through the years.

To the current and former members of the Bardhan Group, thank you. The conversations I've had with Joe Webb, Holly Zarick, May Ou, Naiya Soetan, and Eric Talbert have offered valuable insights and driven my work forward.

This work would not have been possible without financial support from the National Science Foundation, under the Graduate Research Fellowship (1445197) and EPSCOR (EPS1004083).

Finally, I would like to thank my friends and family. To my friends, I am not the same person I was when I started at Vanderbilt and I owe much of the personal the growth I've experienced to you. To my family, I never would have made it here without your support, thank you for always being there for me; everything I have and will achieve is a direct result of your love and encouragement.

TABLE OF CONTENTS

LIST OF TABLES

LIST OF FIGURES

Chapter 1

INTRODUCTION

1.1 Motivation

As the modern economy increasingly moves away from fossil fuels, it is imperative that alternative fuel and electricity sources are developed. In addition to the depletion of oil, natural gas, and coal reserves, greenhouse gas emissions from the production and consumption of fossil fuels are hastening the development of one of the greatest challenges of the 21st century, climate change. If left unabated, greenhouse gas emissions could cause a 4 °C rise in average global temperatures by 2100, thereby devastating the global economy. [1, 2] Clean energy in the U.S. is produced from multiple sources, including wind energy, biofuels, geothermal and hydropower. According to a report by the U.S. Energy Information Administration, commercial solar cells have gained an increasing share of the renewable energy market, producing 6.7% of the total renewable energy in the United States in 2016, up from 1.1% in 2006.[3] It is important to note that the cost of commercially installed solar energy is largely contributed by factors other than the solar module. In a 2013 report by the Rocky Mountain Institute, it was shown in the U.S. that the solar module contributed $<$ 17% of the cost per area of installed solar, with the remainder of the cost contributed from soft costs such as installation, regulatory requirements, and financing, as well as additional hardware and inverter costs. Because of the relatively low cost of solar modules in relation to ancillary costs, it is paramount to maximize the power output per area for commercially viable solar cells.

There are many approaches to improving the light harvesting efficiency of photovoltaic systems including multi-junction solar cells and solar concentrators, however, we investigate the improvement of light harvesting by the incorporation of plasmonic nanostructures

into solar cells. Plasmon enhancement can be used to improve the light absorption of a wide variety of solar harvesting devices, the mechanisms by which will be discussed in detail in Section 1.3.

1.2 Third Generation PV

1.2.1 Organic Photovoltaics

Organic photovoltaics (OPVs) made from solution processed organic polymer semiconductors have attracted much attention since 2001, when Shaheen et al. first published a power conversion efficiency (PCE) of ~2.5%.[4] Toshiba Inc. has since produced a single junction organic thin film cell with a PCE of 11.2%[5, 6], bringing OPVs closer to the realm of commercially viable energy conversion technology. A major advantage to OPVs is their ability to be made flexible, as they are not inherently brittle like leading crystalline solar cells; flexibility could provide a route to implementation of solar technology in apparel and other consumer goods.[7, 8] Additionally, OPVs are semitransparent, and can easily be incorporated into consumer products, due in part to the non-hazardous materials with which they are made. Currently, commercially printed cells with efficiencies in the range of ~1.5-2.5% are available.[9] Krebs et al. developed a process for aqueous processing of OPVs using roll-to-roll methods, and achieved PCEs of up to ~0.7%.[10, 11] A distant goal for the field is to make the manufacture of organic photovoltaics as simple, inexpensive, and unobtrusive as applying paint to a wall.

One major barrier to OPVs commercial viability lies in the low efficiency of commercial modules. Improved PCE is paramount to the cost effectiveness of OPV materials, and may be accomplished, in part, by plasmon enhancement. Plasmon enhancement provides a universal route applicable to the whole family of OPV materials that can significantly boost the optical absorption and carrier generation per unit of OPV absorbing material. Through small additions of metal nanoparticles to OPVs (< 1 wt%), the PCE of OPVs can be signif-

icantly enhanced, enabling thin film architectures compatible with scalable manufacturing routes and improved viability for integration.

In a recent review, Yu et al. outlines the criteria to consider when designing a polymer for use in OPVs: *i)* low bandgap energy to facilitate efficient light absorption, *ii)* proper energy level match between the LUMO levels of the electron donor and acceptor to overcome exciton binding energy, *iii)* balanced charge carrier mobility for efficient charge transport and *iv)* optimized energy difference between the HOMO level of the donor polymer and the LUMO level of the acceptor molecule in order to maximize V_{oc}.[12] The full geometry of an OPV is represented in the top panel of Figure 1.1a. An anode, typically a transparent conductive oxide (TCO) is the base (100-150 nm), followed by a thin (10-100 nm) hole transport layer (typically PEDOT:PSS or MoO_3). The active layer (80-200 nm) consists of an electron donor and an electron acceptor material in a bulk heterojunction architecture (BHJ). An electron transporting layer (1-10 nm) is coated on top of the active layer, which is then capped with a metal cathode (100-150 nm), typically Al or Ag.

The bulk heterojunction (BHJ), as represented in Figure 1.1a is the prevailing geometry used in research grade organic photovoltaics. The BHJ maximizes the contact area between the electron donor and acceptor molecules, while remaining solution processable. High surface areas have been observed in BHJs of donor/acceptor pairs, which is necessary in OPVs, as polymers typically have short exciton diffusion lengths (~10-20 nm).[13] The lower panel of Figure 1.1a schematically shows the process of charge generation in an OPV; first, a bound exciton is excited by an incoming photon (1), the exciton then diffuses through the donor material until it either recombines or finds an interface with the acceptor material (2), where the HOMO energy of the acceptor material provides the necessary energy for dissociation (3). From here, the charge carriers percolate to the current collector where they may be used to perform work (4).

Figure 1.1b further illustrates the charge dissociation process. When a photon of greater energy than the donor bandgap ($E_{g,D}$) excites a donor molecule, an electron moves to the

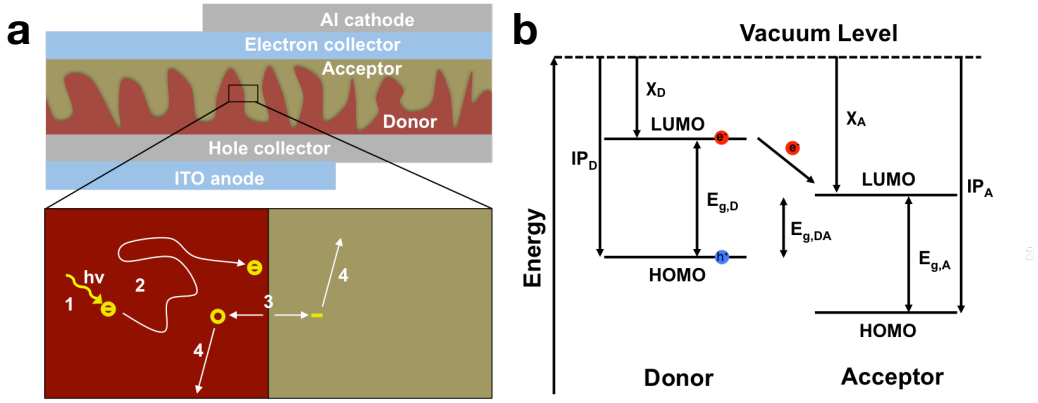

Figure 1.1: (a) Schematic representation of exciton generation and dissociation in a bulk heterojunction OPV. (b) Band diagram of generic donor acceptor system.

lowest unoccupied molecular orbital (LUMO) of the species, remaining bound in an exciton. When the exciton comes in contact with the acceptor molecule, it readily dissociates into free carriers under the condition that $IP_D - U_C < \chi_A$, where IP_D is the ionization potential, χ_A is the acceptor electron affinity, and U_C is the Coulomb energy of the separated species.[14] The effective bandgap of the donor/acceptor system is given by $E_{g,DA}$ - this determines the maximum voltage achievable by the solar cell.

When a photon of sufficient energy strikes an electron donating molecule in an OPV, an exciton is formed. Unlike traditional photovoltaics (PVs) which have a high refractive index (~10-12), organic photovoltaics are made of materials with a much lower refractive index (~3-4). Because of this low refractive index, the bound exciton must overcome a much higher dissociation energy barrier than do excitons in a higher refractive index medium. Owing to this high required dissociation energy, a homojunction as is found in traditional PVs is not a feasible option, and so a heterojunction is used. Typically, a fullerene based acceptor molecule is used, though non-fullerene based acceptor systems have been reported.[15]

1.2.2 Mesoporous Solar Cells

In addition to solid state photovoltaic systems, photoelectrochemical (PEC) cells have been explored for electricity production. An added advantage of PEC systems is that they can be used for direct clean fuel production via redox reactions of consumable electrolytes. The concept of PEC has been studied for various applications since the discovery of the photovoltaic effect in 1839.[16] In a photoelectrochemical system, photons hit a semiconducting electrode, generating charge carriers (e^-/h^+ pairs). Because catalysis is an inherent part of a photoelectrochemical system, high surface area to facilitate reactions between the light absorbing species and the redox electrolyte, typically mesoporous photoelectrodes are used to accomplish this.[17] For an n-type semiconductor, holes migrate to an electrolyte solution in contact with the electrode and perform a redox reaction, the electrons are forced around an external circuit to a counter electrode to participate in the opposite redox reaction, as illustrated in Figure 1.2. For a p-type semiconductor, the opposite is true. Two types of PEC cells are being heavily investigated today: *(i)* cells that generate hydrogen from the cleavage of water which can be used as a clean, portable fuel source,[18] and *(ii)* regenerative type cells that produce current from sunlight, commonly known as dye sensitized solar cells (DSSCs).[19] Titanium dioxide is commonly used in both systems for it's long term stability in a corrosive electrolyte environment.[20] TiO_2 has a relatively high band-gap (3.2 eV) which has an absorption threshold of 460 nm, while other materials are used for PEC solar energy harvesting such as WO_3 and Fe_2O_3, they are often limited by stability.[21, 20]

Because TiO_2 has a high band gap, PEC devices often consist of mesoporous TiO_2 sensitized with molecules or structures which have a high optical cross section and can couple absorbed light into the semiconducting backbone. Dye sensitized solar cells produce electricity using a colloidal semiconductor layer sensitized with dye, an I^- / $I_3{}^-$ redox mediator, and a charge collecting layer (usually platinum) to complete a redox reaction under solar irradiation.[19] Since their conception in 1991, dye sensitized solar cells (DSSCs)

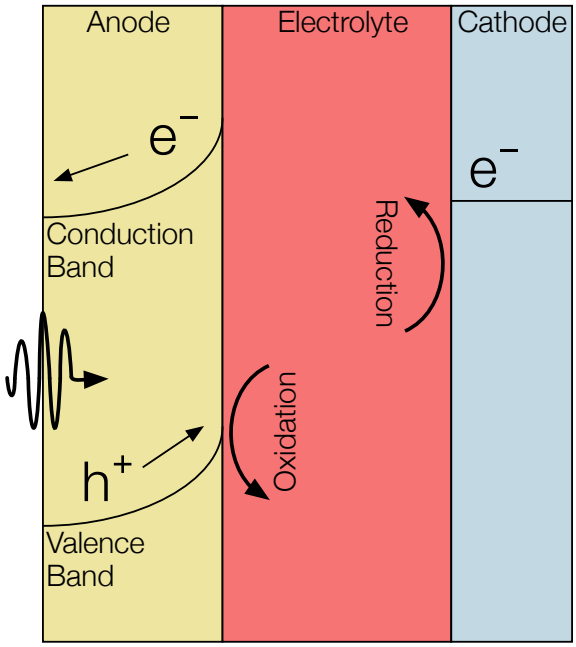

Figure 1.2: Schematic representation of a photoelectrochemical cell.

have reached power conversion efficiencies of up to 11.9%.[5] In addition to poor light absorption by PEC devices, a major barrier in large scale PEC device production lies in the use of the noble metal platinum as a counter electrode.[22] Typically, platinum salt is brushed onto a transparent conductive oxide (TCO) layer and calcined into platinum metal, however, a number of materials have been explored as an alternative to platinum including conductive polymers,[23] mesoporous semiconductors,[24] carbon nanotubes,[25] and graphene.[26, 27, 28, 29] Carbon materials have taken a leading role in the search for a counter electrode material due to their high conductivity, excellent catalytic activity, and is feasibility for large scale production.[30, 25, 31, 32, 24, 23, 33, 34]

1.3 Mechanisms of Plasmon Enhancement

Localized Surface Plasmon Resonances (LSPRs) in metal nanostructures give rise to a collection of optical and electronic effects, processes that occur during the excitation and subsequent decoherence of a plasmon and ultimately contribute to enhanced photonic effects in photovoltaics (PVs). Plasmonic enhancement in solar devices is attributed to *(i)*

radiative effects, in which the LSPR relaxes and re-radiates light into the absorptive layer or the metal nanostructures act as a secondary absorber that enhances local electric fields, and *(ii)* non-radiative effects where the LSPR relaxes and energy is subsequently transferred to vicinal semiconductor, enhancing the current generation. In non-radiative processes, metal nanostructures essentially act as a direct sensitizer in which charge carriers are directly injected into a semiconductor. This section will explain the four mechanisms of plasmonic enhancement shown in Figure 1.3, including light scattering and electromagnetic fields categorized within radiative effects, and hot electron transfer (HET) and plasmon resonant energy transfer (PRET) which fall under non-radiative effects.

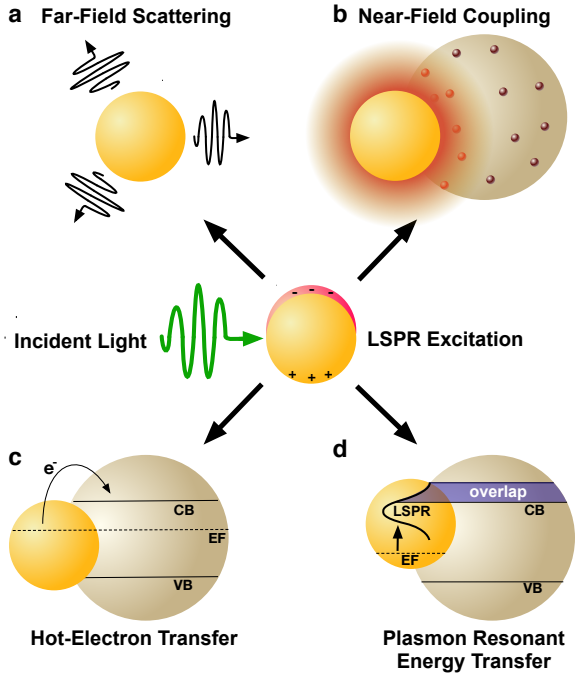

Figure 1.3: Schematic illustration of plasmon enhancement mechanisms of radiative effects (a) far-field scattering and (b) near-field coupling; and nonradiative effects: (c) hot-electron transfer, and (d) plasmon resonant energy transfer. The small gold spheres represent a plasmonic nanostructure, and the large tan spheres represent vicinal semiconductor.

1.3.1 Radiative Effects

LSPRs of metal nanostructures have finite lifetimes following which they decay either radiatively by emitting a photon, or nonradiatively by generating electron-hole pairs.[35, 36, 37] The radiative decay process either gives rise to electromagnetic fields in the nanostructures near-field or light scattering into the nanostructures far-field. Radiative effects are best understood as a dipole-dipole coupling between the metal nanoparticle dipolar fields with the molecule or sensitizer dipole. The metal-molecule radiative coupling is proportional to r^{-3}, where r is the distance from the molecule to the nanostructure. At the plasmon resonance however, radiative fields follow r^{-6} dependence and may far exceed unity.[38, 39, 40, 41, 42] In this section, we discuss the basic concepts and mechanisms of plasmonic enhancement in PVs by radiative processes. Light incident on metal nanostructures with a sufficiently high albedo is scattered into the far-field; depending on geometric and material properties of the particle, the scattering cross section may be up to an order of magnitude larger than the physical cross-section of the nanostructure.[35] This far-field scattered light can ultimately be reabsorbed by the active material, enabling enhanced light absorption even at distances of several hundred nanometers. Photons scattered from each nanostructure can also encounter multiple scattering from proximal nanostructures in the far-field, which ultimately increases the total light trapped within a solar cell.[43, 44, 45] Further, by tuning the LSPR to wavelengths complementary to the active material's absorption, nanostructures can be designed to capture solar photons not otherwise absorbed.[46, 47] Light scattering properties of metal nanostructures are a function of their size and are best understood by Mie theory.[48, 49, 50, 51] Mie theory is the simplest analytical solution of Maxwells equations and describes the extinction behavior of spherical metal nanoparticles when excited with an incident electric field. For a metal nanosphere with radius a in a dielectric medium, where the permittivity for the metal and medium are given by ε_{metal} and ε_{medium}, respectively, the scattering cross section (σ_{scat}) is given by:

$$\sigma_{scat} = \frac{8\pi}{3} k^4 a^6 \left| \frac{\varepsilon_{metal} - \varepsilon_{medium}}{\varepsilon_{metal} - 2\varepsilon_{medium}} \right|^2 \quad (1.1)$$

where $k = 2\pi/\lambda$. Since σ_{scat} scales with a^6, metal nanoparticles with sizes a >30 nm are ideal for coupling far-field scattered light into absorbing materials, resulting in enhanced light harvesting.[52] We have calculated absorption and scattering cross-sections of spherical Au nanoparticles to demonstrate this size effect. Figure 1.4a shows that the percent light scattered from nanoparticles monotonically increases with size while the amount of light absorption decreases.

At the crossover size of ~90 nm for spherical Au nanoparticles, the amount of light absorbed and scattered is equivalent, indicating nanoparticle size can be tuned to achieve desired absorptive and scattering properties for maximum solar harvesting. Beyond the size of metal nanostructures, shape also controls the far-field scattered light attributed to the enhanced polarizability, or ability to polarize incoming light, of the nanostructures (Figure 1.4b).[53, 54, 55, 56] The effect of polarizability is particularly dominant for non-spherical nanostructures with sharp edges and corners such as cubes, pyramids, and octahedrons, as well as layered concentric nanostructures where the polarizability is enhanced at the metal/dielectric interface of each layer.[57] Further, light scattering characteristics are affected by the composition of nanostructures where Ag has stronger radiative properties due to less Ohmic losses than Au (Figure 1.4b). This is best described by the complex dielectric functions of bulk Ag and Au which consists of a real (Figure 1.5a) and imaginary (Figure 1.5b) part. The real part of the dielectric function (ε_1) determines the polarization response and scales with carrier concentration in the metal. The imaginary part of the dielectric function (ε_2) determines the optical losses including interband and intraband losses. For Au, intraband or Drude losses are high in the near-infrared and lower in the visible. Alternatively, interband losses in Au are high at shorter wavelengths. The smaller imaginary dielectric function of Ag across all wavelengths implies lower optical losses (i.e. plasmon damping), which results in higher scattering efficiency and narrower plasmon

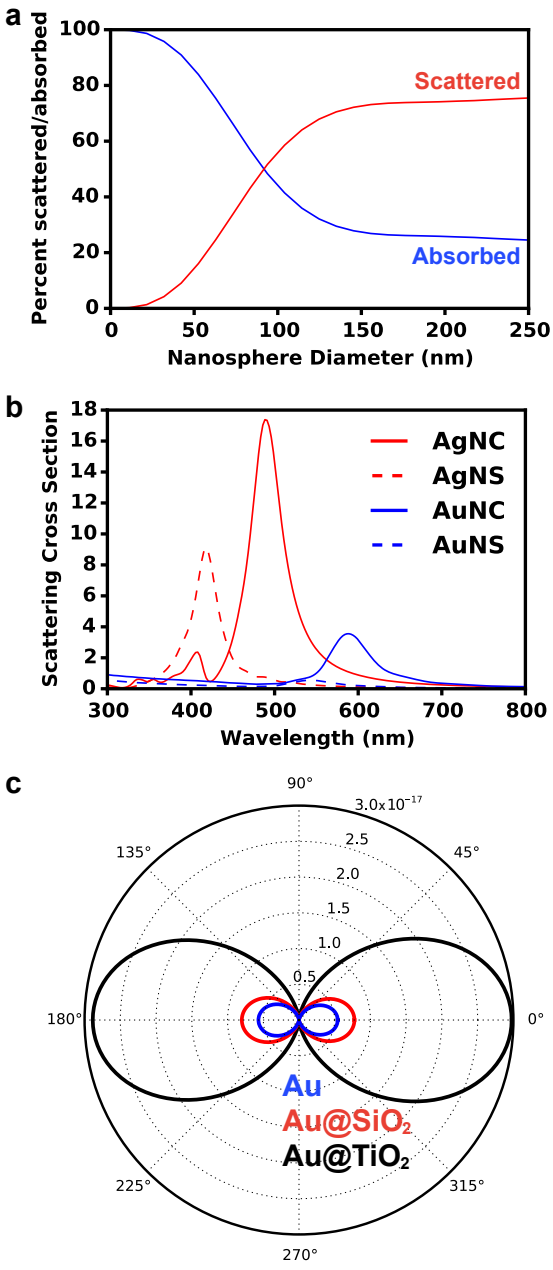

Figure 1.4: (a) Ratio of percent light scattered to light absorbed calculated as a function of Au nanosphere diameter integrated from 300-800 nm. (b) Calculated scattering cross sections of 50 nm Au and Ag nanospheres (NS) and nanocubes (NC) indicate that both shape and composition control nanoparticle albedo. (c) Calculated angular scattering of 50 nm Au nanosphere bare, with a 10 nm SiO_2 coating, and with a 10 nm TiO_2 coating. All calculations were performed in Lumerical FDTD Solutions.

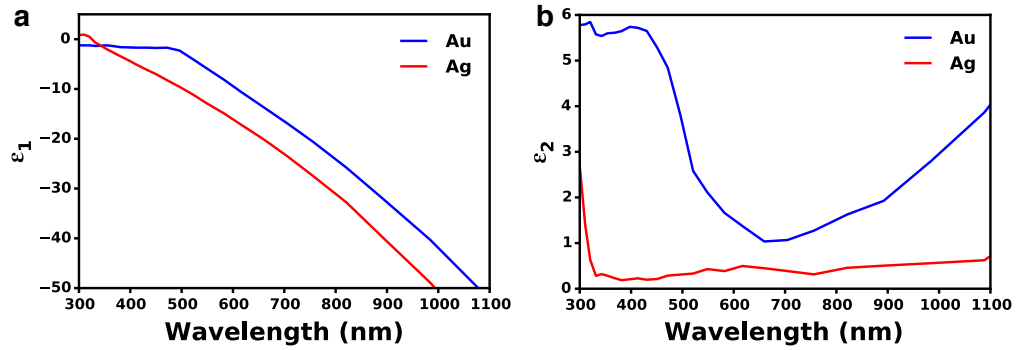

Figure 1.5: (a) Real part of the dielectric function for Au and Ag. (b) Imaginary part of the dielectric function of Au and Ag. Data adapted from Ref. [59].

linewidths.[58, 59, 60, 61] This fundamental difference in the optical behavior of Au and Ag has been extensively harnessed in plasmonic sensing, and more recently applied solar enhancement where Ag has shown stronger enhancement in carrier generation.[62, 63, 64]

Finally, far-field effects may be tuned as a function of the permittivity of the medium (ε_{medium}) surrounding the metal nanostructures.[65, 66, 67, 68] A higher ε_{medium} *(i)* red-shifts the LSPR frequency enabling capture of solar photons where the sensitizer poorly absorbs, and *(ii)* enabling preferential scattering in targeted directions.[69] Calculated angular scattering (Figure 1.4c) of 50 nm Au nanoparticles uncoated, and coated with 10 nm SiO_2, and TiO_2 demonstrates $>3\times$ light scattering for TiO_2 coated nanoparticles. The dielectric constant of TiO_2 is ~6.8 whereas that of SiO_2 is ~2.1. The red-shift in LSPR frequency, λ_p, with increase in ε_{medium} is best understood by the Drude approximation for quasi-static metal nanoparticles, given by:

$$\lambda_p = \lambda_{p,b}\sqrt{2\varepsilon_{medium}+1} \tag{1.2}$$

where $\lambda_{p,b}$ is the bulk plasmon wavelength. Further, the sensitivity of the scattering cross section, σ_{scat}, to ε_{medium} can be understood from Mie theory, given by:

$$\sigma_{scat} = \frac{32\pi^4\varepsilon_{medium}^2 V^2}{\lambda^4}\frac{(\varepsilon_1-\varepsilon_{medium})^2+(\varepsilon_2)^2}{(\varepsilon_1+\varepsilon_{medium})^2+(\varepsilon_2)^2} \tag{1.3}$$

where V is the nanoparticle volume, and shows σ_{scat} scales with ε^2_{medium}.

The interaction of plasmonic nanostructures with incident light results in local enhancement of electromagnetic fields, defined as near-fields, in the immediate vicinity of the nanostructure. Metal nanostructures integrated in PVs function as nanosized light concentrators focusing incident light on the metal surface within a small mode volume; the intensities of these fields are typically orders of magnitude higher than the incident light. Therefore, one can envision nanostructures as a secondary light source increasing the photon flux and the overall light absorbed by the solar cell. Absorbing materials in the proximity of the nanostructures directly couple with the strong near-fields and the resulting plasmon-molecule coupling, increasing the electron-hole pair generation.

Electromagnetic near-fields at the plasmon resonance decay proportional to r^{-6}, where r is the distance from the nanostructure, and typically extend $<$50 nm from the nanostructure surface (Figure 1.6a). Analogous to far-field scattering, the near-fields generated by the LSPR are governed by the metal nanostructure morphology and composition.[52, 55, 56] Non-spherical nanostructures with sharp features, such as nanocubes, generate a high concentration of charges localized at the edges and corners, attributed to the lightning-rod effect.[70, 71] Finite difference time domain (FDTD) simulations demonstrate the impact of nanostructure morphology and composition on the local electromagnetic field intensities at the plasmon resonance (Figure 1.6b-e). These intense fields in nanocubes decay slower and extend much farther than their spherical counterparts (Figure 1.6b-e). The lightning-rod effect was first reported by Gersten and Nitzan,[72] and then by Liao and Wokaun[73] to describe the fields localized at the tips of prolate ellipsoids. Liao et al. defined the lightning-rod factor, γ, given by:

$$\gamma = \frac{3}{2}\frac{a^2}{b}(1 - A_a) \tag{1.4}$$

where A_a is the depolarization factor of the ellipsoid, a and b are the dimensions of the long axis and short axis respectively. For a nanosphere γ =1, for a prolate ellipsoid with

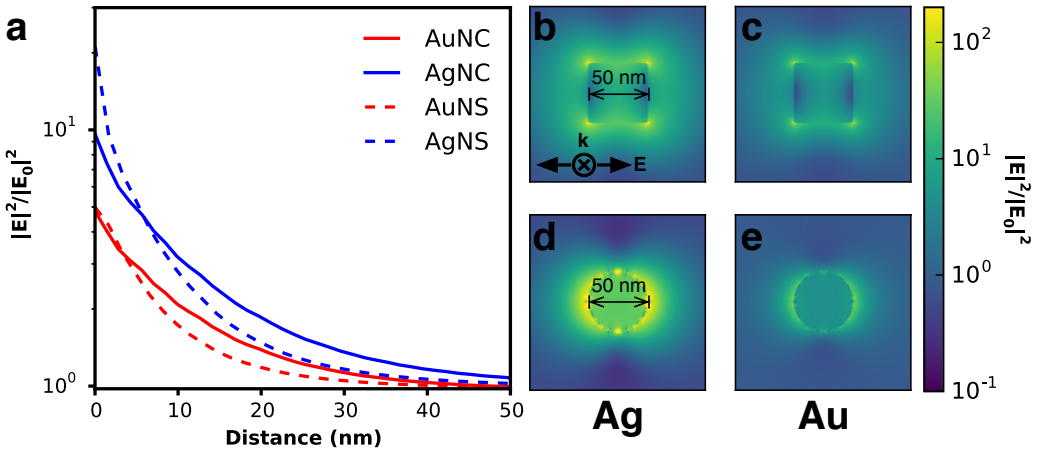

Figure 1.6: (a) Calculated near field enhancement as a function of distance from the particle surface averaged over the 300-800 nm spectral range; values are averaged over the x, y, and z planes intersecting the particle. Near field profiles at peak plasmon resonance for (b) Ag nanocube at 490 nm, (c) Au nanocube at 580 nm, (d) Ag nanosphere at 420 nm, and (e) Au nanosphere at 530 nm are shown. All calculations performed in Lumerical FDTD Solutions.

aspect ratio 3:1 $\gamma = 12$, and for an ellipsoid with aspect ratio 4:1 $\gamma = 22$. The lightning rod effect can be extended to other anisotropic shapes and ultimately explains the higher efficiencies observed when PVs are integrated with non-spherical nanostructures. Near-field effects are also stronger for Ag relative to Au (Figure 1.6a) due to the wavelength-dependent behavior of the real and imaginary dielectric functions of the metals as shown in Figure 1.5. We note that a limitation of radiative enhancements is that photon energy is unchanged when scattered, so only light that is within the band gap of the semiconductor is utilized.

1.3.2 Non-Radiative Effects

While radiative effects are the dominant mechanism for plasmonic enhancement in most PV enhancement schemes, non-radiative effects also play a significant role and facilitate coupling of below band gap energy into the semiconductor. Therefore by effectively harnessing non-radiative enhancement processes, ultra-high efficiencies may be realized

in single junction solar cells. Two distinct non-radiative effects contribute to enhanced carrier generation in PVs: hot-electron transfer (HET), and plasmon resonant energy transfer (PRET). Both of these non-radiative energy transfer processes have been studied in photodetectors[74] and solar photocatalysis,[75, 76] but remain poorly understood in PVs. In this section, we discuss the fundamentals of non-radiative enhancement in PVs with plasmonic nanostructures.

When a plasmon decays non-radiatively via Landau damping upon decoherence of the LSPR, this energetic relaxation generates hot electron-hole pairs.[77] Landau damping, a process that has been extensively studied with femtosecond spectroscopy, is a quantum mechanical phenomenon which occurs on a timescale of 1-100 fs.[78, 79] Hot electrons are not in thermal equilibrium with the atoms in the metal and are characterized by an effective elevated temperature.[76, 80] The generation of hot electrons in noble metal nanostructures, such as Au and Ag, is driven by either intraband excitations within the conduction band or by interband excitations resulting from transitions between d bands and the conduction band.[36] In the case of Au, the d-band energy level lies 2.4 eV below the Fermi energy; therefore interband transitions can contribute significantly to the hot carrier generation process. However, in Ag the d-band lies 4 eV below the Fermi energy; hot electrons are therefore mostly generated by intraband excitations.[81] These hot electrons ultimately cool down through electron-electron scattering followed by electron-phonon collisions, releasing their energy to the lattice by dissipation of heat, a phenomenon that has been extensively harnessed in photothermal cancer therapies.[82]

As depicted in Figure 1.7, prior to relaxation, hot electrons can be efficiently captured by forming a Schottky barrier, Φ_{SB}, with a semiconductor such as TiO_2, which has a high density of states in its conduction band and permits rapid electron injection over Φ_{SB}. Hot electrons with sufficient energy to overcome the Φ_{SB} can be injected into the semiconductor conduction band.[74, 83, 84, 85, 86] Since the energy needed for HET is smaller than the bandgap, E_g, of the semiconductor, spectral overlap between the metal nanostructure and

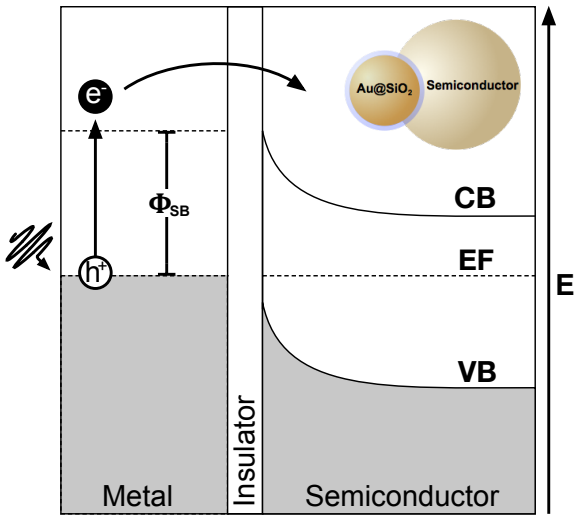

Figure 1.7: Schematic energy diagram of the hot electron transfer process: first, the excitation and subsequent decoherence of a plasmon produces hot electrons and holes, followed by diffusion of hot electrons to the metal-semiconductor interface. Next, hot electrons with sufficient energy traverse the Schottky barrier and tunnel through a thin insulator to enter the conduction band of the neighboring semiconductor.

semiconductor is not required in order for energy transfer to occur. However, HET can only occur when the Fermi levels of the metal and semiconductor are equilibrated, and there is a clear path for electrons to travel between the two.[74, 81] In most plasmon enhanced PEC Typically, platinum salt is brushed onto a transparent conductive oxide (TCO) layer and calcined into platinum metal. and OPV systems, metal nanoparticles are coated in an insulating interlayer such as SiO_2. For HET to occur, the layer must be thinner than the electron tunneling barrier of the material, which is 3 nm for SiO_2.[87] Despite the promise of HET in enhancing carrier generation in plasmon enhanced PVs, recombination of the carriers at interfaces and defect sites remains a challenge. Further, relaxation of hot holes before reaching the hole-transport material, which shuttles the holes to the counter electrode in solar cells, remains a major barrier to successful implementation of HET in PECs and OPVs.

The efficient generation and capture of hot electrons is determined by the shape, size, and composition of metal nanostructures, as well as device design. Nordlander and co-

workers recently calculated hot electron generation in Ag nanoparticles of 15 nm and 25 nm diameter.[81] They demonstrated that when hot carriers are generated with energies close to the Fermi level, an increase in hot carrier production occurs with increasing size. However, larger nanoparticles produce less energetic carriers than smaller Ag nanoparticles. Their analysis also revealed the spatial distribution of hot electrons is primarily localized along the direction parallel to the polarization of the incident field. Govorov and co-workers confirmed that hot electrons are most efficiently generated in Au or Ag nanostructures $<$20 nm size. Since the mean free path of an electron is on the order of 20 nm; hot electrons generated in nanoparticles with dimension $>$20 nm have energies closer to the Fermi level of the metal, and originate from defects in the nanoparticle.[88] The composition of metal nanostructures also determines the rate of Landau damping; for example, metals with strong intraband transitions such as Pd, Pt, and transition metals have weak radiative properties and efficiently convert incident photons to hot electrons. Hot electrons can also be preferentially generated in metal nanostructures with a strong subradiant (dark) mode, such as complex layered architectures or highly anisotropic nanostructures. The superradiant or bright modes in such metal nanostructures directly couple to the incident light and are spectrally broadened due to radiative damping, whereas subradiant modes do not couple to light, hence they are spectrally narrow and relax non-radiatively to produce hot electrons. For example, multilayered metal/dielectric nanoshells,[57, 89] nanostructures with broken symmetry,[90, 91, 92] and ordered clusters of nanostructures[93, 94] all have strong subradiant modes and can produce hot electrons. By engineering the morphology and dimensions of metal nanostructures and coupling with appropriate semiconductors whose Φ_{SB} is relatively close to the Fermi level of the metal, HET can be promoted in PVs. Challenges remain for large scale implementation of hot electron generating devices, including wet chemical synthesis of geometries which promote HET, and the synthesis of an appropriately thin insulating layer to allow for HET to neighboring semiconductor while minimizing unwanted recombination.

In addition to HET, plasmon resonant energy transfer (PRET) also plays a key role in non-radiative plasmonic enhancements in PECs and OPVs. PRET is analogous to Forster resonant energy transfer (FRET) where the LSPR dipole replaces the fluorescent molecule. The LSPR dipole originates from the oscillations of conduction electrons and dephases on plasmon decoherence via absorption or scattering. Following light absorption by the metal nanostructures, PRET occurs when the resonant energy is transferred from the metal to the adjacent semiconductor via dipole-dipole coupling, generating electron-hole pairs below and near the semiconductor band edge.[75, 95, 96] In contrast to HET, where a physical contact between the metal and semiconductor is required, PRET does not require direct contact, and is unaffected by any insulating interlayer, such as SiO_2, between the metal and semiconductor. PRET occurs as long as the semiconductor is within the nanostructures near-field and a spectral overlap exists between the LSPR and the semiconductor absorption. Further, unlike HET where a band alignment of the metal Fermi level with the semiconductor is required, PRET is not limited by Fermi level equilibration.[97] Plasmon enhancement in PVs by PRET is determined by the morphology and composition of metal nanostructures, and distance separating the semiconductor and metal.[30, 98] Wu and coworkers recently performed transient absorption spectroscopy (TAS) and compared the transient signal between four core@shell metal nanospheres, Au@TiO_2, Au@SiO_2@TiO_2, Ag@TiO_2, and Ag@SiO_2@SiO_2 to differentiate the HET and PRET processes.[96] Their results demonstrated that HET was dominant in Au@TiO_2 nanoparticles following light absorption due to direct contact between metal and semiconductor, whereas in Ag@SiO_2@TiO_2 the insulating silica interlayer prevents HET, but promotes PRET due to strong spectral overlap between Ag and TiO_2. In addition, both HET and PRET is possible in Ag@TiO_2, whereas Au@SiO_2@TiO_2 nanoparticles allowed neither HET nor PRET due to poor spectral overlap between Au and TiO_2 and presence of $>$3 nm silica layer preventing plasmon enhanced photoconversion in TiO_2. An enhanced PRET efficiency has also been demonstrated for high aspect ratio nanorods which exhibit longer

dephasing times than nanospheres, up to ~20 fs vs. ~5 fs for spheres.[99, 100, 101] The slow dephasing in nanorods is attributable to reduced radiative damping as a result of low energy LSPR, and the ~1.8 eV threshold for interband transitions.[59, 101] Plasmonic enhancement in solar devices by PRET often competes with FRET, which takes away excited carriers from the semiconductor, and hence distinction of the two processes is essential to preferentially enable PRET. In a recent work, Wu and coworkers differentiated the two processes and demonstrated that in the dipole-dipole coupling regime, exciting the plasmon results in coherent plasmon-to-semiconductor energy transfer via PRET, whereas exciting the semiconductor at its bandgap results in incoherent semiconductor-to-plasmon energy transfer via FRET.[75] They defined the efficiency of dipole-dipole energy transfer for FRET (E_{FRET}) and PRET (E_{PRET}) as follows:

$$E_{FRET} = \frac{1}{(1+(R/R_0)^6)} \tag{1.5}$$

$$E_{PRET} = \frac{(\alpha_{semi}(\omega)+\alpha_{LSPR}(\omega))\frac{1}{(1+\frac{R}{R_0})^6}}{\alpha_{semi}(\omega)} \tag{1.6}$$

where R is the dipole-dipole separation distance, and R_0 is the distance at which 50% of the energy is transferred, and α is frequency-dependent absorption coefficient. The PRET efficiency is dependent on the LSPR dephasing time where a slower plasmon dephasing (10 fs) than the semiconductor (5 fs) results in higher energy transfer via PRET, whereas longer semiconductor dephasing results in FRET. This indicates that when PRET dominates, FRET becomes less efficient and vice-versa, conserving the total energy. The authors also demonstrated PRET efficiency as a function of the LSPR-semiconductor separation distance where PRET is highest where the near-field of the MNSs is the strongest, i.e. at minimum metal-semiconductor separation but not in direct physical contact. On the contrary, the distance dependence for FRET was inversely symmetric to PRET since the plasmons extracted away the excited carriers from the semiconductor in the case of FRET.

While the evidence of PRET has been shown in solar photochemistry and photocatalysis, the contributions of PRET to enhance light trapping in PEC systems remains poorly explored thus far. Since spectral overlap between metal and semiconductor is required for PRET, this mechanism occurs under similar conditions as radiative near field enhancement. Therefore, it is often difficult to differentiate the contributions of the radiative and non-radiative mechanisms. Further work is required to elucidate the potential for PRET in both DSSCs and PSCs.

1.3.3 Plasmon Enhancement in Light Harvesting Devices

Two design schemes for plasmon enhancement of organic photovoltaics have been heavily investigated: buffer layer incorporation and active layer incorporation. When plasmonic particles are incorporated into the buffer layer, they are not in direct contact with the active layer, this presents a distinct set of advantages and disadvantages. Because the metal particle is not in contact with the light absorbing material, it cannot act as a center for recombination, however, the enhanced electric fields must extend into the active layer (5-100 nm) to have an effect. Previous studies using this approach have found enhancements up to 65% for donor/acceptor systems[102]. The buffer layer enhancement approach is illustrated in Figure 1.8a. To maximize the optical enhancement by adding plasmonic nanostructures, it is advantageous to use nanostructures with resonances that have strong overlap with the incident solar spectrum and the absorbing material, as shown in Figure 1.8b-f.

The second approach, incorporating plasmonic particles into the active layer, also has major advantages and disadvantages. Because this approach tends to be more complicated, it is practiced less than the former. Direct incorporation of metal nanoparticles into the active layer can result in a decrease in performance as a result of increased recombination caused by the direct contact of metal with semiconductor[103]. In addition to metal acting as an electron sink, incorporation of metal nanoparticles into the active layer disrupts

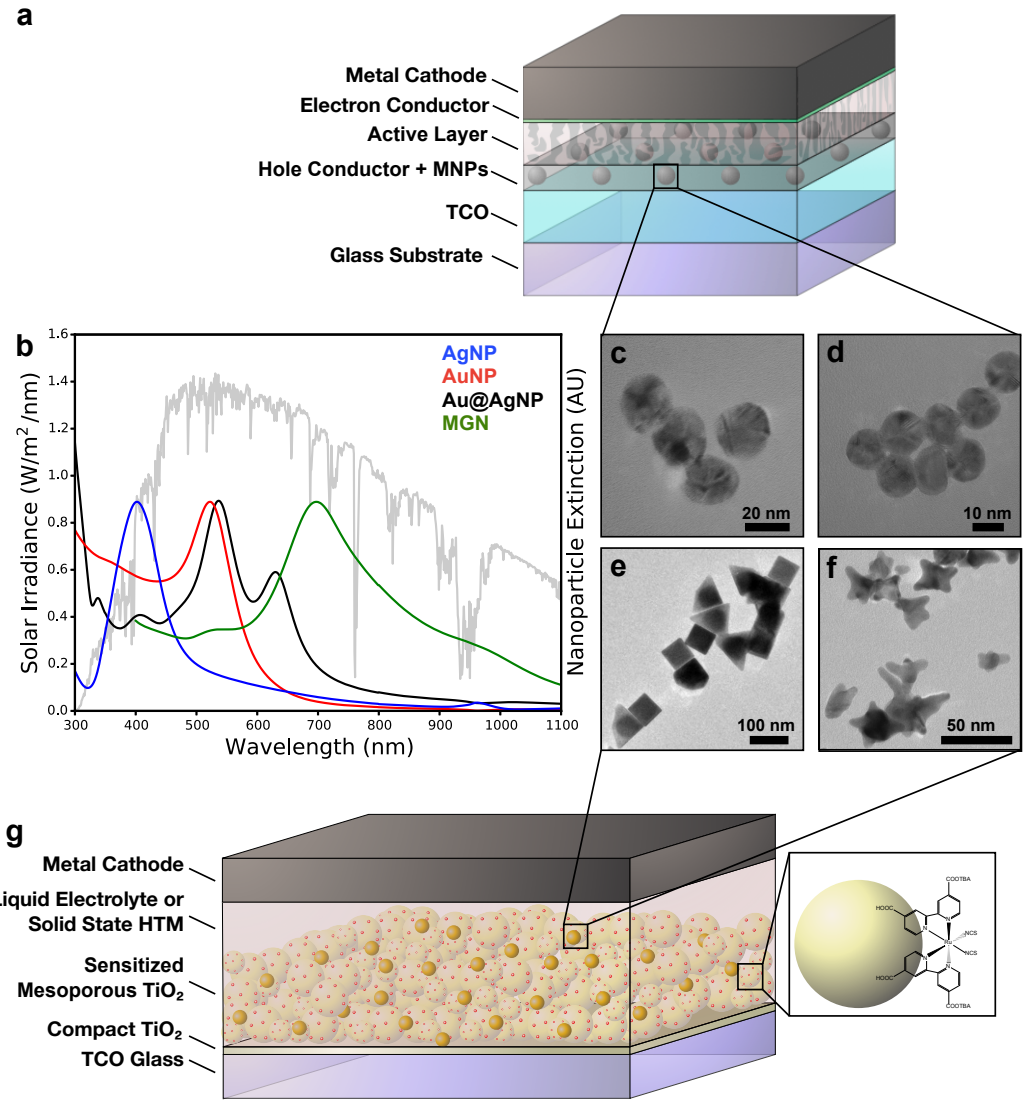

Figure 1.8: (a) Generalized schematic for plasmon enhanced organic photovoltaics. (b) Solar irradiance overlaid with extinction spectra of nanostructures corresponding to TEM images of (c) Ag nanoparticles (Ag NP), (d) Au nanoparticles (Au NP), (e) Au@Ag nanoparticles (Au@Ag NP), and (f) multibranched gold nanoantennas (MGN). (g) Generalized plasmon enhanced mesoporous solar cell schematic.

the morphology of the BHJ. The bulk of recombination can be avoided by adding a thin insulating layer to the nanoparticle, however this is often non-trivial, and trap states are still introduced due to the inherent interruption in active layer morphology. Even when coated with an insulating layer, active layer embedded metal nanoparticles are still within close proximity to the semiconductor ($<$10 nm). Near field effects are typically exploited using particles with sharp corners and edges, which exhibit strong local field enhancement. For this approach, enhancements up to 95% have been reported.[102]. For a P3HT based system, it has been reported that the effects of adding nanoparticles to both the buffer and active layers are cooperative, with enhancements of 14% and 8% for the individual approaches, respectively, but a 21% enhancement when the approaches were combined[104].

In addition to OPVs, plasmonic nanoparticles can be used to improve efficiencies in PEC water splitting where low solar energy conversion efficiency due to low spectral absorption stands as a major barrier in large scale production and implementation. The use of plasmonic metal nanoparticles for enhancement of a photoelectrochemical light harvesting device is pictured schematically in Figure 1.8g.[105, 106, 107, 108, 109, 17, 41] MNS of sub-wavelength dimensions couple incident light to conduction-band electrons, generating surface plasmons which give rise to intense electromagnetic near-fields at the metal surface.[110] When MNS with controllable shapes and sizes are integrated with the mesoporous semiconductor, the result is significant optical enhancement and improved e^-/h^+ generation increasing the H_2 production efficiency.[111] Plasmon-mediated enhancement is achieved in two ways: *(i)* MNS absorb solar energy in the visible and scatter light which is trapped in the semiconductor by total internal reflection increasing the optical path length, and *(ii)* MNS absorb light and couple the electromagnetic near-fields into the semiconductor thereby amplifying the light absorption and rate of e^-/h^+ formation. By positioning the MNS arrays into the mesoporous semiconducting layer, the scattering mechanism of MNS plasmons will be harnessed and light will be preferentially scattered into the semiconductor layer increasing the optical path length. Strong near-field effects

are also observed, which couple with the semiconductor, increasing the rate of e^{-}/h^{+} pair formation in the active layer.

1.4 Bibliography

[1] T.F. Stocker, D. Qin, G.-K. Plattner, S.K. Alexander, N.L. Allen, M. Bindoff, F, J.A. Breon, U. Church, S. Cubasch, S. Emori, P. Forster, N. Friedlingstein, J.M. Gillett, D.L. Gregory, E. Hartmann, B. Jansen, and R. Kirtman. Climate Change 2013: The Physical Science Basis. Contribution of Working Group I to the Fifth Assessment Report of the Intergovernmental Panel on Climate Change,. Technical report, Cambridge University Press, Cambridge, United Kingdom and New York, NY, USA, 2013.

[2] Barack Obama. The irreversible momentum of clean energy. *Science*, 355(6321):126–129, 2017.

[3] U.S. Enery Information Administration. Short-Term Energy Outlook. Technical report, U.S. Department of Energy, Washington, D.C., 2017.

[4] Sean E. Shaheen, Christoph J. Brabec, N. Serdar Sariciftci, Franz Padinger, Thomas Fromherz, and Jan C. Hummelen. 2.5% Efficient Organic Plastic Solar Cells. *Appl. Phys. Lett.*, 78(6):841, 2001.

[5] Martin A. Green, Keith Emery, Yoshihiro Hishikawa, Wilhelm Warta, and Ewan D. Dunlop. Solar cell efficiency tables (version 48). *Prog. Photovoltaics Res. Appl.*, 24:905–913, 2016.

[6] Shigehiko Mori, Haruhi Oh-oka, Hideyuki Nakao, Takeshi Gotanda, Yoshihiko Nakano, Hyangmi Jung, Atsuko Iida, Rumiko Hayase, Naomi Shida, Mitsunaga Saito, Kenji Todori, Taro Asakura, Akihiro Matsui, and Masahiro Hosoya. Organic photovoltaic module development with inverted device structure. *MRS Proc.*, 1737, 2015.

[7] Seok In Na, Seok Soon Kim, Jang Jo, and Dong Yu Kim. Efficient and Flexible ITO-Free Organic Solar Cells Using Highly Conductive Polymer Anodes. *Adv. Mater.*, 20(21):4061–4067, 2008.

[8] Martin Kaltenbrunner, Matthew S White, Eric D Głowacki, Tsuyoshi Sekitani, Takao Someya, Niyazi Serdar Sariciftci, and Siegfried Bauer. Ultrathin and lightweight organic solar cells with high flexibility. *Nat. Commun.*, 3:770, 2012.

[9] Guillaume A. Rivière, Jean Jacques Simon, Ludovic Escoubas, Wilfried Vervisch, and Marcel Pasquinelli. Photo-electrical characterizations of plastic solar modules. *Sol. Energy Mater. Sol. Cells*, 102:19–25, 2012.

[10] Thomas R. Andersen, Thue T. Larsen Olsen, Birgitta Andreasen, Arvid P. L. Böttiger, Jon E. Carlé, Martin Helgesen, Eva Bundgaard, Kion Norrman, Jens W. Andreasen, Mikkel Jørgensen, and Frederik C. Krebs. Aqueous processing of low-band-gap polymer solar cells using roll-to-roll methods. *ACS Nano*, 5(5):4188–96, 2011.

[11] Roar Søndergaard, Martin Helgesen, Mikkel Jørgensen, and Frederik C. Krebs. Fabrication of Polymer Solar Cells Using Aqueous Processing for All Layers Including the Metal Back Electrode. *Adv. Energy Mater.*, 1(1):68–71, 2011.

[12] Luyao Lu and Luping Yu. Understanding Low Bandgap Polymer PTB7 and Optimizing Polymer Solar Cells Based on It. *Adv. Mater.*, 26:4413–4430, 2014.

[13] Duygu Kozanoglu, Dogukan Hazar Apaydin, Ali Cirpan, and Emren Nalbant Esenturk. Power conversion efficiency enhancement of organic solar cells by addition of gold nanostars, nanorods, and nanospheres. *Org. Electron.*, 14(7):1720–1727, 2013.

[14] N. S. Sariciftci, L. Smilowitz, A. J. Heeger, and F. Wudl. Photoinduced electron transfer from a conducting polymer to buckminsterfullerene. *Science*, 258(5087):1474–6, 1992.

[15] Antonio Facchetti. Polymer donorpolymer acceptor (all-polymer) solar cells. *Mater. Today*, 16(4):123–132, 2013.

[16] Michael Gratzel. Photoelectrochemical cells. *Nature*, 414:338–344, 2001.

[17] Hao Ming Chen, Chih Kai Chen, Ru-Shi Liu, Lei Zhang, Jiujun Zhang, and David P. Wilkinson. Nano-architecture and material designs for water splitting photoelectrodes. *Chem. Soc. Rev.*, 41(17):5654–71, 2012.

[18] Yasuhiro Tachibana, Lionel Vayssieres, and James R. Durrant. Artificial photosynthesis for solar water-splitting. *Nat. Photonics*, 6:511–518, 2012.

[19] Brian O'Regan and Michael Gratzel. A low-cost, high-efficiency solar cell based on dye-sensitized colloidal TiO2 films. *Nature*, 353:737–740, 1991.

[20] Michael G. Walter, Emily L. Warren, James R. McKone, Shannon W. Boettcher, Qixi Mi, Elizabeth A. Santori, and Nathan S. Lewis. Solar water splitting cells. *Chem. Rev.*, 110(11):6446–6473, 2010.

[21] Akihiko Kudo and Yugo Miseki. Heterogeneous photocatalyst materials for water splitting. *Chem. Soc. Rev.*, 38(1):253–78, 2009.

[22] Michael Grätzel. Dye-sensitized solar cells. *J. Photochem. Photobiol. C Photochem. Rev.*, 4(2):145–153, 2003.

[23] Qinghua Li, Jihuai Wu, Qunwei Tang, Zhang Lan, Pinjiang Li, Jianming Lin, and Leqing Fan. Application of microporous polyaniline counter electrode for dye-sensitized solar cells. *Electrochem. commun.*, 10(9):1299–1302, 2008.

[24] Yu Hou, Dong Wang, Xiao Hua Yang, Wen Qi Fang, Bo Zhang, Hai Feng Wang, Guan Zhong Lu, P. Hu, Hui Jun Zhao, and Hua Gui Yang. Rational screening low-cost counter electrodes for dye-sensitized solar cells. *Nat. Commun.*, 4:1583, 2013.

[25] Pei Dong, Cary L. Pint, Mel Hainey, Francesca Mirri, Yongjie Zhan, Jing Zhang, Matteo Pasquali, Robert H. Hauge, Rafael Verduzco, Mian Jiang, Hong Lin, and Jun Lou. Vertically aligned single-walled carbon nanotubes as low-cost and high electrocatalytic counter electrode for dye-sensitized solar cells. *ACS Appl. Mater. Interfaces*, 3(8):3157–61, 2011.

[26] Josef Velten, Attila J. Mozer, Dan Li, David Officer, Gordon Wallace, Ray Baughman, and Anvar Zakhidov. Carbon nanotube/graphene nanocomposite as efficient counter electrodes in dye-sensitized solar cells. *Nanotechnology*, 23(8):085201, 2012.

[27] Martin Pumera. The electrochemistry of carbon nanotubes: fundamentals and applications. *Chemistry (Easton).*, 15(20):4970–8, 2009.

[28] Joseph D. Roy-Mayhew, David J. Bozym, Christian Punckt, and Ilhan A. Aksay. Functionalized Graphene as a Catalytic Solar Cells. *ACS Nano*, 4(10):6203–6211, 2010.

[29] Yuhua Xue, Jun Liu, Hao Chen, Ruigang Wang, Dingqiang Li, Jia Qu, and Liming Dai. Nitrogen-doped graphene foams as metal-free counter electrodes in high-performance dye-sensitized solar cells. *Angew. Chemie*, 51(48):12124–7, 2012.

[30] Hyunbong Chio, Wei Ta Chen, and Prashant Kamat. Know Thy Nano Neighbor. Plasmonic versus Electron Charging Effects of Metal Nanoparticles in Dye-Sensitized Solar Cells. *ACS Nano*, 6(5):4418–4427, 2012.

[31] Kun Seok Lee, Won Jun Lee, Nam-Gyu Park, Sang Ouk Kim, and Jong Hyeok Park. Transferred vertically aligned N-doped carbon nanotube arrays: use in dye-sensitized solar cells as counter electrodes. *Chem. Commun.*, 47(14):4264–6, 2011.

[32] Kun Seok Lee, Hang Ken Lee, Dong Hwan Wang, Nam-Gyu Park, Jun Young Lee, O Ok Park, and Jong Hyeok Park. Dye-sensitized solar cells with Pt- and TCO-free counter electrodes. *Chem. Commun.*, 46(25):4505–7, 2010.

[33] Prakash Joshi, Yu Xie, Mike Ropp, David Galipeau, Shelia Bailey, and Qiquan Qiao. Dye-sensitized solar cells based on low cost nanoscale carbon/TiO2 composite counter electrode. *Energy Environ. Sci.*, 2(4):426, 2009.

[34] Prakash Joshi, Lifeng Zhang, Qiliang Chen, David Galipeau, Hao Fong, and Qiquan Qiao. Electrospun carbon nanofibers as low-cost counter electrode for dye-sensitized solar cells. *ACS Appl. Mater. Interfaces*, 2(12):3572–7, 2010.

[35] Craig F. Borhen and Donald R. Huffman. *Absorption and Scattering of Light by Small Particles*. Wiley, 1983.

[36] Stefan A. Maier. *Plasmonics: Fundamentals and Applications*. Springer, 2007.

[37] H. C. van de Hulst. *Light Scattering by Small Particles*. Dover Publications Inc., New York, NY, 1981.

[38] R. Carminati, J.-J. Greffet, C. Henkel, and J.M. Vigoureux. Radiative and non-radiative decay of a single molecule close to a metallic nanoparticle. *Opt. Commun.*, 261(2):368–375, 2006.

[39] Prashant K. Jain, Wenyu Huang, and Mostafa A. El-Sayed. On the universal scaling behavior of the distance decay of plasmon coupling in metal nanoparticle pairs: A plasmon ruler equation. *Nano Lett.*, 7(7):2080–2088, 2007.

[40] Joseph R. Lakowicz. Radiative decay engineering 5: metal-enhanced fluorescence and plasmon emission. *Anal. Biochem.*, 337(2):171–194, 2005.

[41] Scott C. Warren and Elijah Thimsen. Plasmonic solar water splitting. *Energy Environ. Sci.*, 5(1):5133–5146, 2012.

[42] Anatoly V. Zayats, Igor I. Smolyaninov, and Alexei A. Maradudin. Nano-optics of surface plasmon polaritons. *Phys. Rep.*, 408(3-4):131–314, 2005.

[43] Wei-Shun Chang, Britain A. Willingham, Liane S. Slaughter, Bishnu P. Khanal, Leonid Vigderman, Eugene R. Zubarev, and Stephan Link. Low absorption losses of strongly coupled surface plasmons in nanoparticle assemblies. *Proc. Natl. Acad. Sci. U. S. A.*, 108(50):19879–84, 2011.

[44] Jonathan A. Fan, Chihhui Wu, Kui Bao, Jiming Bao, Rizia Bardhan, Naomi J. Halas, Vinothan N. Manoharan, Peter Nordlander, Gennady Shvets, and Federico Capasso. Self-assembled plasmonic nanoparticle clusters. *Science*, 328(5982):1135–1138, 2010.

[45] Andrea Tao, Prasert Sinsermsuksakul, and Peidong Yang. Tunable plasmonic lattices of silver nanocrystals. *Nat. Nanotechnol.*, 2(7):435–440, 2007.

[46] Mahesh K Gangishetty, Robert W J Scott, and Timothy L Kelly. Panchromatic Enhancement of Light-Harvesting Efficiency in Dye- Sensitized Solar Cells Using Thermally Annealed Au@SiO2 Triangular Nanoprisms. *Langmuir*, 30:14352–14359, 2014.

[47] Hsiang-Lin Hsu, Tzong-Yuan Juang, Chih-Ping Chen, Cheng-Ming Hsieh, Chun-Chen Yang, Cheng-Liang Huang, and Ru-Jong Jeng. Enhanced efficiency of organic and perovskite photovoltaics from shape-dependent broadband plasmonic effects of silver nanoplates. *Sol. Energy Mater. Sol. Cells*, 140:224–231, 2015.

[48] Wolfram Hergert and Thomas Wriedt, editors. *The Mie Theory: Basics and Applications*. Springer, New York, NY, 1 edition, 2012.

[49] William T. Doyle. Optical properties of a suspension of metal spheres. *Phys. Rev. B*, 39(14):9852–9858, 1989.

[50] Xiaofeng Fan, Weitao Zheng, and David J. Singh. Light scattering and surface plasmons on small spherical particles. *Light Sci. Appl.*, 3(6):e179, 2014.

[51] Q. Fu and W. Sun. Mie theory for light scattering by a spherical particle in an absorbing medium. *Appl. Opt.*, 40:1354–1361, 2001.

[52] C. Sonnichsen, T. Franzl, T. Wilk, G. von Plessen, and J. Feldmann. Plasmon resonances in large noble-metal clusters. *New J. Phys.*, 4:93–93, 2002.

[53] K. L. Kelly, K. Lance Kelly, E. Coronado, L. Zhao, Eduardo Coronado, G. C. Schatz, Lin Lin Zhao, and George C. Schatz. The Optical Properties of Metal Nanoparticles: The Influence of Size, Shape, and Dielectric Environment. *J. Phys. Chem. B*, 107(3):668–677, 2003.

[54] Kyeong Seok Lee and Mostafa A. El-Sayed. Gold and silver nanoparticles in sensing and imaging: Sensitivity of plasmon response to size, shape, and metal composition. *J. Phys. Chem. B*, 110(39):19220–19225, 2006.

[55] Encai Hao, George C. Schatz, and Joseph T. Hupp. Synthesis and optical properties of anisotropic metal nanoparticles. *J. Fluoresence*, 14(4):331–341, 2004.

[56] C. Sosa Noguez, R. G. Barrera, Iván O. Sosa, Cecila Noguez, and Rubén G. Barrera. Optical Properties of Metal Nanoparticles with Arbitrary Shapes. *J. Phys. Chem. B*, 107(26):6269–6275, 2003.

[57] Rizia Bardhan, Shaunak Mukherjee, Nikolay A. Mirin, Stephen D. Levit, Peter Nordlander, and Naomi J. Halas. Nanosphere-in-a-Nanoshell: A Simple Nanomatryushka. *J. Phys. Chem. C*, 114(16):7378–7383, 2010.

[58] N.K. Grady, N.J. Halas, and P. Nordlander. Influence of dielectric function properties on the optical response of plasmon resonant metallic nanoparticles. *Chem. Phys. Lett.*, 399(1-3):167–171, 2004.

[59] P. B. Johnson and R. W. Christy. Optical Constants of the Noble Metals, 1972.

[60] Anatoliy Pinchuk, Gero Von Plessen, and Uwe Kreibig. Influence of interband electronic transitions on the optical absorption in metallic nanoparticles. *J. Phys. D. Appl. Phys.*, 37(22):3133–3139, 2004.

[61] J. M. Pitarke, V. M. Silkin, E. V. Chulkov, and P. M. Echenique. Theory of surface plasmons and surface-plasmon polaritons. *Reports Prog. Phys.*, 70(1):1–87, 2007.

[62] Gede Widia Pratama Adhyaksa, Se-Woong Baek, Ga In Lee, Dong Ki Lee, Jun-Yong Lee, and Jeung Ku Kang. Coupled Near- and Far-Field Scattering in Silver Nanoparticles for High-Efficiency , Stable , and Thin Plasmonic Dye-Sensitized Solar Cells. *ChemSusChem*, 7:2461–2468, 2014.

[63] J. M. Pitarke, V. M. Silkin, E. V. Chulkov, and P. M. Echenique. Surface plasmons in metallic structures. *J. Opt. A Pure Appl. Opt.*, 7:S73–S84, 2005.

[64] Hua Dong, Zhaoxin Wu, Fan Lu, Yucui Gao, Ahmed El-shafei, Bo Jiao, Shuya Ning, and Xun Hou. Optics electrics highways : Plasmonic silver nanowires @ TiO 2 core shell nanocomposites for enhanced dye-sensitized solar cells performance. *Nano Energy*, 10:181–191, 2014.

[65] Kyeong-seok Lee and Mostafa A. El-sayed. Dependence of the Enhanced Optical Scattering Efficiency Relative to That of Absorption for Gold Metal Nanorods on Aspect Ratio, Size, End-Cap Shape, and Medium Refractive Index. *J. Phys. Chem. B*, 109:20331–20338, 2005.

[66] A. Liebsch and B. N. J. Persson. Optical properties of small metallic particles in a continuous dielectric medium. *J. Phys. C Solid State Phys.*, 16(27):5375–5391, 1983.

[67] S. Link, M. B. Mohamed, and M. A. El-Sayed. Simulation of the Optical Absorption Spectra of Gold Nanorods as a Function of Their Aspect Ratio and the Effect of the Medium Dielectric Constant. *J. Phys. Chem. B*, 103(16):3073–3077, 1999.

[68] Feng Wang and Y. Ron Shen. General properties of local plasmons in metal nanostructures. *Phys. Rev. Lett.*, 97(20):1–4, 2006.

[69] Traci R. Jensen, Michelle L. Duval, K. Lance Kelly, Anne A. Lazarides, George C. Schatz, and Richard P. Van Duyne. Nanosphere Lithography: Effect of the External Dielectric Medium on the Surface Plasmon Resonance Spectrum of a Periodic Array of Silver Nanoparticles. *J. Phys. Chem. B*, 103(45):9846–9853, 1999.

[70] Mohamed Haggui, Montacer Dridi, Jerome Plain, Sylvie Marguet, Henri Perez, George C. Schatz, Gary P. Wiederrecht, Stephen K. Gray, and Renaud Bachelot. Spatial confinement of electromagnetic hot and cold spots in gold nanocubes. *ACS Nano*, 6(2):1299–1307, 2012.

[71] Matthew Rycenga, Moon Ho Kim, Pedro H. C. Camargo, Claire Cobley, Zhiyuan Li, and Younan Xia. Surface-Enhanced Raman Scattering : Comparison of Three Different Molecules on Single-Crystal Nanocubes and Nanospheres of Silver Surface-Enhanced Raman Scattering : Comparison of Three Different Molecules on Single-Crystal Nanocubes and Nanospheres of Si. *J. Phys. Chem. A*, 113:3932–3939, 2009.

[72] J. Gersten and A. Nitzan. Electromagnetic theory of enhanced Raman scattering by molecules adsorbed on rough surfaces. *J. Chem. Phys.*, 73(7):3023, 1980.

[73] P. F. Liao. Lightning rod effect in surface enhanced Raman scattering. *J. Chem. Phys.*, 76(1):751, 1982.

[74] Mark W. Knight, Heidar Sobhani, Peter Nordlander, and Naomi J. Halas. Photodetection with Active Optical Antennas. *Science*, 332:19–22, 2011.

[75] Jiangtian Li, Scott K. Cushing, Fanke Meng, Tess R. Senty, Alan D. Bristow, and Nianqiang Wu. Plasmon-induced resonance energy transfer for solar energy conversion. *Nat. Photonics*, 9(9):601–607, 2015.

[76] César Clavero. Plasmon-induced hot-electron generation at nanoparticle/metal-oxide interfaces for photovoltaic and photocatalytic devices. *Nat. Photonics*, 8(2):95–103, 2014.

[77] Xiaoguang Li, Di Xiao, and Zhenyu Zhang. Landau damping of quantum plasmons in metal nanostructures. *New J. Phys.*, 15(2):023011, 2013.

[78] R. Bingham, J. Mendonça, and J. Dawson. Photon Landau Damping. *Phys. Rev. Lett.*, 78(6):247–249, 1997.

[79] Yi Gao, Zhe Yuan, and Shiwu Gao. Semiclassical approach to plasmon-electron coupling and Landau damping of surface plasmons. *J. Chem. Phys.*, 134(13):1–5, 2011.

[80] Mark L. Brongersma, Naomi J. Halas, and Peter Nordlander. Plasmon-induced hot carrier science and technology. *Nature*, 10(1):25–34, 2015.

[81] Alejandro Manjavacas, Jun G. Liu, Vikram Kulkarni, and Peter Nordlander. Plasmon-Induced Hot Carriers in Metallic Nanoparticles. *ACS Nano*, 8(8):7630–7638, 2014.

[82] Joseph A. Webb and Rizia Bardhan. Emerging advances in nanomedicine with engineered gold nanostructures. *Nanoscale*, pages 2502–2530, 2014.

[83] Syed Mubeen, Joun Lee, Woo-Ram Lee, Nirala Singh, Galen D. Stucky, and Martin Moskovits. On the Plasmonic Photovoltaic. *ACS Nano*, 8(6):6066–6073, 2014.

[84] Syed Mubeen, Joun Lee, Nirala Singh, Stephan Krämer, Galen D. Stucky, and Martin Moskovits. An autonomous photosynthetic device in which all charge carriers derive from surface plasmons. *Nat. Nanotechnol.*, 8(4):247–251, 2013.

[85] Shaunak Mukherjee, Linan Zhou, Amanda M. Goodman, Nicolas Large, Ciceron Ayala-Orozco, Yu Zhang, Peter Nordlander, and Naomi J. Halas. Hot-electron-induced dissociation of H2 on gold nanoparticles supported on SiO2. *J. Am. Chem. Soc.*, 136(1):64–67, 2014.

[86] Ali Sobhani, Mark W. Knight, Yumin Wang, Bob Zheng, Nicholas S. King, Lisa V. Brown, Zheyu Fang, Peter Nordlander, and Naomi J. Halas. Narrowband photodetection in the near-infrared with a plasmon-induced hot electron device. *Nat. Commun.*, 4:1643, 2013.

[87] William R. Erwin, Holly Zarick, Eric M. Talbert, and Rizia Bardhan. Light Trapping in Mesoporous Solar Cells with Plasmonic Nanostructures. *Energy Environ. Sci.*, 9:1577–1601, 2016.

[88] Alexander O. Govorov, Hui Zhang, and Yurii K. Gun'Ko. Theory of photoinjection of hot plasmonic carriers from metal nanostructures into semiconductors and surface molecules. *J. Phys. Chem. C*, 117(32):16616–16631, 2013.

[89] Shaunak Mukherjee, Heidar Sobhani, J. Britt Lassiter, Rizia Bardhan, Peter Nordlander, and Naomi J. Halas. Fanoshells: Nanoparticles with built-in Fano resonances. *Nano Lett.*, 10(7):2694–2701, 2010.

[90] Zheyu Fang, Junyi Cai, Zhongbo Yan, Peter Nordlander, Naomi J. Halas, and Xing Zhu. Removing a wedge from a metallic nanodisk reveals a fano resonance. *Nano Lett.*, 11(10):4475–4479, 2011.

[91] Feng Hao, Yannick Sonnefraud, Pol Van Dorpe, Stefan A. Maier, Naomi J. Halas, and Peter Nordlander. Symmetry breaking in plasmonic nanocavities: Subradiant LSPR sensing and a tunable Fano resonance. *Nano Lett.*, 8(11):3983–3988, 2008.

[92] Feng Hao, Peter Nordlander, Yannick Sonnefraud, Pol Van Dorpe, and Stefan A. Maier. Tunability of subradiant dipolar and fano-type plasmon resonances in metallic ring/disk cavities: Implications for nanoscale optical sensing. *ACS Nano*, 3(3):643–652, 2009.

[93] Jonathan A. Fan, Kui Bao, Chihhui Wu, Jiming Bao, Rizia Bardhan, Naomi J. Halas, Vinothan N. Manoharan, Gennady Shvets, Peter Nordlander, and Federico Capasso. Fano-like interference in self-assembled plasmonic quadrumer clusters. *Nano Lett.*, 10(11):4680–4685, 2010.

[94] Mario Hentschel, Daniel Dregely, Ralf Vogelgesang, Harald Giessen, and Na Liu. Plasmonic oligomers: The role of individual particles in collective behavior. *ACS Nano*, 5(3):2042–2050, 2011.

[95] Scott K. Cushing, Jiangtian Li, Fanke Meng, Tess R. Senty, Savan Suri, Mingjia Zhi, Ming Li, Alan D. Bristow, and Nianqiang Wu. Photocatalytic Activity Enhanced by Plasmonic Resonant Energy Transfer from Metal to Semiconductor. *J. Am. Chem. Soc.*, 134, 2012.

[96] Scott K. Cushing, Jiangtian Li, Joeseph Bright, Brandon T. Yost, Peng Zheng, Alan D. Bristow, and Nianqiang Wu. Controlling Plasmon-Induced Resonance Energy Transfer and Hot Electron Injection Processes in Metal@TiO 2 CoreShell Nanoparticles. *J. Phys. Chem. C*, pages 16239–16244, 2015.

[97] Anatoliy Pinchuk and Uwe Kreibig. Interface decay channel of particle surface plasmon resonance. *New J. Phys.*, 5, 2003.

[98] Q. Wang, T. Butburee, X. Wu, H. J. Chen, G. Liu, and L. Z. Wang. Enhanced performance of dye-sensitized solar cells by doping Au nanoparticles into photoanodes: a size effect study. *J. Mater. Chem. A.*, 1(5):13524–13531, 2013.

[99] Alexandria Anderson, Kseniya S. Deryckx, Xiaoji G. Xu, Günter Steinmeyer, and Markus B. Raschke. Few-femtosecond plasmon dephasing of a single metallic nanostructure from optical response function reconstruction by interferometric frequency resolved optical gating. *Nano Lett.*, 10(7):2519–2524, 2010.

[100] Yoshio Nishiyama, Keisuke Imaeda, Kohei Imura, and Hiromi Okamoto. Plasmon dephasing in single gold nanorods observed by ultrafast time-resolved near-field optical microscopy. *J. Phys. Chem. C*, 119(28):16215–16222, 2015.

[101] C. Sonnichsen, T. Franzl, T. Wilk, G. von Plessen, J. Feldmann, O. Wilson, and P. Mulvaney. Drastic reduction of plasmon damping in gold nanorods. *Phys. Rev. Lett.*, 88(7):774021–774024, 2002.

[102] Emmanuel Stratakis and Emmanuel Kymakis. Nanoparticle-based plasmonic organic photovoltaic devices. *Mater. Today*, 16(4):133–146, 2013.

[103] Bo Wu, Xiangyang Wu, Cao Guan, Kong Fai Tai, Edwin Kok Lee Yeow, Hong Jin Fan, Nripan Mathews, and Tze Chien Sum. Uncovering loss mechanisms in silver nanoparticle-blended plasmonic organic solar cells. *Nat. Commun.*, 4(2004):1–7, 2013.

[104] Luyao Lu, Zhiqiang Luo, Tao Xu, and Luping Yu. Cooperative plasmonic effect of Ag and Au nanoparticles on enhancing performance of polymer solar cells. *Nano Lett.*, 13(1):59–64, 2013.

[105] Zuwei Liu, Wenbo Hou, Prathamesh Pavaskar, Mehmet Aykol, and Stephen B. Cronin. Plasmon resonant enhancement of photocatalytic water splitting under visible illumination. *Nano Lett.*, 11(3):1111–1116, 2011.

[106] K. R. Catchpole and a. Polman. Design principles for particle plasmon enhanced solar cells. *Appl. Phys. Lett.*, 93(19):191113, 2008.

[107] Rui Liu, Yongjing Lin, Lien-Yang Chou, Stafford W. Sheehan, Wangshu He, Fan Zhang, Harvey J. M. Hou, and Dunwei Wang. Water splitting by tungsten oxide prepared by atomic layer deposition and decorated with an oxygen-evolving catalyst. *Angew. Chemie*, 50(2):499–502, 2011.

[108] Joun Lee, Syed Mubeen, Xiulei Ji, Galen D. Stucky, and Martin Moskovits. Plasmonic photoanodes for solar water splitting with visible light. *Nano Lett.*, 12(9):5014–5019, 2012.

[109] K. R. Catchpole and Albert Polman. Plasmonic solar cells. *Opt. Express*, 16(26):21793–800, 2008.

[110] Vincenzo Giannini, Antonio I. Fernández-Domínguez, Susannah C. Heck, and Stefan A. Maier. Plasmonic nanoantennas: fundamentals and their use in controlling the radiative properties of nanoemitters. *Chem. Rev.*, 111(6):3888–912, 2011.

[111] Suljo Linic, Phillip Christopher, and David B. Ingram. Plasmonic-metal nanostructures for efficient conversion of solar to chemical energy. *Nat. Mater.*, 10(12):911–921, 2011.

Chapter 2

PLASMON ENHANCED WATER SPLITTING MEDIATED BY HYBRID BIMETALLIC AU-AG CORE-SHELL NANOSTRUCTURES

2.1 Summary

In this chapter, we employed wet chemically synthesized bimetallic Au-Ag core-shell nanostructures (Au-AgNSs) to enhance the photocurrent density of mesoporous TiO_2 for water splitting and we compared the results with monometallic Au nanoparticles (AuNPs). While Au-AgNSs incorporated photoanodes give rise to 14× enhancement in incident photon to charge carrier efficiency, AuNPs embedded photoanodes result in 6× enhancement. By varying nanoparticle concentration in the photoanodes, we observed ~245× less Au-AgNSs are required relative to AuNPs to generate similar photocurrent enhancement for solar fuel conversion. Power-dependent measurements of Au-AgNSs and AuNPs showed a first order dependence to incident light intensity, relative to half-order dependence for TiO_2 only photoanodes. This indicated that plasmonic nanostructures enhance charge carriers formed on the surface of the TiO_2 which effectively participate in photochemical reactions. Our experiments and simulations suggest the enhanced near-field, far-field, and multipolar resonances of Au-AgNSs facilitating broadband absorption of solar radiation collectively gives rise to their superior performance in water splitting.

2.2 Introduction

The conversion of solar energy into a renewable chemical fuel, which can be stored and released on demand both for stationary applications and transportation, offers a promising alternative to the use of fossil fuels. Solar driven photocatalytic water splitting affords enormous prospects to produce H_2, a sustainable and clean fuel, potentially at the terawatt

scale.[1, 2] However, despite the promise of solar-to-hydrogen conversion technology, poor efficiencies and challenges with scalability have severely hindered their broad deployment for clean energy production.[3] For example, an ideal market-ready solar-to-fuel system must simultaneously *(i)* be composed of earth-abundant, robust, and inexpensive semiconductors which absorb broadband solar radiation,[4] *(ii)* have long minority carrier diffusion lengths to minimize bulk recombination of e^-/h^+ pairs, *(iii)* enable separation of charge carriers and transport to the semiconductor/liquid interface where half reactions occur, and *(iv)* have active surface sites that enable charge transfer processes at the semiconductor/liquid interface and lower the kinetic overpotential needed for the half reactions.[5, 6] Currently available semiconductors do not meet all these requirements. For example the most investigated n-type semiconductor, TiO_2, while inexpensive, has a large bandgap (3.2 eV) which limits its photo-activity to the UV region of the solar spectrum.[7] Hematite, α-Fe_2O_3, a promising alternative to TiO_2, has a more narrow bandgap (2.2 eV) but suffers from low mobility of energetic charge carriers.[8] Narrow bandgap semiconductors with high carrier mobility, such as Si and InP, are either limited by poor catalytic activity of surface sites (Si) or are expensive (InP) and an impractical solution to large scale devices.[9]

Alternatively, semiconductors integrated with metal nanostructures have demonstrated remarkably improved performance for solar-to-fuel conversion.[10, 11, 12, 13, 14] Topologically compact metallic nanostructures with sub-wavelength dimensions couple incident photons to conduction electrons generating localized surface plasmon resonances (LSPR) that give rise to electric fields with intensities that can be orders of magnitude greater than that of the incident field.[15, 16] LSPRs also result in strong light scattering into the far-field. These near-field and far-field properties of metal nanostructures have been long known to enhance optical properties of adjacent molecules and semiconductors by modifying their photonic mode density,[17, 18, 19, 20] a concept that has been harnessed extensively in solar devices.[21, 22, 23, 24] The SPR of metal nanostructures are governed by both geometry and dimension. Unlike spherical nanoparticles, nanostruc-

tures with sharp edges and corners such as cubic and pyramidal morphologies generate intense electromagnetic fields localized at the corners due to the quasi-static lightening rod effect.[25, 26, 27] Such morphology-controlled nanostructures when integrated with semiconductors for photocatalytic water splitting give rise to enhanced light absorption and current collection.[28, 2]

In addition to morphology, the composition of metal nanostructures also contributes to the absorption and scattering. Bimetallic nanostructures where two metals are coupled together in core-shell architecture can be designed to exhibit enhanced electronic properties not achievable by monometallic nanostructures.[29, 30] Gold core-silver shell bimetallic nanostructures offer several advantages for water splitting including *(i)* dual metals generate multiple plasmon resonances allowing broadband absorption of solar light, *(ii)* intense near-field enhancements facilitating superior light harvesting characteristics, *(iii)* less Ohmic losses in Ag relative to Au, giving rise to enhanced radiative damping and strong light scattering,[31] and *(iv)* core-shell architecture enabling dynamic modulation of electronic properties without altering the overall size. Here we demonstrate the use of Au-Ag core-shell nanostructures (Au-AgNSs) to enhance the photoactivity of mesoporous TiO_2 photoanodes. Relative to monometallic Au nanoparticles (AuNPs), Au-AgNSs demonstrate a higher absorption across the solar spectrum and stronger enhancement in incident photon to charge carrier efficiency (IPCE). Our experiments and electrodynamics simulations show that broadband absorption of incident light as well as enhanced scattering and near-field effects result in the superior performance of Au-AgNSs relative to AuNPs.

2.3 Results and Discussion

Bimetallic Au-Ag NSs were synthesized following our previously reported procedure.[30] Au nanocrystal cores of 46 $\pm$ 3 nm, which consisted of both rounded corner nanocubes and truncated nanocubes, were coated in Ag shell which resulted in two distinct shapes: bimetallic nanocubes with 67 $\pm$ 3 nm edge length (~55%), and nanopyramids with 86 $\pm$

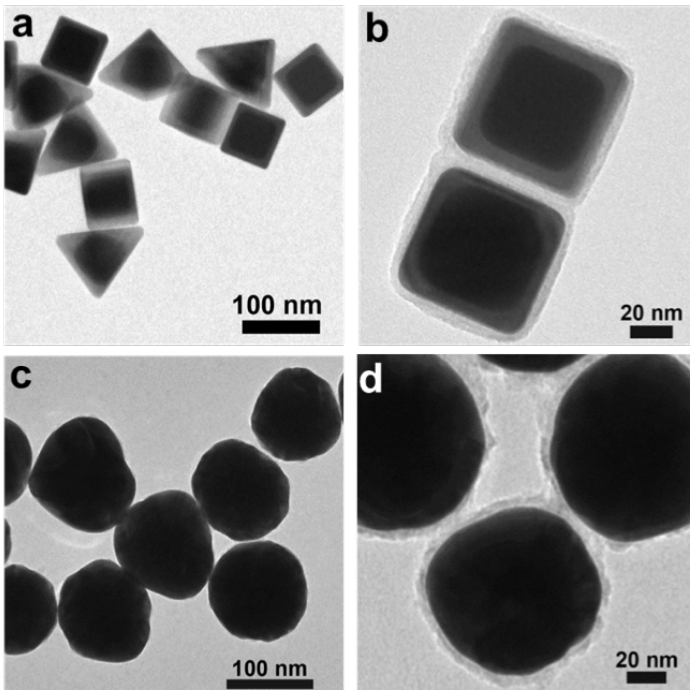

Figure 2.1: Transmission electron micrographs of (a) Au-Ag nanostructures and (b) after coating with 5 nm layer silica, (c) Au nanoparticles and (d) after coating with a 5 nm layer silica.

4 nm side length and 98 $\pm$ 4 nm base length (~45%). The rounded corner Au nanocube cores drives nucleation and growth of bimetallic nanocubes, while truncated nanocubes drive the growth of nanopyramids.[30] Transmission electron micrographs of Au-AgNSs (Figure 2.1a) show the high contrast Au core surrounded by lower contrast Ag shell. The Au-AgNSs are coated in a 5 nm layer of silica (Au-Ag@SiO_2, Figure 2.1b). The silica layer has multiple purposes: *(i)* since metals are electron scavengers, the insulating silica spacer minimizes recombination of electron-hole (e^-/h^+) pairs on the metal surface; *(ii)* silica layer minimizes Ostwald ripening during annealing of the photoanode; and *(iii)* silica layer also protects the nanostructures from the corrosive basic electrolyte. The plasmon enhanced water splitting ability of bimetallic nanostructures was compared with 85 nm diameter AuNPs (Figure 2.1c) which were also coated with a uniform, thin layer of silica (Au@SiO_2, Figure 2.2d).

Plasmonic enhancement of solar devices is contributed by the absorption and scatter-

ing cross-sections of nanostructures. To understand these optical characteristics of the different shapes observed experimentally, finite difference time domain (FDTD) simulations were performed. Calculated absorption, scattering, and extinction spectra of bimetallic nanocubes (Figure 2.2a) show a dipolar mode centered at 560 nm and a quadrupolar mode at 490 nm and other higher order multipole modes associated with the nanocube corners.[32] Calculated spectra for bimetallic nanopyramids show dual resonances when excited with a perpendicularly polarized light due to excitation of both dipole and quadrupole modes (Figure 2.2b). The dipole resonance is observed at 720 nm, the quadrupole resonance at 600 nm, and other higher order modes are observed due to excitation of the various corners of the pyramids.[30] The near-field intensity plot indicates intense electromagnetic fields localized on the edges and corners at the dipole resonance of nanocubes (Figure 2.2e-i) and nanopyramids (Figure 2.2e-ii). Calculations of AuNPs show a dipole resonance centered at 555 nm with stronger absorption relative to scattering (Figure 2.2c). Simulations demonstrate that the overall optical characteristics of Au-Ag nanocubes and nanopyramids combined together supersede those of AuNPs; the presence of the nanopyramids also gives rise to near-infrared resonances enabling broadband light absorption.

The experimental extinction spectra of Au-Ag@SiO_2 nanostructures exhibit dual plasmon resonances (Figure 2.2d) centered at 535 nm which is primarily attributed to the nanocubes and at 630 nm which is due to the nanopyramids. While the experimental dipole modes of Au-Ag nanocubes matches well with calculated spectra, for the nanopyramids the dipole and quadrupole mode are overlapped into a single peak in experiments relative to simulations. This difference in spectral characteristics between experiments and simulations is likely attributed to two factors: *(i)* heterogeneities in the nanopyramids shape and size resulting from the synthesis process, and *(ii)* calculated spectra of nanopyramids represent a perfectly symmetric Au core within the Ag shell, but experimentally we either observe an outer shell of non-uniform thickness or a nonconcentric alignment of the core and shell. This results in symmetry breaking allowing quadrupolar modes to hybridize

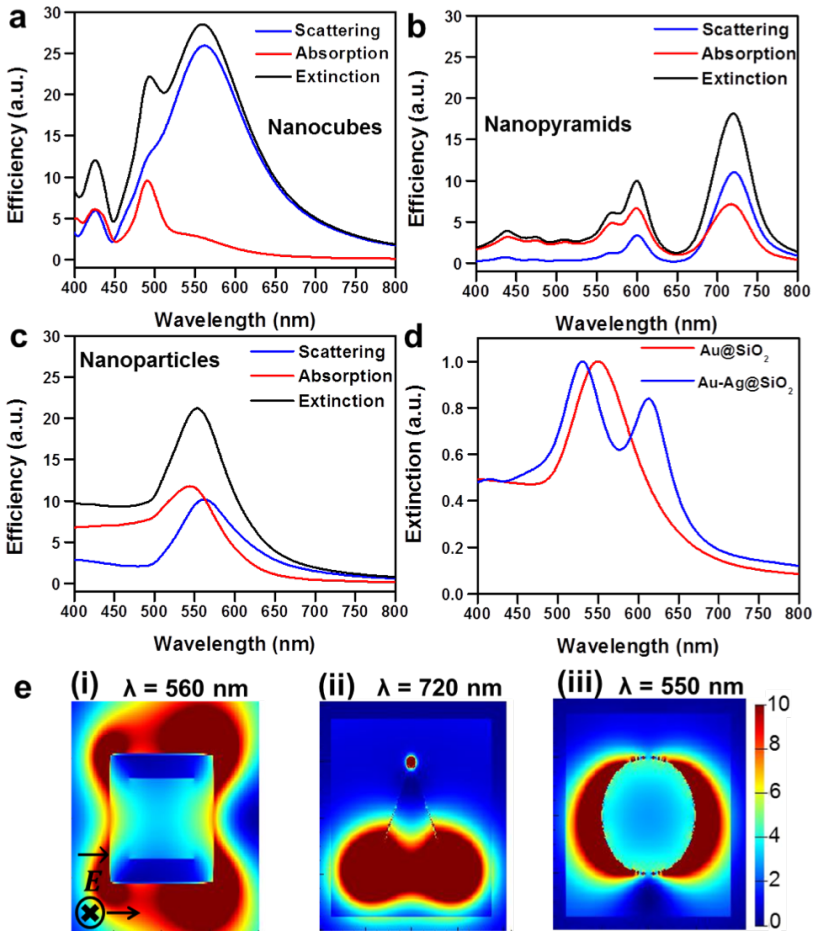

Figure 2.2: Calculated absorption, scattering, and extinction spectra obtained from FDTD simulations of (a) Au-Ag nanocubes, (b) Au-Ag nanopyramids, and (c) Au nanoparticles. (d) Experimental extinction spectra of $Au@SiO_2$ nanoparticles with a plasmon resonance at 560 nm and $Au\text{-}Ag@SiO_2$ nanostructures showing dual resonances at 535 nm and 630 nm. (e) Electromagnetic intensity profile, $<E^2/E_0^2>$, of (i) Au-Ag nanocubes, (ii) Au-Ag nanopyramids, and (iii) Au nanoparticles. Profiles were collected at the dipole resonance of each shape. A plane wave of intensity unity was injected along the x-axis with propagation occurring along the y-axis. Color bars represent intensities of the resulting electric fields.

with dipolar modes which results in single strong peak in experiments red-shifted from the calculated quadrupole mode and blue-shifted from the simulated dipole mode. The experimental plasmon resonance of Au@SiO_2 nanoparticles centered at 550 nm overlaps well with calculations.

Following synthesis, Au@SiO_2-NPs and Au-Ag@SiO_2-NSs were embedded in photoanodes mixed with 20 nm mesoporous TiO_2 (P25). A detailed characterization and size analysis of the mesoporous TiO_2 nanoparticles is shown in Figure 2.3. The mesoporous TiO_2 is beneficial to device performance due to the large surface area in contact with electrolyte per unit volume. Due to the large bandgap of TiO_2, control photoanodes (TiO_2 only) show minimal absorbance in the visible (Figure 2.4a). The photoanodes with Au@SiO_2-NPs exhibit an enhanced absorption in the visible region relative to the control; however, due to the overall poor extinction cross-section of spherical AuNPs and high Ohmic losses the absorption enhancement is not significant. Photoanodes with Au-Ag@SiO_2-NSs increased the overall absorption through the full spectral range from 350-750 nm. This improved absorption is attributed to the multiple plasmon resonances of Au-Ag@SiO_2-NSs spanning the entire visible spectrum. Additionally, due to high dielectric constant of TiO_2 ($\varepsilon > 8$) the plasmon resonances of Au-Ag@SiO_2 are expected to red-shift in the TiO_2 nanoparticle film which explains the absorption enhancement beyond 650 nm. We note spherical nanoparticles are typically less sensitive in sensing the change in refractive index of surrounding medium relative to nanocubes and nanopyramids. The enhanced absorption is also attributed to the overall larger extinction cross-section of Au-AgNSs relative to AuNPs as observed in simulations (Figure 2.2).

The photocatalytic water splitting ability of photoanodes were analyzed in a three-electrode set-up with Pt counter electrode and Ag/AgCl reference electrode under AM 1.5G illumination (100 mW/cm^2). Relative to control, IPCE of plasmon-enhanced photoanodes (Figure 2.4b) demonstrate an increase in photocurrent in the visible for the Au@SiO_2-NPs embedded photoanodes, and both visible and near-infrared for the Au-Ag@SiO_2-NSs pho-

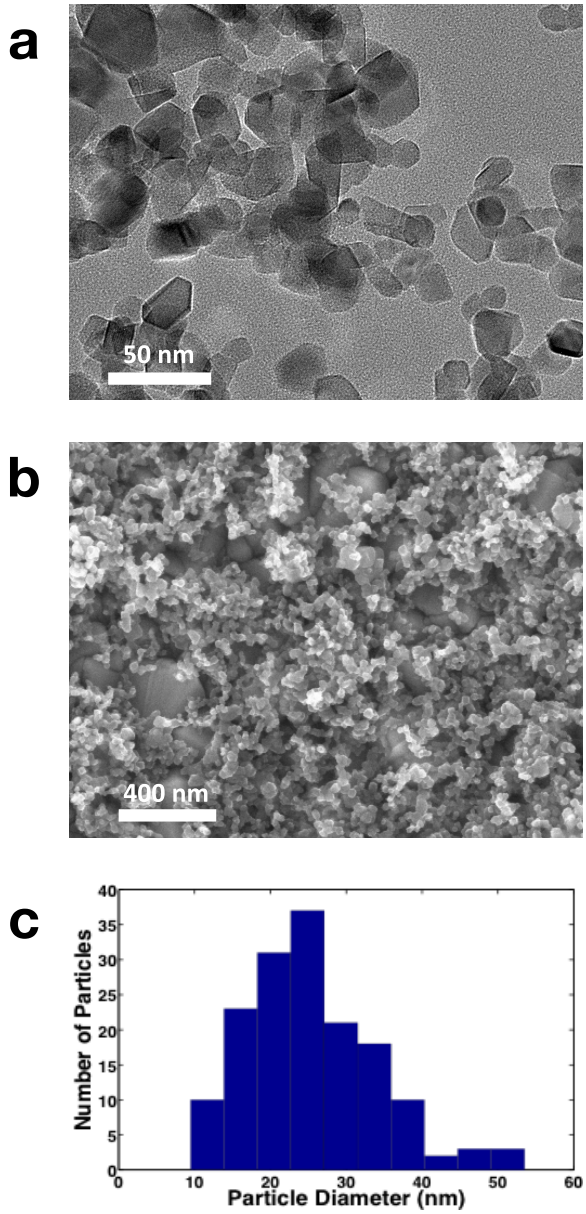

Figure 2.3: (a) Representative transmission electron micrograph of P25 nanoparticles. (b) Scanning electron micrograph of mesoporous morphology of P25 nanoparticles on FTO glass. (c) Size distribution of P25 nanoparticles, the average size is 23 nm.

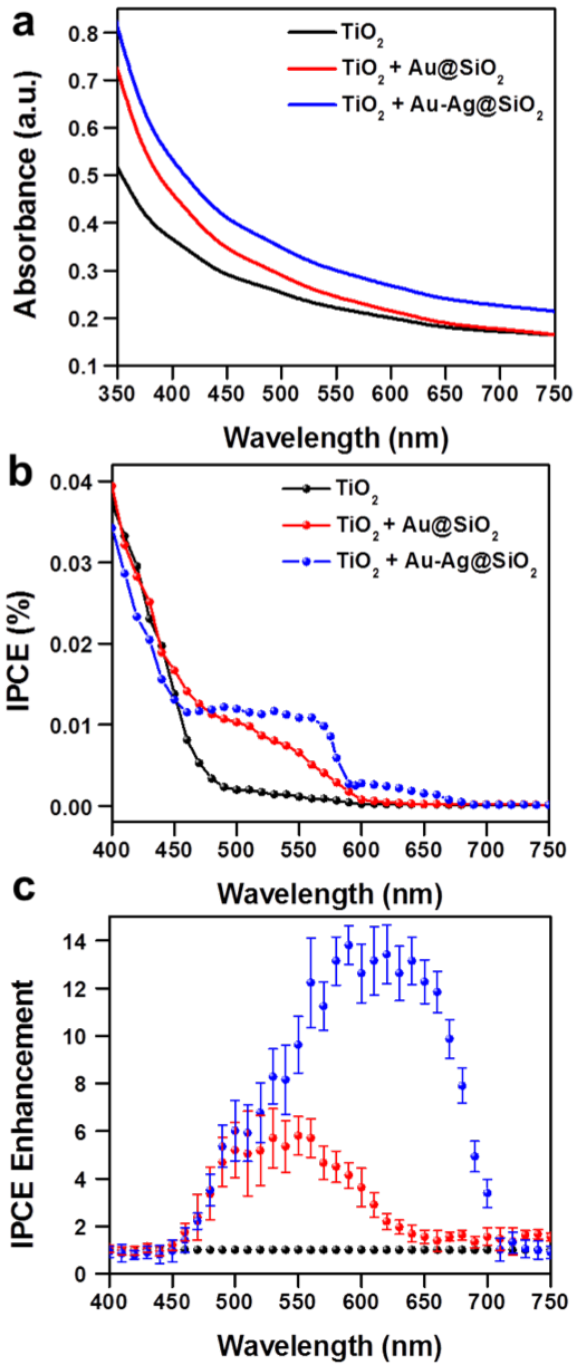

Figure 2.4: (a) Absorption spectra showing enhancement in light absorption with Au-Ag@SiO_2 nanostructures (blue) and Au@SiO_2 nanoparticles (red) embedded within the mesoporous TiO_2 photoanodes relative to TiO_2 only anodes (control, black). (b) Incident photon to charge carrier efficiency (IPCE) curves of non-enhanced (TiO_2 only) and plasmon enhanced photoanodes. The plasmon enhanced photoanodes are at the optimized concentration. (c) Enhancement in photocurrent as a function of wavelength obtained from IPCE data of plasmon enhanced photoanodes relative to TiO_2 only photoanodes. The error bars were obtained from >4 devices.

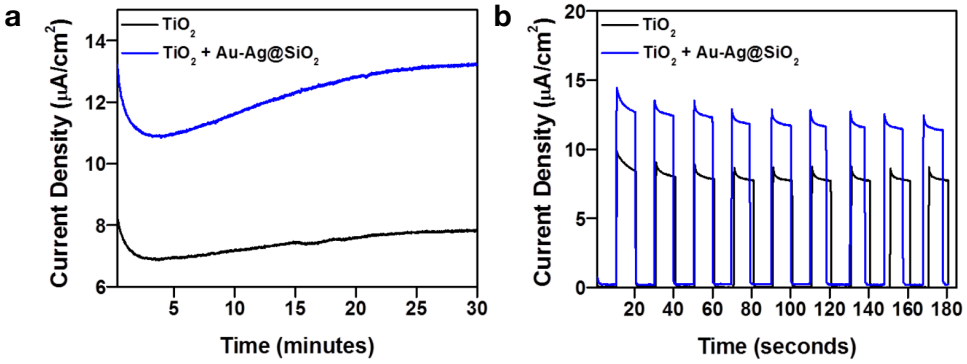

Figure 2.5: (a) Chronoamperometry measurement of reference photoanode (TiO_2) and plasmon enhanced photoanode (TiO_2 + Au-Ag@SiO_2), and (b) Light-chopping measurement of the two photoanodes shown in a.

toanodes. A slight decrease in photocurrent over the spectral range from 400-450 nm was observed attributable to reduction in the photon flux that reaches the TiO_2 surface due to presence of the metal nanostructures. IPCE enhancement as a function of wavelength was obtained from by dividing the IPCE intensity of plasmon enhanced photoanodes by control photoanodes (Figure 2.4c). IPCE enhancements correlate well with corresponding plasmon resonances of the embedded nanostructures. While photoanodes incorporated with Au@SiO_2-NPs show 6$\times$ enhancement in the visible region consistent with that observed previously with AuNPs,[33] photoanodes with Au-Ag@SiO_2-NSs demonstrate a 14$\times$ enhancement distributed across the visible and near-infrared. We also performed chronoamperometric measurements at 0 V vs. RHE for both plasmon enhanced and non-enhanced photoanodes and observed stable photocurrent over 30 minutes for both devices, as shown in Figure 2.5.

The increased photocurrent in the presence of plasmonic nanostructures is attributed to two phenomena: *(i)* metal nanostructures behave as antennas where the plasmonic near field is coupled to the semiconductor thereby increasing the total absorption cross-section, *(ii)* metal nanostructures serve as sub-wavelength scatterers to couple and trap solar energy into the absorbing semiconductor layer. Relative to spherical nanostructures, a higher

concentration of charges are localized at the corners and edges of cubic and pyramidal morphologies due to the lightning-rod effect which gives rise to strong local fields that decays tens of nanometers from the nanostructure surface. These confined fields can serve as a secondary light source, increasing optical interactions with proximal materials and resulting in a higher density of e^-/h^+ pairs than is possible with visible illumination alone. The bimetallic nanostructures (particularly nanocubes, see Figure 2.2) have a high scattering cross-section, which also contributes to the enhanced photocurrent. Light scattered from nanostructures into the semiconductor beyond the critical angle of reflection passes several times through the semiconductor and remains trapped. This phenomenon increases the semiconductor optical path length and improves light absorption.

A third mechanism has also been proposed where following photo-excitation at the plasmon resonance, plasmons will decay by energetic relaxation generating e^-/h^+ pairs. These photo-excited electrons undergo electron-electron scattering resulting in a non-equilibrium hot electron distribution. The process of hot electron conduction in metal nanoparticles is dependent on the electron mean free path, λ_e, of the metal; for Au and Ag λ_e is on the order of 50 nm.[34, 35] This suggests for metal nanoparticles $<$50 nm hot electrons can rapidly transfer to the semiconductor near the metal surface (in the absence of an insulating barrier such as silica) and initiate efficient photochemical reactions.[36, 37, 38] However, for metal nanoparticles $>$50 nm in size, such as the Au-Ag NSs and AuNPs used in this work, fewer hot electrons reach the metal surface due to scattering. The hot carriers that reach the Au/SiO_2 interface must now pass the electron tunneling barrier, Φ_b, of the insulating SiO_2; for SiO_2 Φ_b is $<$3 nm.[39, 40] Since the silica layer thickness of $Au@SiO_2$-NPs and $Au-Ag@SiO_2$-NSs is ~5 nm, it is highly unlikely hot electrons will transfer to the surrounding TiO_2, suggesting the hot electron mechanism does not play a role in our system. The higher enhancements by $Au-Ag@SiO_2$-NSs also results from the dual plasmon resonances allowing broadband incident light absorption. We also note that the observed enhancements in photocurrent suggests that the nanostructures are within 10-20 nm from the semiconduc-

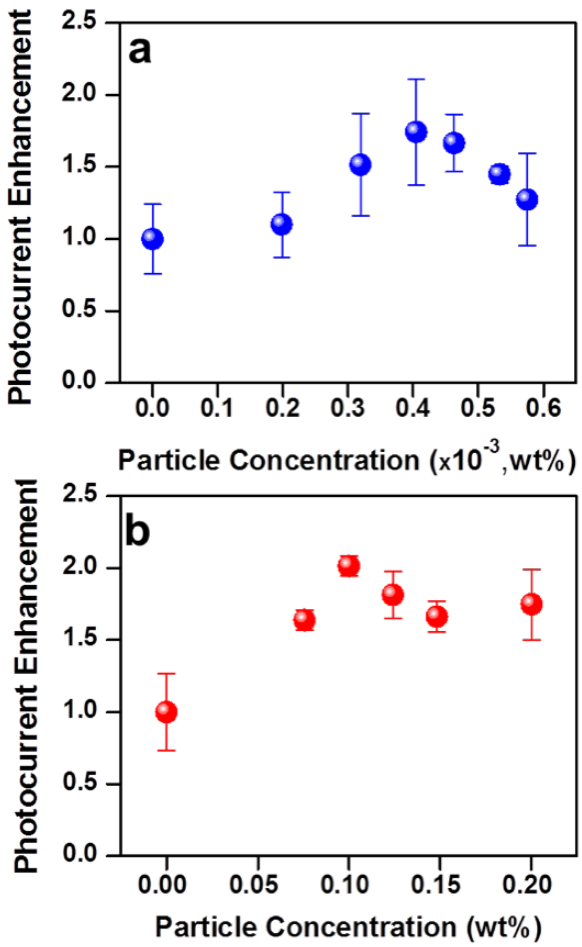

Figure 2.6: The photocurrent enhancement of photoanodes as a function of particle concentration in wt.% with (a) Au-Ag@SiO_2 nanostructures, and (b) Au@SiO_2 nanoparticles embedded within the mesoporous TiO_2. Note: The maximum photocurrent densities are achieved with three orders of magnitude less Au-Ag@SiO_2 nanostructures relative to Au@SiO_2 nanoparticles. Error bars were achieved from 4 photoanodes per concentration.

tor/electrolyte interface; since minority carrier diffusion length for TiO_2 is on the order of 10-100 nm only e^-/h^+ pairs generated within this distance of semiconductor/electrolyte interface contribute to photocatalytic water splitting. [41, 42, 43]

We varied the concentration of Au-Ag@SiO_2-NSs and Au@SiO_2-NPs in the photoanodes to determine the dependence of particle density to photocurrents. Particle densities were determined by correlating the absorbance of nanostructures to weight of the dried nanostructures determined via thermogravimetric analysis (TGA). We observed a clear trend in nanostructure concentration dependence to photocurrent for both Au-Ag@SiO_2-

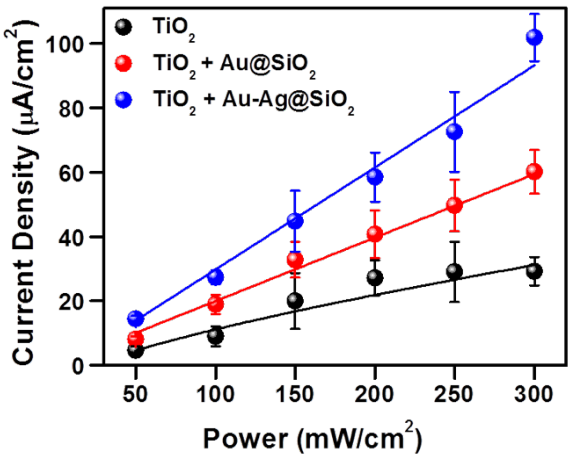

Figure 2.7: Correlation of photocurrent to light intensity (power) of photoanodes with Au-Ag@SiO_2 nanostructures (blue) and Au@SiO_2 nanoparticles (red) embedded within the mesoporous TiO_2 photoanods relative to TiO_2 only photoanodes. The power dependence of the samples is: Au-Ag@SiO_2 $\propto$ Intensity 1.2, Au@SiO_2 $\propto$ Intensity 0.94, and TiO_2 $\propto$ Intensity 0.55. Error bars were achieved from four photoanodes measured at each light intensity.

NSs and Au-Ag@SiO_2-NPs (Figure 2.6). Photocurrent density monotonically increased reaching a maximum at 4.5×10^{-4} wt.% Au-Ag@SiO_2-NSs and then decreased with further increase in particle density. For Au@SiO_2-NPs photocurrent reached a maximum at 1×10^{-1} wt.% and then decreased and leveled off. To achieve similar photocurrent enhancements three orders of magnitude fewer particles are needed for Au-Ag@SiO_2-NSs relative to Au@SiO_2-NPs which demonstrates significantly less material is required to achieve plasmonic enhancement of solar devices with bimetallic nanostructures relative to monometallic nanoparticles. The decrease in photocurrent at high particle concentrations is attributed to: *(i)* at high particle densities the total available photon flux reaching TiO_2 is significantly decreased resulting in fewer e^-/h^+ pairs being generated; *(ii)* increasing concentration of metal increases e^-/h^+ recombination decreasing carriers available for photocurrent generation; and *(iii)* increased particle density promoting interparticle interaction between adjacent nanostructures giving rise to heat generation. The dissipation of this heat increases the phonon density relative to the carrier density available for photocurrent generation which reduced the current density of photoanodes.

To further understand the role of plasmonic nanostructures in increased charge carrier generation at the semiconductor surface, the photocurrents of the samples were analyzed by modulating intensity of the solar simulated light from 50 mW/cm^2 to 300 mW/cm^2. Photoanodes incorporated with Au-Ag@SiO_2-NSs and Au@SiO_2-NPs (Figure 2.7) exhibit first-order intensity dependence, while control photoanodes show half-order intensity dependence. If the observed photocurrent is directly correlated to the concentration of h^+ on the TiO_2 surface, that indicates the surface concentration of h^+ follows a first- and half-order dependence for the plasmon enhanced, and control photoanodes respectively. Studies have shown that e^-/h^+ pairs formed in the bulk of TiO_2 shows a half-order dependence on photon flux, whereas charge carriers formed near the surface of TiO_2 show a first-order dependence on light intensity.[41, 44, 45] These results provide further evidence that in the nanostructure embedded photoanodes charge carriers generated near the surface of the TiO_2 are primarily enhanced by the intense electromagnetic fields of the proximal plasmonic nanostructures. This effect is further augmented in the photoanodes integrated with Au-Ag@SiO_2-NSs giving rise to higher photocurrent densities as a function of incident light intensity relative to the photoanodes with Au@SiO_2-NPs.

2.4 Conclusions

We compared the plasmon enhanced photocatalytic water splitting capability of Au-Ag bimetallic nanostructures with monometallic Au nanoparticles incorporated in mesoporous TiO_2 photoanodes. Bimetallic nanostructures embedded photoanodes demonstrated significantly improved photocurrent densities relative to those with Au nanoparticles. Our experiments and simulations attribute these enhancements to the dual plasmon resonance of bimetallic nanostructures resulting in broadband absorbance of incident light across the visible and near-infrared, large electric field enhancements localized on the edges and corners of the nanostructures, and large scattering cross-sections resulting in enhanced optical absorption in the TiO_2 photoanodes. These near-field and far-field properties of bimetal-

lic nanostructures collectively result in an increased e^-/h^+ pair generation at the surface of the vicinal TiO_2 particles; these charge carriers can subsequently separate and migrate to the semiconductor/electrolyte interface initiating photochemical reactions. We also observed to achieve similar photocurrent enhancements three orders of magnitude less wt.% of bimetallic nanostructures was required relative to Au nanoparticles in TiO_2 photoanodes demonstrating that bimetallic nanostructures will ultimately enable thin film solar devices with enhanced efficiencies. Beyond water splitting, these bimetallic-semiconductor hybrid architectures can be generalized to a range of applications including solar cells, solid-state sensors, light induced CO_2-to-fuel conversion, and photodetectors.

2.5 Methods

A. Nanostructure Synthesis. AuNPs were prepared via a potassium carbonate reduction method.[46] A solution containing 250 mL of Milli-Q water, 3.75 mL of 1% chloroauric acid and 6.25 mg of potassium carbonate was allowed to age in a dark place for two days. After aging, 1.25 mL of 27% aqueous formaldehyde was added to the solution under rapid stirring. The solution was allowed to react for approximately 15 minutes, or until it turned orange/brown showing scattering from AuNPs. The peak plasmon resonance was at 550 nm. Au-Ag NSs were prepared via a seed mediated growth process.[30] Au seeds were prepared by adding 0.6 mL of freshly prepared and ice cold 10 mM $NaBH_4$ to an aqueous solution composed of 7.5 mL of 100 mM cetyltrimethylammonium bromide (CTAB), 2.75 mL milli-Q water (18.2 MΩ), and 0.8 mL of 10 mM $HAuCl_4$. This solution was stirred vigorously for 1 minute and then transferred to a 35 °C water bath, where it was left undisturbed for one hour. A growth solution was prepared by the sequential addition of 6.4 mL of 100 mM CTAB, 0.8 mL of 10 mM $HAuCl_4$, and 3.8 mL of 100 mM ascorbic acid to 32 mL of milli-Q H_2O. The seed solution was diluted by a factor of ten with milli-Q H_2O. The 20 mL of diluted seed solution was added to the growth solution, mixed gently by inversion, and then left undisturbed at 35 °C for 5 hours. The Au nanocrystal suspen-

sion was centrifuged at 1100 RCF for 12 minutes ($\times$ 3) and washed and soaked in 20 mM cetyltrimethylammonium chloride (CTAC) for 15 minutes. The Au nanocrystals were then redispersed in 333 μL of H_2O for use as precursor solution for Ag growth. Typically, 200 μL of precursor solution and 50 μL of 10 mM KBr were added to 5 mL of 20 mM CTAC and heated in a 65 °C water bath for 10 minutes before adding in 50 mL of 10 mM $AgNO_3$ and 150 mL of 100 mM ascorbic acid. The solution was mixed gently by inversion and left undisturbed at 65 °C for one hour.

B. Nanostructure Silica Coating. Silica coating for both AuNPs and Au-Ag NSs was accomplished by a modified procedure in the literature.[47] A sodium silicate solution was freshly prepared before use by adding 2 mL of 27% sodium silicate solution to a 100 mL beaker while stirring, in addition to 60 mL of 0.1 M HCl and 40 mL milli-Q water. The resulting solution of 0.54% sodium silicate was adjusted to pH 10.2 with 5 N HCl. Next, 18.3 μL of APTES (97 wt%) is added to 100 mL H_2O and stirred briefly. As prepared nanoparticle solution (30 mL) was added to a 50 mL round bottom flask, in addition to 400 μL of freshly prepared APTES solution, and stirred for 15 minutes. Sodium silicate solution (1.4 mL) was then added to the nanostructure suspension, which was then placed in an oil bath at 90 °C for eight hours. After the reaction reached the desired growth thickness, it was quenched in an ice bath for 15 minutes, followed by a 15 minute centrifuge at 1500 rcf ($\times$2)

C. Nanostructure Characterization. A Varian Cary 5000 UV-vis NIR spectrophotometer (Agilent Technologies) with dual beam capability was used to measure the extinction of the AuNPs and Au-Ag NSs in aqueous media using a 1 cm path length cuvette. The nanoparticle size, geometry, and composition were characterized using an FEI Osiris TEM at 200 keV. Nanostructure concentrations were determined by performing thermogravimetric analysis on Instrument Specialist's TGA-1000; all nanostructures were heated to 600 °C at the rate of 20 °C/min.

D. Anode Fabrication. FTO glass (MTI) was cut into 1" $\times$ 1/2" pieces and cleaned via suc-

cessive 30 minute sonication cycles in IPA/Acetone with 1% Triton-X and then IPA/Acetone, followed by a thorough drying with nitrogen. A solution was prepared with 3 mL ethanol, 0.1 g of P25 and varied amounts of metal nanostructures; the solution was spin coated onto the substrate for 30 seconds at 600 rpm, followed by 60 seconds at 800 rpm. Following spin coating, anodes were annealed at 450 °C for 45 minutes to ensure that TiO_2 was fully converted to anatase phase.

E. Electrochemical Measurements and IPCE. Photocatalytic water splitting capability of anodes was tested over a potential range of -1 to 1 V at a scan rate of 50 mV/s under AM 1.5G illumination (100 mW/cm^2) with a Newport solar simulator and power supply. An average area of 0.2 cm^2 was illuminated. Electrochemical measurements were conducted in a three electrode setup. A Pt foil was used as the counter electrode, Ag/AgCl was used as a reference electrode. A MetroOhm PGSTAT101 potentiostat was used for all electrochemical measurements. Incident photon to charge carrier efficiency (IPCE) measurements were conducted with a Newport system with a 300 W Xe light source, monochromator, and Si detector.

F. Electrodynamic Simulations. Finite difference time domain (FDTD) simulations were performed using commercial Lumerical software. Simulations were performed on single particles in water as the surrounding medium using a total-field scattered-field (TFSF) plane wave source and a 7 angstrom mesh. The simulated Au-Ag nanocube had a 50 nm Au core and a 12.5 nm Ag shell. The simulated Au-Ag nanopyramid had a 60 nm edge length for the Au core and a 20 nm thick Ag shell. The simulated Au nanosphere had a diameter of 85 nm.

2.6 Bibliography

[1] Hyung Gyu Park and Jason K. Holt. Recent advances in nanoelectrode architecture for photochemical hydrogen production. *Energy Environ. Sci.*, 3(8):1028–1036, 2010.

[2] Scott C. Warren, Kislon Voïtchovsky, Hen Dotan, Celine M. Leroy, Maurin Cornuz, Francesco Stellacci, Cécile Hébert, Avner Rothschild, and Michael Grätzel. Identifying champion nanostructures for solar water-splitting. *Nat. Mater.*, 12(9):842–849, 2013.

[3] Michael G. Walter, Emily L. Warren, James R. McKone, Shannon W. Boettcher, Qixi Mi, Elizabeth A. Santori, and Nathan S. Lewis. Solar water splitting cells. *Chem. Rev.*, 110(11):6446–6473, 2010.

[4] Takashi Hisatomi, Jun Kubota, and Kazunari Domen. Recent advances in semiconductors for photocatalytic and photoelectrochemical water splitting. *Chem. Soc. Rev.*, 43(22):7520–7535, 2014.

[5] Suljo Linic, Phillip Christopher, and David B. Ingram. Plasmonic-metal nanostructures for efficient conversion of solar to chemical energy. *Nat. Mater.*, 10(12):911–921, 2011.

[6] Fuding Lin and Shannon W. Boettcher. Adaptive semiconductor/electrocatalyst junctions in water-splitting photoanodes. *Nat. Mater.*, 13(1):81–86, 2014.

[7] A. J. Cowan, Junwang Tang, Wenhua Leng, James R. Durrant, and David R. Klug. Water Splitting by Nanocrystalline TiO2 Limited by Charge Recombination in a Complete Photoelectrochemical Cell Exhibits Efficiencies. *J. Phys. Chem. C*, 114(9):4208–4214, 2010.

[8] Ilkay Cesar, Kevin Sivula, Andreas Kay, Radek Zboril, and Michael Grätzel. Influence of Feature Size, Film Thickness, and Silicon Doping on the Performance of Nanostructured Hematite Photoanodes for Solar Water Splitting. *J. Phys. Chem. C*, 113(2):772–782, 2009.

[9] Yidong Hou, Billie L. Abrams, Peter C. K. Vesborg, Mårten E. Björketun, Konrad Herbst, Lone Bech, Alessandro M. Setti, Christian D. Damsgaard, Thomas Pedersen, Ole Hansen, Jan Rossmeisl, Søren Dahl, Jens K. Nørskov, and I. Chorkendorff. Bioinspired molecular co-catalysts bonded to a silicon photocathode for solar hydrogen evolution. *Nat. Mater.*, 10(6):434–438, 2011.

[10] Hanwei Gao, Chong Liu, Hoon Eui Jeong, and Peidong Yang. Plasmon-enhanced photocatalytic activity of iron oxide on gold nanopillars. *ACS Nano*, 6(1):234–240, 2012.

[11] Jiangtian Li, Scott K. Cushing, Peng Zheng, Fanke Meng, Deryn Chu, and Nianqiang Wu. Plasmon-induced photonic and energy-transfer enhancement of solar water splitting by a hematite nanorod array. *Nat. Commun.*, 4:2651, 2013.

[12] Ying Chih Pu, Gongming Wang, Kao Der Chang, Yichuan Ling, Yin Kai Lin, Bob C. Fitzmorris, Chia Ming Liu, Xihong Lu, Yexiang Tong, Jin Z. Zhang, Yung Jung Hsu, and Yat Li. Au nanostructure-decorated TiO2 nanowires exhibiting photoactivity across entire UV-visible region for photoelectrochemical water splitting. *Nano Lett.*, 13(8):3817–3823, 2013.

[13] Zhaoyao Zhan, Jianing An, Huanchao Zhang, Reinack Varghese Hansen, and Lianxi Zheng. Three-dimensional plasmonic photoanodes based on Au-embedded TiO 2 structures for enhanced visible-light water splitting. *ACS Appl. Mater. Interfaces*, 6(2):1139–1144, 2014.

[14] Xu Shi, Kosei Ueno, Naoki Takabayashi, and Hiroaki Misawa. Plasmon-Enhanced Photocurrent Generation and Water Oxidation with a Gold Nanoisland-Loaded Titanium Dioxide Photoelectrode. *J. Phys. Chem. C*, 117(6):2494–2499, 2013.

[15] Vincenzo Giannini, Antonio I. Fernández-Domínguez, Susannah C. Heck, and Stefan A. Maier. Plasmonic nanoantennas: Fundamentals and their use in controlling the radiative properties of nanoemitters. *Chem. Rev.*, 111(6):3888–3912, 2011.

[16] Michael B. Cortie and Andrew M. McDonagh. Synthesis and Optical Properties of Hybrid and Alloy Plasmonic Nanoparticles. *Chem. Rev.*, 111:3713–3735, 2011.

[17] Alberto G. Curto, Giorgio Volpe, Tim H. Taminiau, Mark P. Kreuzer, Romain Quidant, and Niek F. Van de Hulst. Unidirectional Emission of a Quantum Dot Coupled to a Nanoantenna. *Science*, 329:930–933, 2010.

[18] Julien Claudon, Joël Bleuse, Nitin Singh Malik, Maela Bazin, Perine Jaffrennou, Niels Gregersen, Christophe Sauvan, Philippe Lalanne, and Jean-Michel Gerard. A highly efficient single-photon source based on a quantum dot in a photonic nanowire. *Nat. Photonics*, 4(3):174–177, 2010.

[19] Rizia Bardhan, Nathaniel K. Grady, Tamer Ali, and Naomi J. Halas. Metallic nanoshells with semiconductor cores: Optical characteristics modified by core medium properties. *ACS Nano*, 4(10):6169–6179, 2010.

[20] Rizia Bardhan, Nathaniel K. Grady, and Naomi J. Halas. Nanoscale control of near-infrared fluorescence enhancement using au nanoshells. *Small*, 4(10):1716–1722, 2008.

[21] Joun Lee, Syed Mubeen, Xiulei Ji, Galen D. Stucky, and Martin Moskovits. Plasmonic photoanodes for solar water splitting with visible light. *Nano Lett.*, 12(9):5014–5019, 2012.

[22] Syed Mubeen, Joun Lee, Nirala Singh, Stephan Krämer, Galen D. Stucky, and Martin Moskovits. An autonomous photosynthetic device in which all charge carriers derive from surface plasmons. *Nat. Nanotechnol.*, 8(4):247–251, 2013.

[23] Stafford W. Sheehan, Heeso Noh, Gary W. Brudvig, Hui Cao, and Charles A. Schmuttenmaer. Plasmonic enhancement of dye-sensitized solar cells using core-shell-shell nanostructures. *J. Phys. Chem. C*, 117:927–934, 2013.

[24] Marina Stavytska-Barba, Michael Salvador, Abhishek Kulkarni, David S. Ginger, and Anne Myers Kelley. Plasmonic enhancement of Raman scattering from the organic solar cell material P3HT/PCBM by triangular silver nanoprisms. *J. Phys. Chem. C*, 115(42):20788–20794, 2011.

[25] Matthew Rycenga, Moon Ho Kim, Pedro H. C. Camargo, Claire Cobley, Zhi-yuan Li, and Younan Xia. Surface-Enhanced Raman Scattering : Comparison of Three Different Molecules on Single-Crystal Nanocubes and Nanospheres of Silver Surface-Enhanced Raman Scattering : Comparison of Three Different Molecules on Single-Crystal Nanocubes and Nanospheres of Si. *J. Phys. Chem. A*, 113:3932–3939, 2009.

[26] Joseph A. Webb, William R. Erwin, Holly F. Zarick, Jayde Aufrecht, Harris W. Manning, Matthew J. Lang, Cary L. Pint, and Rizia Bardhan. Geometry-Dependent Plasmonic Tunability and Photothermal Characteristics of Multibranched Gold Nanoantennas. *J. Phys. Chem. C*, 118(7):3696–3707, 2014.

[27] Mohamed Haggui, Montacer Dridi, Jerome Plain, Sylvie Marguet, Henri Perez, George C. Schatz, Gary P. Wiederrecht, Stephen K. Gray, and Renaud Bachelot. Spatial confinement of electromagnetic hot and cold spots in gold nanocubes. *ACS Nano*, 6(2):1299–1307, 2012.

[28] Wenbo Hou and Stephen B. Cronin. A review of surface plasmon resonance-enhanced photocatalysis. *Adv. Funct. Mater.*, 23(13):1612–1619, 2013.

[29] Akshaya K. Samal, Lakshminarayana Polavarapu, Sergio Rodal-Cedeira, Luis M. Liz-Marzán, Jorge Pérez-Juste, and Isabel Pastoriza-Santos. Size tunable Au@Ag core-shell nanoparticles: Synthesis and surface-enhanced raman scattering properties. *Langmuir*, 29(48):15076–15082, 2013.

[30] Holly F. Zarick, William R. Erwin, Jayde Aufrecht, Andrew Coppola, Bridget R. Rogers, Cary L. Pint, and Rizia Bardhan. Morphological modulation of bimetallic nanostructures for accelerated catalysis. *J. Mater. Chem. A*, 2(19):7088, 2014.

[31] H. Mertens and A. Polman. Strong luminescence quantum-efficiency enhancement near prolate metal nanoparticles: Dipolar versus higher-order modes. *J. Appl. Phys.*, 105(4):044302, 2009.

[32] Jianxiao Gong, Fei Zhou, Zhiyuan Li, and Zhiyong Tang. Synthesis of Au-Ag Core-Shell Nanocubes Containing Varying Shaped Cores and Their Localized Surface Plasmon Resonances. *Langmuir*, 28:8959–8964, 2012.

[33] Zuwei Liu, Wenbo Hou, Prathamesh Pavaskar, Mehmet Aykol, and Stephen B. Cronin. Plasmon resonant enhancement of photocatalytic water splitting under visible illumination. *Nano Lett.*, 11(3):1111–1116, 2011.

[34] Fuming Wang and Nicholas A. Melosh. Power-independent wavelength determination by hot carrier collection in metal-insulator-metal devices. *Nat. Commun.*, 4:1711, 2013.

[35] Fuming Wang and Nicholas A. Melosh. Plasmonic Energy Collection through Hot Carrier Extraction. *Nano Lett.*, 11(12):5426–5430, 2011.

[36] Shaunak Mukherjee, Linan Zhou, Amanda M. Goodman, Nicolas Large, Ciceron Ayala-Orozco, Yu Zhang, Peter Nordlander, and Naomi J. Halas. Hot-Electron-Induced Dissociation of H2 on Gold Nanoparticles Supported on SiO2. *J. Am. Chem. Soc.*, 136(1):64–67, 2014.

[37] Louis Brus. Noble Metal Nanocrystals: Plasmon Electron Transfer Photochemistry and Single-Molecule Raman Spectroscopy. *Acc. Chem. Res.*, 41(12):1742–1749, 2008.

[38] Prashant K. Jain, Wei Qian, and Mostafa A. El-Sayed. Ultrafast Cooling of Photoexcited Electrons in Gold NanoparticleThiolated DNA Conjugates Involves the Dissociation of the GoldThiol Bond. *J. Am. Chem. Soc.*, 128(7):2426–2433, 2006.

[39] Wen-chin Lee and Chenming Hu. Modeling CMOS Tunneling Currents Through Ultrathin Gate Oxide Due to Conduction- and Valence-Band Electron and Hole Tunneling. *IEEE Trans. Electron Devices*, 48(7):1366–1373, 2001.

[40] Chu-Hsuan Lin and Chee Wee Liu. Metal-insulator-semiconductor photodetectors. *Sensors*, 10(10):8797–8826, 2010.

[41] David B. Ingram and Suljo Linic. Water Splitting on Composite Plasmonic-Metal/Semiconductor Photoelectrodes: Evidence for Selective Plasmon-Induced Formation of Charge Carriers near the Semiconductor Surface. *J. Am. Chem. Soc.*, 133:5202–5205, 2011.

[42] W. H. Leng, Piers R. F. Barnes, Mindaugas Juozapavicius, Brian C. O'Regan, and James R. Durrant. Electron Diffusion Length in Mesoporous Nanocrystalline TiO 2 Photoelectrodes during Water Oxidation. *J. Phys. Chem. Lett.*, 1(6):967–972, 2010.

[43] Cary L. Pint, Kuniharu Takei, Rehan Kapadia, Maxwell Zheng, Alexandra C. Ford, Junjun Zhang, Arash Jamshidi, Rizia Bardhan, Jeffrey J. Urban, Ming Wu, Joel W. Ager, Michael M. Oye, and Ali Javey. Rationally Designed, Three-Dimensional Carbon Nanotube Back-Contacts for Efficient Solar Devices. *Adv. Energy Mater.*, 1(6):1040–1045, 2011.

[44] John T. Yates. Photochemistry on TiO2: Mechanisms behind the surface chemistry. *Surf. Sci.*, 603(10-12):1605–1612, 2009.

[45] Zhen Zhang and John T. Yates. Direct observation of surface-mediated electron-hole pair recombination in TiO2(110). *J. Phys. Chem. C*, 114(7):3098–3101, 2010.

[46] Rizia Bardhan, Shaunak Mukherjee, Nikolay A. Mirin, Stephen D. Levit, Peter Nordlander, and Naomi J. Halas. Nanosphere-in-a-Nanoshell: A Simple Nanomatryushka. *J. Phys. Chem. C*, 114(16):7378–7383, 2010.

[47] Jian Feng Li, Xiang Dong Tian, Song Bo Li, Jason R. Anema, Zhi Lin Yang, Yong Ding, Yuan Fei Wu, Yong Ming Zeng, Qi Zhen Chen, Bin Ren, Zhong Lin Wang, and Zhong Qun Tian. Surface analysis using shell-isolated nanoparticle-enhanced Raman spectroscopy. *Nat. Protoc.*, 8(1):52–65, 2013.

Chapter 3

PLASMON ENHANCED P3HT:PCBM ORGANIC PHOTOVOLTAICS

3.1 Summary

In this chapter, we investigate plasmonic enhancement in poly(3-hexylthiophene):phenyl-C_{61}-butyric acid methyl ester organic P3HT:PCBM organic photovoltaics (OPVs) by integrating shape- and size-controlled bimetallic gold core silver shell nanocrystals (Au-Ag NCs) into the PEDOT:PSS hole transport layer. We observed the best performing Au-Ag NC incorporated OPVs improved the power conversion efficiency by 11% via broadband increase in photocurrent throughout the visible spectrum. Our experimental and computational results suggest that the observed photocurrent enhancement in plasmonic OPVs originates from both enhanced absorption, and improved exciton dissociation and charge collection. This is particularly achieved by placing metal nanocrystals near the interface of the active layer and hole transport layer. The impedance spectroscopy results also suggest that Au-Ag NCs reduce recombination and also increase the internal exciton to carrier efficiency by driving the dissociation of bound charge transfer states to free carriers.

3.2 Introduction

Thin film organic photovoltaics (OPVs) have emerged as a promising alternative to inorganic PVs due to inexpensive fabrication and processing techniques. Whereas a few low band gap polymers with competitive efficiencies are viable competitors in the solar market,[1, 2, 3] the power conversion efficiencies (PCE) of OPVs remain low relative to market-leading inorganic PVs such as Si, CdTe, or $CuInGaSe_2$.[4] A number of factors impact the performance of the OPVs including photon absorption, carrier generation, and carrier collection. The contribution from each of these factors can be understood from the

external quantum efficiency (EQE) expression, which is the wavelength dependent metric for photon to charge carrier efficiency. The expression for EQE is given by: EQE(λ) = η_{abs} $\times$ η_{gen} $\times$ η_{coll} where η_{abs} is the ratio of absorbed light to incident light, η_{gen} is the ratio of photoexcited excitons that are converted to free carriers, and η_{coll} is the carrier collection efficiency at the electrodes.[5, 6, 7] In the archetypal OPV, charge separation is facilitated by bulk heterojunction (BHJ) active layers where the high interfacial area between the continuous veins of electron donor polymers and electron acceptor molecules provides the driving force necessary for the generation of free carriers via the separation of charge transfer excitons.[8, 7] High efficiencies in OPVs are ultimately limited by charge transport and recombination (η_{coll}), however locally improving the light absorption (η_{abs}) and charge generation rate near the collection interface has the potential to improve PCE. Recent approaches to increasing PCE in OPVs have emphasized improving η_{gen} via the modification of the BHJ architecture,[9, 10, 11] as well as to enhance η_{abs} by designing organic-inorganic hybrid devices,[12] tandem junctions,[9, 13] and incorporating metal nanocrystals that support surface plasmons.[14, 15, 7] Augmentation of light harvesting in OPVs has been achieved by embedding colloidal metal nanocrystals in the active layer[16, 17, 18, 19] and the poly(3,4-ethylenedioxythiophene) polystyrene sulfonate (PEDOT:PSS) hole transport layer.[20, 21, 22, 23, 7] While metal nanocrystal enhanced OPVs have attracted significant interest and resulted in 5-50 % increase in photocurrents,[23, 24, 25, 26] the precise origin of plasmonic enhancement in OPVs has remained elusive, and has been primarily correlated to improved absorption.

In this work we demonstrate that BHJ OPVs integrated with gold core-silver shell nanocrystals (Au-Ag NCs) show both increased absorption via light scattering and enhanced local electromagnetic fields, as well as electric field assisted exciton dissociation in the OPVs. Au-Ag NCs enhanced OPVs show an 11% increase in efficiency relative to the reference devices from 2.15% to 2.39% on average. Our experimental and theoretical analyses support that the observed enhancements in photocurrent are collectively driven

by increases in η_{abs}, η_{gen}, and η_{coll}. The contribution from η_{gen}, and η_{coll} can be understood from the origin of Frenkel-type excitons in conjugated polymers. Photoexcitation of poly(3-hexylthiophene) (P3HT) gives rise to Frenkel excitons where the Coulomb binding energy restricts the electron-hole separation to ~2 nm with binding energy in the range of 0.4-1.0 eV which is above the threshold for dissociation.[27, 28] The unique geometry driven optical properties of Au-Ag NCs give rise to strong electric fields in the vicinity of the nanocrystals which extend to tens of nanometers. These strong electric fields improve the absorption (η_{abs}) near the P3HT:PCBM/PEDOT:PSS interface, as well as enhance the conversion of bound Frenkel-type charge transfer excitons to free carriers subsequently improving η_{gen} and the overall photocurrent. Our proposed mechanism is supported by recent studies which describe that non-equilibrium hot excitons at the donor/acceptor interface in BHJ architectures contribute strongly in carrier generation.[29, 30] This motivates our work where we demonstrate plasmonic enhancement in BHJ OPVs is catalyzed by interplay between charge transfer excitons and surface plasmons, and is not simply a result of improved light absorption. We have combined optical and optoelectronic characterization to study and understand the performance Au-Ag NC incorporated OPVs. Experimental observations are supplemented with a 3D finite-difference time-domain (FDTD) model to support our hypothesis.

3.3 Results and Discussion

OPVs were fabricated by adapting a standard procedure from the literature;[15] details are available in Section 3.5. We note that our relative low efficiencies are primarily a result of using low molecular weight P3HT (Mn = 15,000-45,000, Sigma 698989), and our efficiencies are typical for this molecular weight.[31] Au-Ag NCs were embedded in the 70 nm thick PEDOT:PSS hole transport layer of the OPVs. Embedding the nanocrystals in the hole transport layer minimizes any change in the morphology of the active layer and prevents introducing defects that can be detrimental to OPV performance.[32] The 140 nm

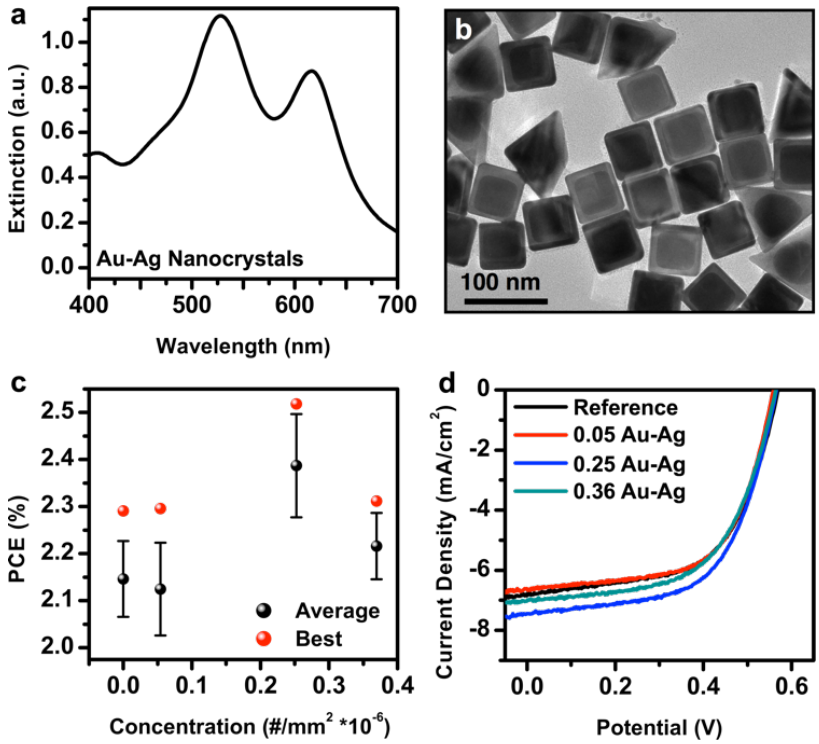

Figure 3.1: (a) Representative extinction spectrum of Au-Ag NCs in aqueous media. (b) Representative TEM image of Au-Ag nanocrystals showing both nanocubes and nanopyramids. (c) Power conversion efficiency as a function of Au-Ag NC concentration. The error bars represent 16 devices. (d) Current density vs. potential (J-V) curves for OPVs at different Au-Ag NC particle densities where the numbers refer to no. of particles/μm^2.

thick active layer is composed of poly(3-hexylthiophene):phenyl-C61-butyric acid methyl ester (P3HT:PCBM). The plasmon resonance of Au-Ag NCs spans the visible spectrum (Figure 3.1a), which is ideal for OPVs where a broadband response results in increased light capture.

A representative TEM image of Au-Ag NCs features two distinct geometries (Figure 3.1b), bimetallic nanocubes and nanopyramids. The origin of these shapes lies in the synthesis process and is described in detail in Chapter 2. The plasmon mode at 530 nm is attributed to the dipole mode of the nanocubes, and at 630 nm is contributed by the dipolar resonance of the nanopyramids.[33, 34] The sharp corners and edges of Au-Ag NCs generate strong local fields that extend up to 30 nm nanometers from the surface of the Au-Ag NCs (Figure 3.2). These intense fields are a result of charge accumulation at the corners

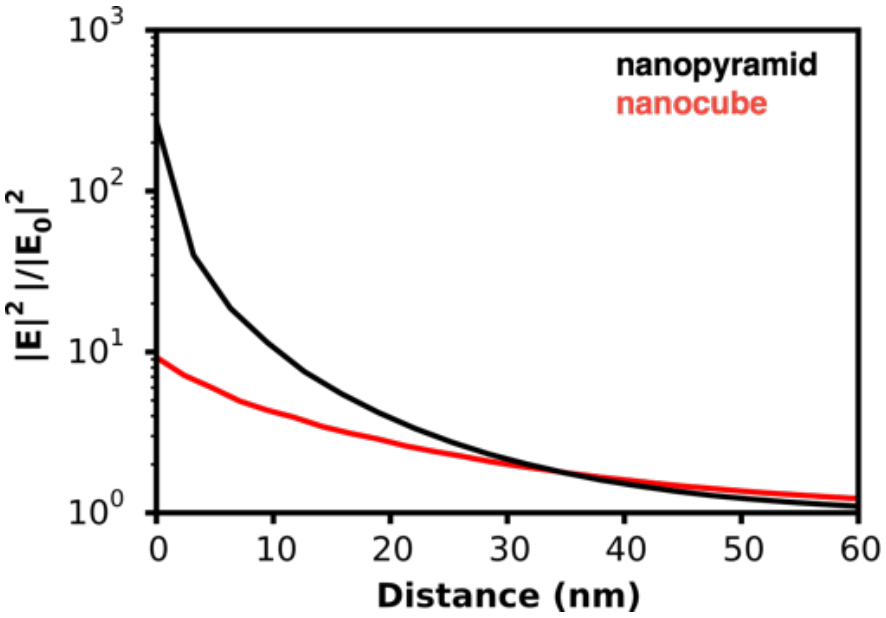

Figure 3.2: Simulated intensity of radiative field as a function of distance from the particle in a water background averaged over the x, y, and z planes bisecting the respective particles.

and edges of Au-Ag NC described as the lightning-rod effect, which is frequently observed in non-spherical nanostructures.[35, 36, 37]

The PCE of OPVs is enhanced by 11% upon integrating Au-Ag NCs in the PEDOT:PSS layer (Figure 3.1c). The concentration of Au-Ag NCs was varied in the PEDOT:PSS solution before spin coating to determine the effect of the nanocrystal density on PCE enhancement. The particle density was confirmed by examining the PEDOT:PSS layer in SEM and counting the number of Au-Ag NCs per area (Figure 3.4). The effect of Au-Ag NC concentration on the fill factor (FF), short circuit current density (J_{sc}) and open circuit voltage (V_{oc}) are provided in Figure 3.3. The improvements in PCE were attributed to increased current density in the presence of the Au-Ag NCs, which peaks at an area density of 0.25 $\times$ 10^6 particles/mm^2, as shown in the J-V curves in Figure 3.1d.

The trend observed in PCE closely resembles the trend in J_{sc} which likely results from two primary effects: *(i)* increased overall light harvesting in the active layer (η_{abs}), and *(ii)* increased exciton separation to collected carrier efficiency (η_{gen} + η_{coll}). At high concentrations of Au-Ag NCs the PCE is reduced due to the formation of nanoparticle aggregates

Table 3.1: Average P3HT:PCBM device characterization parameters

Concentration (#μm^2)	FF	V_{oc} (V)	J_{sc} (mA/cm^2)	PCE (%)	Champion PCE (%)
0	0.59	0.57	7.69	2.58	2.85
0.05	0.60	0.56	7.62	2.55	2.82
0.25	0.59	0.56	8.47	2.80	3.10
0.37	0.57	0.56	8.33	2.66	2.86

that increase recombination losses. All device performance parameters are provided in Table 3.1.

To understand the origin of the photocurrent enhancement, we compared the EQE of a reference OPV (no nanocrystals) to that with optimum Au-Ag NCs concentration (Figure 3.5a). The average EQE enhancement of 10% agrees with the 11% enhancement found in PCE. The normalized EQE in Figure 3.5b suggests that the photocurrent enhancement in the presence of Au-Ag NCs is broadband throughout the visible region and does not show any spectral dependence overlapping with the Au-Ag NC plasmon resonance (Figure 3.1a).

The broadband enhancement is attributed to plasmon red-shift of Au-Ag NCs spanning the visible and near-infrared and spectral broadening in the presence of PEDOT:PSS.We measured the extinction of the plasmon-enhanced devices relative to the reference OPVs (Figure 3.5c) and observed that the two spectra overlapped to within 0.1% when integrated over the visible spectrum. This indicates that absorption contribution from the nanoparticles when averaged over the entire cross section of the active layer is minimal; however, we find that in the presence of the Au-Ag NCs, the electric field preferentially increases near the PEDOT:PSS interface where charge collection occurs. Simulations (Figure 3.8) clearly demonstrate that plasmonic enhancement of ~35% is achieved localized at the P3HT:PCBM/PEDOT:PSS interface averaged over the bottom 10 nm volume of the active layer.

The lack of enhancement in the experiments (Figure 3.5c) is because experimental extinction is bulk measurements accounting for the entire OPV. The spectrophotometer is not sensitive enough to only focus at the P3HT:PCBM/PEDOT:PSS interface and measure im-

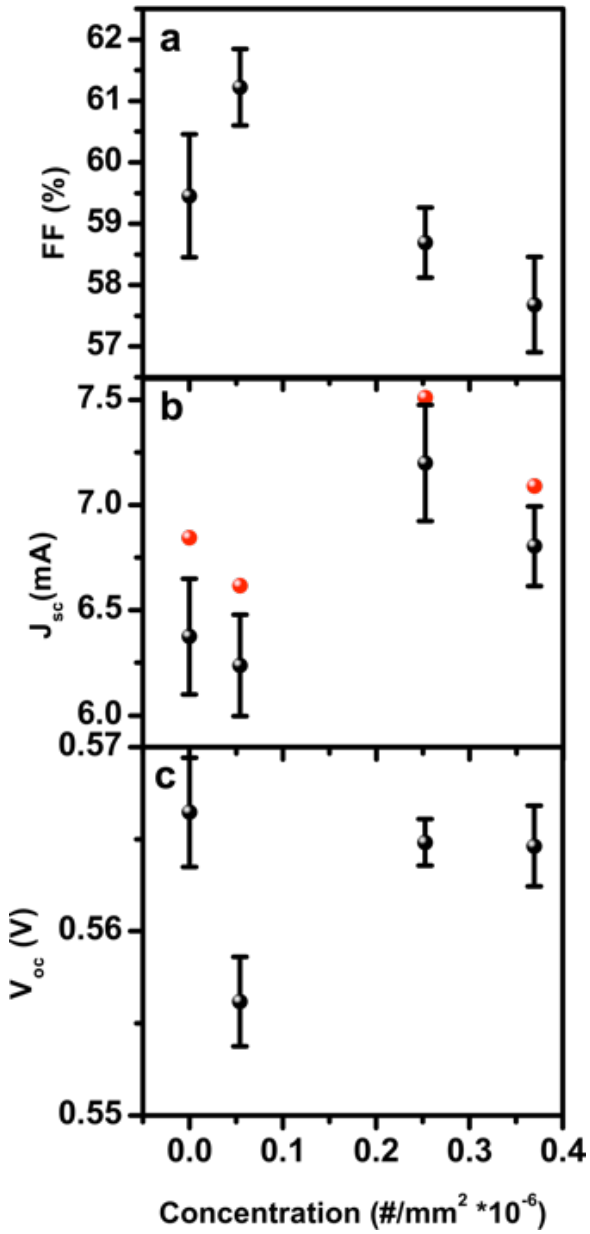

Figure 3.3: OPV characterization parameters (a) fill factor, (b) short circuit current density, and (c) open circuit voltage as a function of Au-Ag concentration.

proved extinction at the interface. However, we note that the strong radiative properties of the Au-Ag NCs, both attributed to the size and the presence of the Ag layer, are the driving force for the observed enhancement in EQE and J-V curves.[34, 37] To demonstrate this, we also incorporated Au nanocubes (Figure 3.6a) without any Ag layer into devices. Au nanocubes have narrow spectral resonance relative to Au-Ag NCs (Figure 3.6), and are pri-

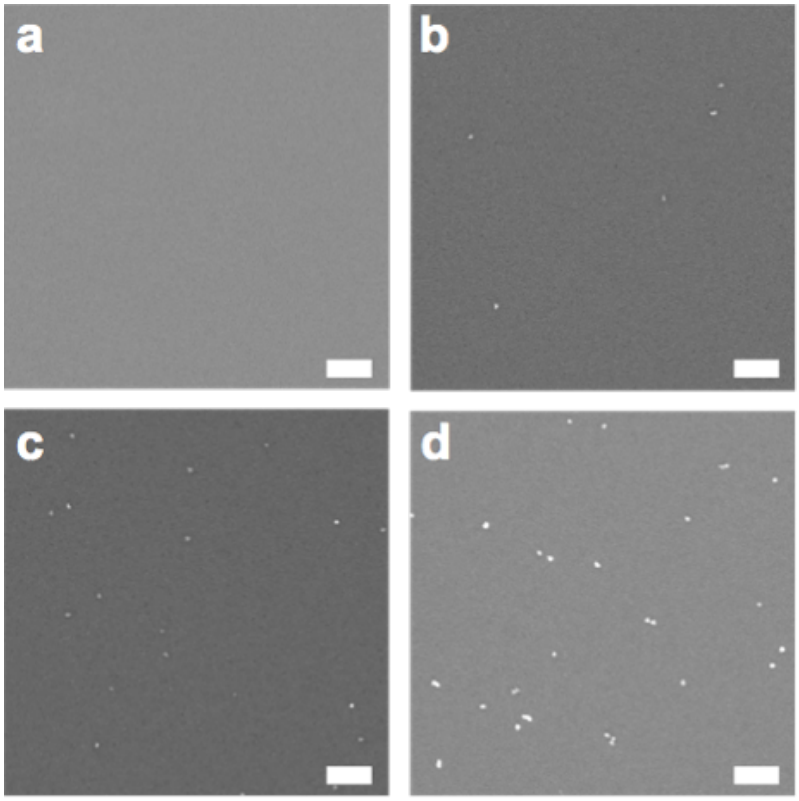

Figure 3.4: Scanning electron micrographs of Au-Ag doped PEDOT:PSS on ITO for (a) reference sample, (b) 0.05% doping, (c) 0.25% doping and (d) 0.40% doping. Scale bar represents 1μm.

marily absorbing rather than scattering (Figure 3.6c). Due to their low scattering properties, we observed a decrease in EQE relative to the reference (Figure 3.6d).

To further understand the origin of plasmonic enhancement, FDTD simulations were performed to measure the spatially-dependent electric field enhancement in the OPV (Figure 3.8). In order to gain an understanding of the plasmonic radiative field strength of the Au-Ag NCs at different locations in the OPV active layer, E-field monitors were placed at the top, middle and bottom of the P3HT:PCBM layer. These simulations demonstrate three different effects across the OPV. First the simulations show Au-Ag NCs have significant forward scattering into the active layer, with spatially dependent average electric field intensity up to 18$\times$ the incident field over the wavelength range of 400 - 700nm. A ~35% plasmonic enhancement is achieved in the OPVs localized within 10 nm of the

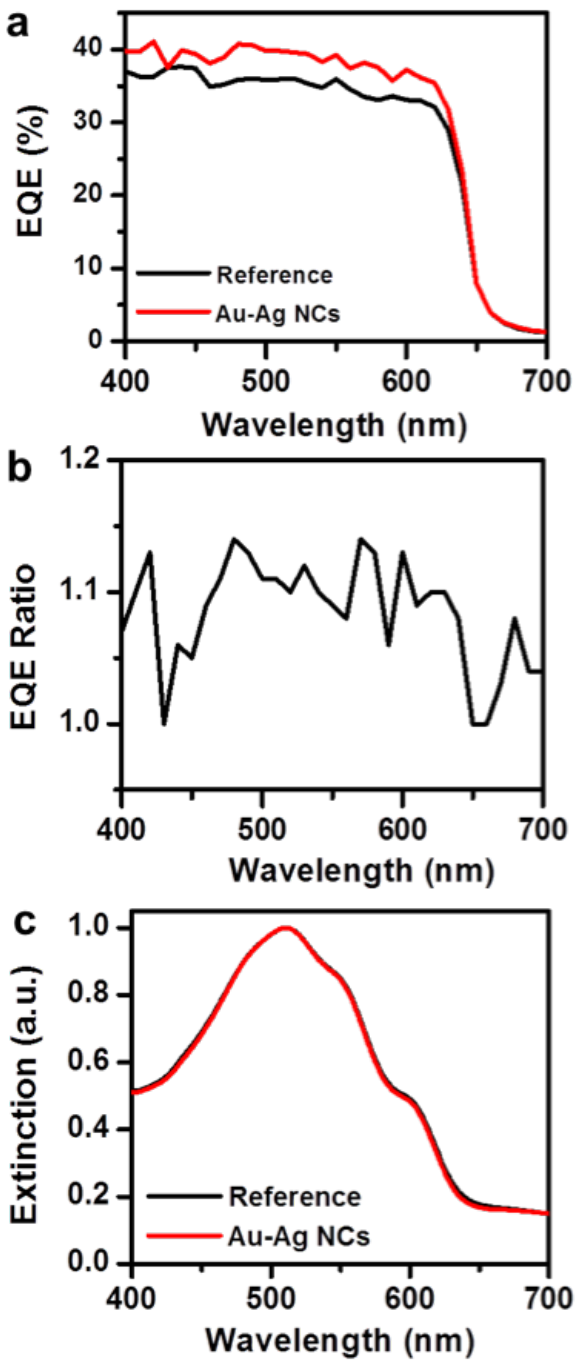

Figure 3.5: (a) EQE of both control and Au-Ag-enhanced OPVs. (b) Ratio of the EQE of the Au-Ag-enhanced OPV to the control OPV. (c) Experimentally observed extinction spectra for control and Au Ag-enhanced OPVs.

P3HT:PCBM/PEDOT:PSS interface (Figure 3.8b,c bottom) which is within the electric field decay length of the Au-Ag NCs. The near field decay length of Au-Ag NCs is within

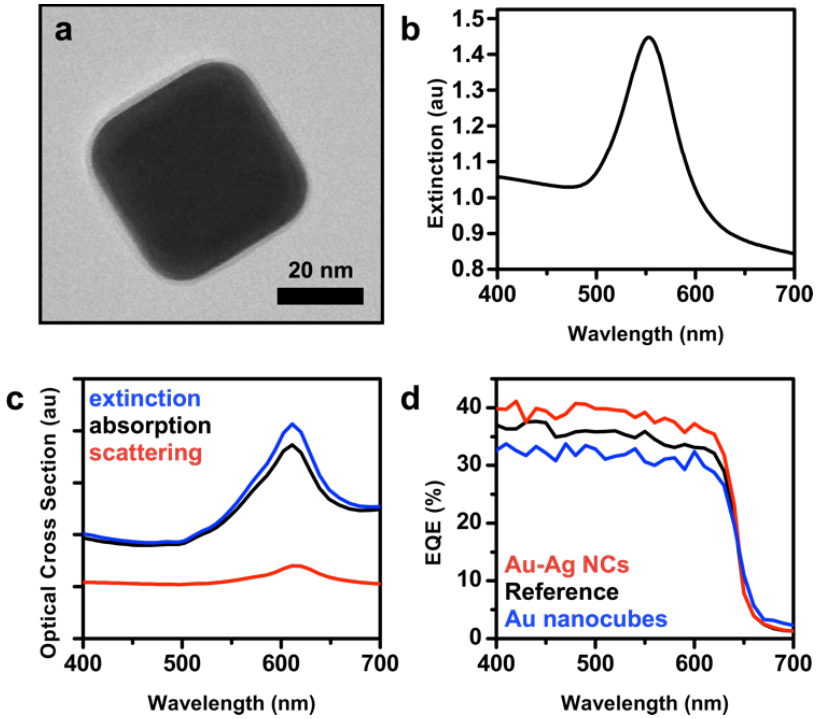

Figure 3.6: (a) Transmission electron micrograph of Au nanocube which were integrated in the OPVs. b) Experimental extinction of Au nanocube in aqueous media. (c) Calculated absorption, scattering, and extinction of Au nanocubes embedded in PEDOT:PSS layer. (d) External quantum efficiency of Au nanocube enhanced OPVs relative to reference and Au-Ag NCs enhanced OPVs.

30 nm from their surface (Figure 3.2). Second a 13% increase in absorption is observed at the top of the OPV (140 nm from the PEDOT:PSS interface) closer to the Al top electrode which we attribute to back scattered light from the Al electrode increasing the light harvested by the OPVs. And third, in the middle of the OPVs (70 nm from the PEDOT:PSS interface) there is a ~37% decrease in absorbance in the presence of the nanocrystals. This decrease is because in the middle of the OPVs there is no effect from back-scattered light from the Al top electrode and the electric fields from the Au-Ag NCs have already decayed. Therefore light re-radiated from the nanocrystals (or Al electrode) does not reach the middle of the OPV and instead we see parasitic effect that reduces the overall absorbance in the presence of the nanocrystals. Collectively the three effects correlate well with the experimental enhancement of 11% observed in the PCE and J-V curves (Figure 3.1c,d) and EQE (Figure 3.5a) from the plasmonic devices. But we anticipate the increase in absorption at the interface of the active layer and hole transport layer likely contributes to the increased photocurrent, as the carrier generation profile is strongly skewed towards the illumination side of the device. It has been proposed by Fung et.al.[14] that increased roughness at the PEDOT:PSS/P3HT:PCBM interface due to incorporation of nanoparticles could increase the interfacial area for charge separation, thereby increasing PCE. Atomic force microscopy (AFM) scans (Figure 3.7) indicate that the average roughness at the interface is <1 nm in both reference and nanocrystal incorporated samples, and is unlikely contributes to performance enhancement.

To further understand plasmonic enhancement in OPVs by Au-Ag NCs we performed electrochemical impedance spectroscopy (EIS). Nyquist plots of reference OPVs and best-performing Au-Ag NC embedded OPVs at particle concentration of 0.25 nanocrystals/μm^2 are shown in Figure 3.9a. The Nyquist plots are fit to an equivalent circuit model (Figure 3.9b) which has four components: series resistance (R_s), recombination resistance (R_r), contact capacitance (C_c), and Gerischer impedance (G). G represents diffusion of separated charges. The high frequency region shown in the Nyquist plot is attributed to R_r and

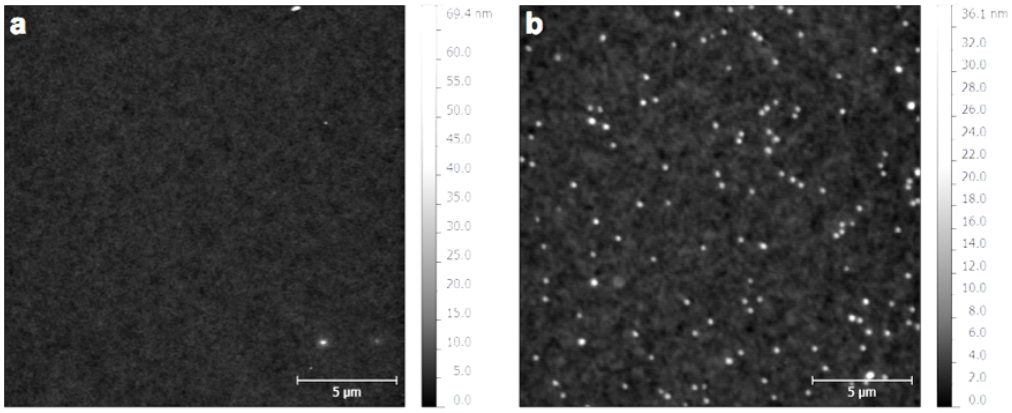

Figure 3.7: Atomic force micrographs of (a) the control and (b) the optimum concentration Au-Ag doping in PEDOT:PSS.

C_c owing to charge buildup between P3HT:PCBM active layer and its adjacent contacts including the PEDOT:PSS hole transport layer, and the LiF electron transport layer. According to circuit model fits, Au-Ag NC integration did not significantly alter the R_s relative to the reference OPVs but lowered R_r (24% decrease), C_c (25% decrease), and Gerischer impedance, G, (82% decrease).

The fit parameters are included in Table 3.2. These results indicate that bimetallic nanocrystals decrease carrier recombination and promote diffusion across the PEDOT:PSS layer improving the charge generation and collection efficiency ($\eta_{gen} + \eta_{coll}$). Bode phase plots were used to examine the behavior of charged species within the reference and plasmon-enhanced OPVs at different particle concentrations of Au-Ag NCs (Figure 3.9c). The Bode phase peak frequency decreases as Au-Ag NC concentration increases. The phase represents the shift of the input phase; the frequency at maximum phase shift these OPVs is proportional to the inverse of the electron lifetime. Equation 3.1 shows the relationship between frequency at peak phase shift and carrier lifetime.[38]

$$\tau_{eff} = \frac{1}{2\pi f} \tag{3.1}$$

The effective lifetime of carriers, τ_{eff}, decreases from ~4.0 μs to ~2.5 μs with the

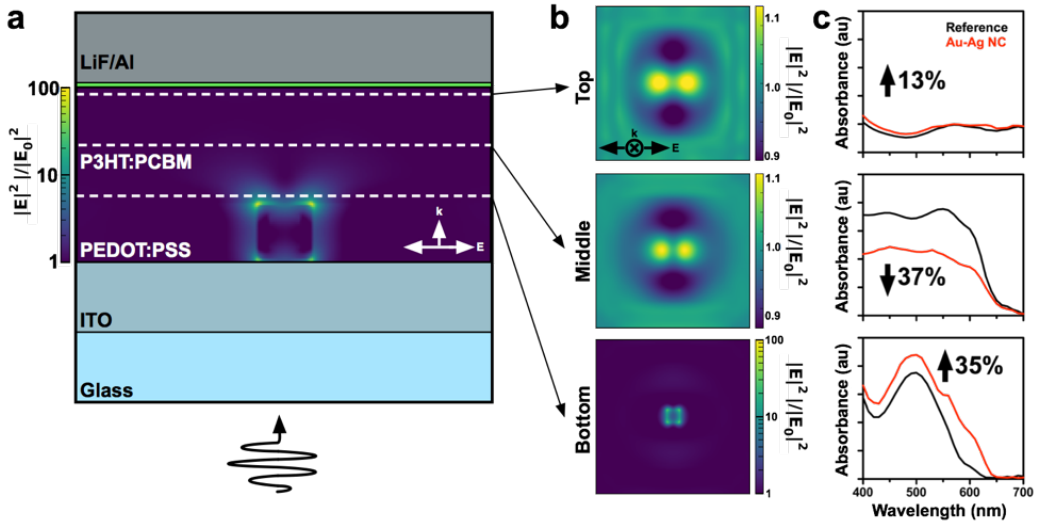

Figure 3.8: (a) Cross section of the electromagnetic field enhancement in the hole transport layer (PEDOT:PSS) and active layer (P3HT:PCBM) with an embedded Au-Ag nanocube. (b) Cross sections perpendicular to the k-vector of the top, middle, and bottom sections of the active layer. (c) Calculated absorbance spectra corresponding to the cross-sections shown in (b) showing a 13% increase in absorbance at the top of the OPV, a 35% increase near the PEDOT:PSS/P3HT:PCBM interface, and a 37% decrease in absorbance in middle of the OPVs.

Table 3.2: P3HT:PCBM OPV circuit model fits

	R_s (Ω)	R_{rec} (Ω)	C_c (nF)	G (mMho)
Control	63	144	41	3.9
Optimal Au-Ag	65	120	30	0.7

addition of Au-Ag NCs (Figure 3.9d). We attribute the decrease in τ_{eff} to two distinct factors resulting the presence of the Au-Ag NCs and subsequent enhanced electric field: *i)* increased carrier generation and *ii)* decreased carrier diffusion length. As is shown in Figure 3.8, the presence of Au-Ag NCs causes regions of intense electric field, which in turn creates carrier concentrations higher than in reference cells, leading to increased probability for carrier collision, a phenomenon that has been previously demonstrated in the literature.[39] Additionally, because the electric field is distorted such that charge generation is concentrated near the P3HT:PCBM/PEDOT:PSS interface with the presence of Au-Ag NCs (Figure 3.8), the required diffusion length to carrier collection is shortened, thus the free carrier lifetime decreases. This is in agreement with the decrease in Gerischer impedance in the presence of the nanocrystals, which is representative of diffusion of separated charges across the hole-transport layer.

Based on our experimental and simulated results, our hypothesis is the strong electric fields generated by Au-Ag NCs collectively improve absorption efficiency (η_{abs}), carrier generation efficiency (η_{gen}), and charge collection efficiency (η_{coll}) in our system. Strong electric fields in conjugated polymers have been shown to be capable of providing sufficient driving force for exciton dissociation,[40, 41, 42] yet this concept has not been emphasized in plasmonic OPV systems. To further understand the origin of the enhanced performance of the Au-Ag NC incorporated devices, we analyzed the photocurrent of the reference and best plasmonic device (Figure 3.10) as a function of the effective potential (V_0).[23] Figure 3.10 shows a plot of the photocurrent density (J_{ph} = J_{dark} - V_{eff}) at AM 1.5 illumination versus the effective voltage (V_{eff} = V_0 - V_a), where V_0 is the potential where J_{light} equals zero, and V_a is the applied potential (Figure 3.10a). This plot was used to calculate the maximum exciton generation rate, J_{ph}, which is given by G_{max} $J_{sat} = qG_{max}L$, where J_{sat} is the saturated or maximum J_{ph} that is obtained at higher potential, q is the electronic charge, and L is the active layer thickness. J_{sat} for our reference and plasmonic devices was 72 A/m^2 and 77 A/m^2, respectively, and resulted in G_{max} values of 3.21 $\times$ 10^{27} m^{-3}s^{-1} and 3.43

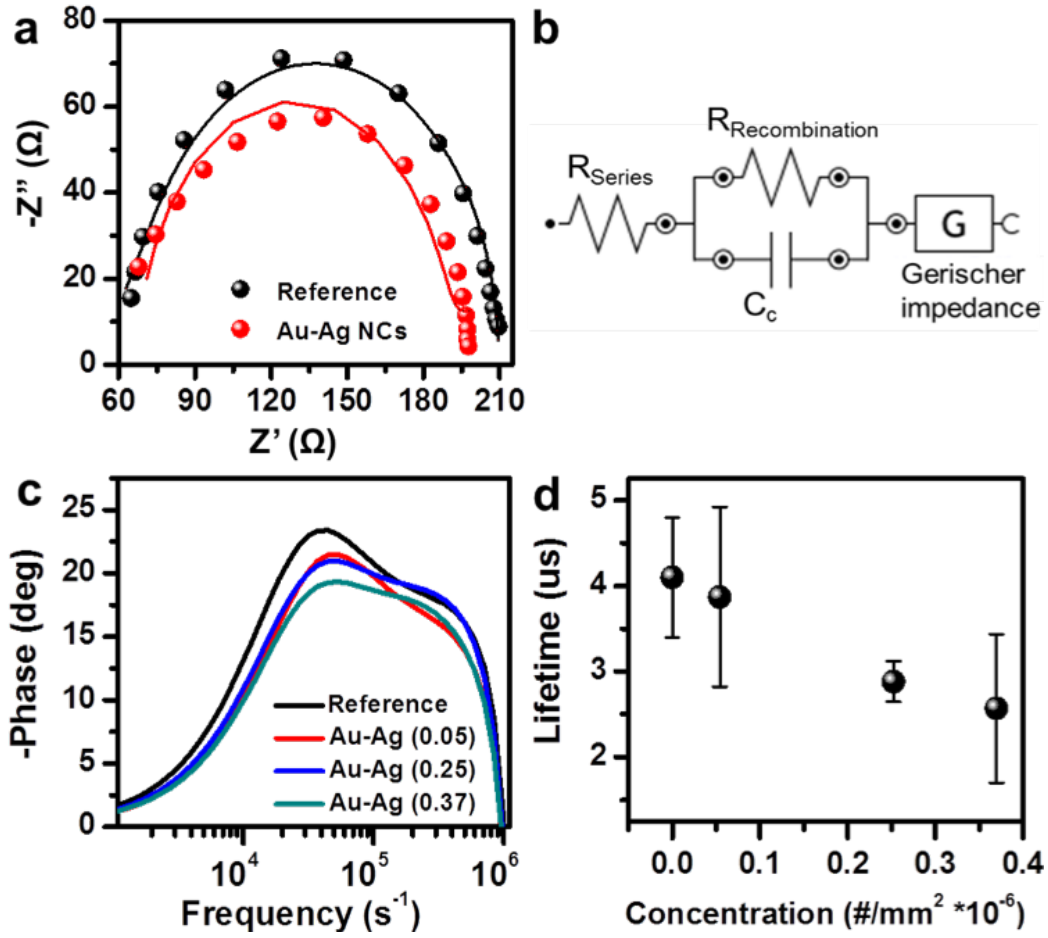

Figure 3.9: Electrochemical impedance spectroscopy of the OPVs. (a) Best performing Au-Ag NCs enhanced and reference Nyquist plots fitted to a circuit model shown in (b). (c) Bode phase plots of OPVs with increasing Au-Ag NCs particle concentration. The numbers in bracket correspond to no. of particles/μm. (d) Carrier lifetimes of reference and Au-Ag NC enhanced OPVs calculated from the frequency at peak phase shift in the Bode plots in (c). Error bars represent n = 3 measurements per sample.

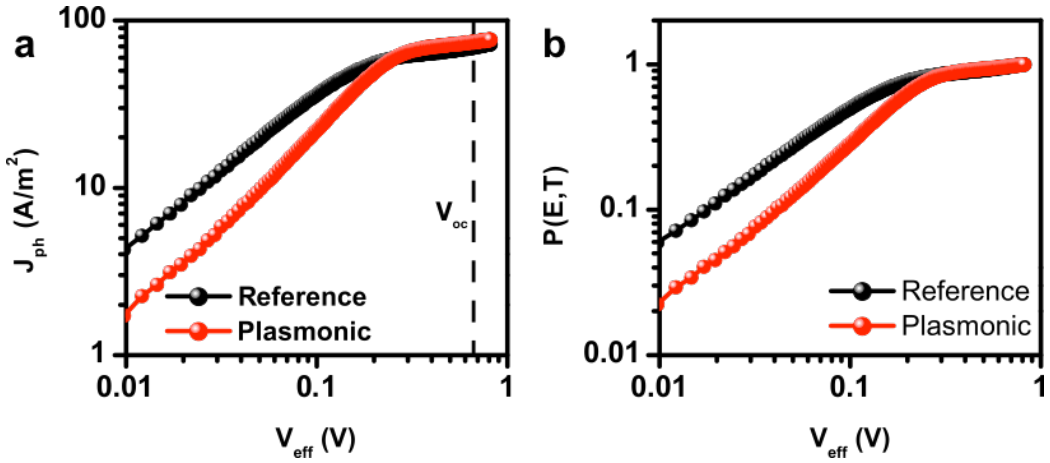

Figure 3.10: (a) Photocurrent density versus effective potential for reference and best plasmonic device. (b) Probability for exciton dissociation versus effective potential for reference and best plasmonic device.

$\times$ 10^{27} m^{-3}s^{-1}, respectively. Since q and L are constant among both devices, this 6.4% improvement in G_{max} from reference to plasmonic OPVs indicates a direct enhancement in exciton generation in the active layer. We also calculated the exciton dissociation probability, $P(E,T)$ which simply provides a measure of effective charge separation (Figure 3.10b). $P(E,T)$ was calculated at the short-circuit condition ($V_a = 0$), where $J_{ph} = qG_{max}P(E,T)L$. We calculated that J_{ph} at $V_a = 0$ was 67.7 mA/cm^2 and 74.5 mA/cm^2 resulting in $P(E,T)$ of 94% and 97%, for the reference and plasmonic devices, respectively indicating that the presence of the nanocrystals increased the dissociation of excitons into free carriers. These $P(E,T)$ values correlate well with those observed in literature and supports our initial hypothesis that the observed enhancements in photocurrent are collectively driven by increases in η_{abs}, η_{gen}, and η_{coll}.[23, 24]

The presence of Au-Ag NCs in our BHJ OPVs not only improves the absorption (η_{abs}) near the P3HT:PCBM/PEDOT:PSS interface but also promotes dissociation of Frenkel-type charge transfer excitons in P3HT. Upon photoexcitation of the P3HT:PCBM active layer, a tightly bound exciton with a diffusion length of 10 nm is formed.[6] In the reference OPVs, free carriers are formed when the exciton diffuses to the donor/acceptor interface and sufficient energy is available for charge separation. In the Au-Ag NC in-

corporated OPVs, two effects simultaneously impact the performance: *(i)* strong radiative enhancement contributed by the intense near-fields and light scattering from the Au-Ag NCs localized within 10 nm of the interface of the active layer and hole-transport layer, as shown in our simulated results (Figure 3.8). This 35% increase in absorbance increases absorption efficiency (η_{abs}) concentrated near the interface of the active layer and hole transport layer, *(ii)* Enhanced exciton dissociation near a charge collection interface - the strong electric fields of Au-Ag NCs in the vicinity of the nanocrystals increase the probability for the dissociation of charge transfer excitons in P3HT, improving the photoexcited exciton to carrier generation efficiency (η_{gen}). These separated electrons and holes are in the proximity of the hole conductor, PEDOT:PSS, which facilitates efficient charge collection efficiency (η_{coll}).

3.4 Conclusions

In summary, we have fabricated plasmon enhanced P3HT:PCBM OPVs by embedding bimetallic Au core Ag shell nanocrystals in the PEDOT:PSS hole transport layer. Power conversion efficiency improved by 11% relative to the reference at the optimized concentration of Au-Ag nanocrystals. Our experimental and simulated results suggest that Au-Ag NCs result in broadband enhancement in the visible and near-infrared spectrum due to improved absorption and increased charge separation, where strong electric fields of Au-Ag NCs assist in separating bound Frenkel-type excitons. EIS measurements support our hypothesis that plasmonic enhancement in our system also results from increased internal exciton to carrier efficiency and increased charge collection, in addition to increased photon to carrier efficiency. We envision that by carefully controlling the interplay between surface plasmons and charge transfer excitons, metal nanostructures can be designed to have dual roles - as light harvesters which will improve η_{abs}, and as driving force for exciton dissociation and carrier collection which will improve η_{gen} and η_{coll}. Energy upconversion via plasmon-exciton coupling may play a role in increasing absorption of low

energy light in conjugated polymers, and could be potentially explored in future. We anticipate that this work will provide design rules for the fabrication of plasmonic OPVs with improved efficiencies, reduced recombination, and better carrier collection efficiency across the charge transport layers. These enhancements controlled by electric fields of shape- and size-controlled plasmonic nanostructures will ultimately enable thin-film, flexible devices viable for large-scale manufacturing and integration

3.5 Methods

All chemicals were purchased from Sigma-Aldrich unless noted otherwise; all water was nanopure from a Milli-Q Direct-Q 3UV system. All work conducted under inert atmosphere was conducted in a nitrogen environment in an M-Braun LabStar glovebox (<0.5 ppm O_2). Thermal evaporation was conducted on an Angstrom Amod system.

NC Synthesis. Bimetallic NCs were synthesized by the procedure reported in Section 2.5 and consisted of three steps: seed growth, Au nanocube growth, and Ag capping layer growth.

Seed Solution. A solution of 2.75 mL water, 7.5 mL 100 mM cetyltrimethylammonium bromide (CTAB), and 250 μL 10 mM $HAuCl_4$ were added to a 10 mL glass vial, mixed by inversion, and placed in a 35 °C water bath for temperature equilibration. After 10 min, 600 μL of ice cold, freshly prepared 10 mM $NaBH_4$ solution was injected with vigorous stirring, followed by 1 min of stirring before being returned to the 35 °C water bath for 1 h undisturbed.

Au Nanocube Growth. The seed solution was removed from the water bath and reduced 10× with water. Next, in a 50 mL vial, 6.4 mL 100 mM CTAB, 800 μL 10 mM $HAuCl_4$, 3.8 mL 100 mM ascorbic acid, and 20 μL diluted seed solution were added and mixed by inversion. The vial was then placed in a 35 °C water bath and allowed to sit undisturbed for 5 h.

Ag Capping Layer Growth. Au nanocubes (7.5 mL) were centrifuged at 1100 rcf for 15

min, the supernatant removed and the pellet redispersed in 3.75 mL of 20 mM hexadecyl trimethylammonium chloride (CTAC) and allowed to sit for 15 min. The centrifugation and redispersal step was repeated two additional times; however, on the final redispersal, the pellet was combined with 500 μL water, rather than a CTAC solution. Next, 20 mL 20 mM CTAC, 800 μL concentrated Au nanocubes from the previous step, and 200 μL 10 mM KBr were combined in a 50 mL vial and placed in a 65 °C water bath. After 10 min, the vial was removed from the water bath and mixed by inversion with 220 μL of 10 mM $AgNO_3$ and 600 μL 100 mM ascorbic acid. Finally, the vial was placed in a 65 °C water bath for 2 h. The colloid was stable for up to 60 days in the dark at 2 °C.

Device Fabrication. ITO glass (150 nm, <10 ÅRMS roughness) was purchased from Thin Film Devices Inc. Phenyl-C_{61}-butyric acid (PCBM) was purchased from Rieke Materials, and P3HT was from Sigma-Aldrich (698989). OPV fabrication was adapted from a procedure in the literature.[43] One inch ITO glass squares were cleaned with acetone and isopropanol and dried with nitrogen, followed by air plasma treatment for 10 min to remove any organic residue. Next, a solution of PEDOT:PSS was filtered through a 0.45 μm PVDF filter and concentrated Au-Ag NCs were spin coated onto the cleaned substrates at 1500 rpm for 60 seconds and dried at 120 °C for 10 min, then transferred to an inert environment. Under inert atmosphere, 20 mg P3HT and 16 mg PCBM were combined with 720 μL dichlorobenzene and stirred at 125 °C for 30 min, then allowed to be stirred at room temperature overnight. A 100 μL drop of P3HT:PCBM solution was spin cast onto the PEDOT:PSS coated substrates at 500 rpm for 5 s and 2000 rpm for 13 s, followed by immediate transfer to a dichlorobenzene environment until the film transitioned from bright orange to dark red/purple. This solvent annealing step was essential for the formation of the BHJ and dictates the charge separation and charge-transfer efficiency. The substrate was kept in an inert environment and transferred to a vacuum evaporation chamber where 1 nm LiF and 100 nm Al were deposited in 8 mm diameter circles via shadow masks.

Material Characterization. All optical spectroscopic measurements were carried out with

a Varian Cary 5000 ultravioletvisible spectrophotometer. SEM and TEM were conducted using a Zeiss Merlin and FEI Osiris, respectively. A Veeco Dektak 150 profilometer was used for all layer thickness measurements. AFM was performed on a Bruker Dimension Icon AFM.

Photoelectrical Characterization. All current-potential scans were conducted under AM 1.5G 100 mW/cm^2 illumination at a 10 mV/s scan rate using a MetroOhm Autolab potentiostat. EIS was conducted with an amplitude of 10 mV over a frequency range of 10^3 10^6 Hz. Quantum efficiency measurements were conducted on a homemade setup using a Fianum supercontinuum laser, a Thorlabs PM100D power meter, and a Keithley 2600 sourcemeter. To block any additional current via lateral charge transport, shadow masks were used.

Electrodynamic Modeling. All electrodynamic modeling was carried out in Lumerical FDTD Solutions software with a simulation time of 500 fs and a spectral range of 400700 nm. The solar cell stack of ITO/PEDOT:PSS/P3HT:PCBM/Al had thicknesses of 100/70/140/100 nm, respectively. All metal/dielectric interfaces were contained in a 0.7 nm mesh grid. Dielectric parameters for all layers are available in the literature.[44, 45] Figure 3.2 was generated by taking a slice from the center of the nanoparticles in the x, y, and z planes and by averaging the enhancement of field intensity as a function of distance from the edge of the particle. Further simulation details are available in Chapter 4.

3.6 Bibliography

[1] Eva Bundgaard and Frederik C. Krebs. Low band gap polymers for organic photovoltaics. *Sol. Energy Mater. Sol. Cells*, 91(11):954–985, 2007.

[2] Gang Li, Rui Zhu, and Yang Yang. Polymer solar cells. *Nat. Photonics*, 6(3):153–161, 2012.

[3] Huaxing Zhou, Liqiang Yang, and Wei You. Rational Design of High Performance Conjugated Polymers for Organic Solar Cells. *Macromolecules*, 45(2):607–632, 2012.

[4] Nathan S. Lewis. Research opportunities to advance solar energy utilization. *Science*, 351(6271), 2016.

[5] Andre Molitin and Jean-Michel Nunzi. How to model the behaviour of organic photovoltaic cells. *Polym. Int.*, 55:583–600, 2006.

[6] S. Matthew Menke and Russell J. Holmes. Exciton diffusion in organic photovoltaic cells. *Energy Environ. Sci.*, 7(2):499–512, 2014.

[7] Chun-Hsien Chou and Fang-Chung Chen. Plasmonic nanostructures for light trapping in organic photovoltaic devices. *Nanoscale*, 6(15):8444–8458, 2014.

[8] Qiaoqiang Gan, Filbert J. Bartoli, and Zakya H. Kafafi. Plasmonic-enhanced organic photovoltaics: breaking the 10% efficiency barrier. *Adv. Mater.*, 25(17):2385–2396, 2013.

[9] T. Ameri, G. Dennler, C. Lungenschmied, and C. J. Brabec. Organic tandem solar cells: A review. *Energy Environ. Sci.*, 2(4):347–363, 2009.

[10] Weiran Cao and Jiangeng Xue. Recent progress in organic photovoltaics: device architecture and optical design. *Energy Environ. Sci.*, 7(7):2123–2144, 2014.

[11] Paul Heremans, David Cheyns, and Barry P. Rand. Strategies for Increasing the Efficiency of Heterojunction Organic Solar Cells : Material Selection and Device Architecture. *Acc. Chem. Res.*, 42(11):1740–1747, 2009.

[12] Matthew Wright and Ashraf Uddin. Organic-inorganic hybrid solar cells: A comparative review. *Sol. Energy Mater. Sol. Cells*, 107:87–111, 2012.

[13] Tayebeh Ameri, Ning Li, and Christoph J. Brabec. Highly efficient organic tandem solar cells: a follow up review. *Energy Environ. Sci.*, 6(8):2390–2413, 2013.

[14] Dixon D. S. Fung, Linfang Qiao, Wallace C. H. Choy, Chuandao Wang, Wei E. I. Sha, Fengxian Xie, and Sailing He. Optical and electrical properties of efficiency enhanced polymer solar cells with Au nanoparticles in a PEDOTPSS layer. *J. Mater. Chem.*, 21(41):16349, 2011.

[15] Shiva Shahin, Palash Gangopadhyay, and Robert Norwood. Plasmonic-enhanced organic solar cells. *Proc. SPIE*, 8471:84710D, 2012.

[16] Peng Du, Pengtao Jing, Di Li, Yinghui Cao, Zhenyu Liu, and Zaicheng Sun. Plasmonic ag@oxide nanoprisms for enhanced performance of organic solar cells. *Small*, 11(20):2454–2462, 2015.

[17] Abhishek P. Kulkarni, Kevin M. Noone, Keiko Munechika, Samuel R. Guyer, and David S. Ginger. Plasmon-enhanced charge carrier generation in organic photovoltaic films using silver nanoprisms. *Nano Lett.*, 10(4):1501–1505, 2010.

[18] Michael Salvador, Bradley A. Macleod, Angela Hess, Abhishek P. Kulkarni, Keiko Munechika, Jennifer I. L. Chen, David S. Ginger, and Salvador E. T. Al. Electron Accumulation on Metal Nanoparticles in Plasmon-Enhanced Organic Solar Cells. *ACS Nano*, 6(11):10024–10032, 2012.

[19] Robert C. Wadams, Chun-wan Yen, Dennis P. Butcher, Hilmar Koerner, Michael F. Durstock, Laura Fabris, and Christopher E. Tabor. Gold nanorod enhanced organic photovoltaics: The importance of morphology effects. *Org. Electron.*, 15(7):1448–1457, 2014.

[20] Se Woong Baek, Jonghyeon Noh, Chun Ho Lee, BongSoo Kim, Min Kyo Seo, and Jung Yong Lee. Plasmonic Forward Scattering Effect in Organic Solar Cells: A Powerful Optical Engineering Method. *Sci. Rep.*, 3:1–7, 2013.

[21] Se Woong Baek, Garam Park, Jonghyeon Noh, Changsoon Cho, Chun Ho Lee, Min Kyo Seo, Hyunjoon Song, and Jung Yong Lee. Au@Ag core-shell nanocubes for efficient plasmonic light scattering effect in low bandgap organic solar cells. *ACS Nano*, 8(4):3302–3312, 2014.

[22] Anthony J. Morfa, Kathy L. Rowlen, Thomas H. Reilly, Manuel J. Romero, and Jao Van De Lagemaat. Plasmon-enhanced solar energy conversion in organic bulk heterojunction photovoltaics. *Appl. Phys. Lett.*, 92(1):2008–2010, 2008.

[23] J. L. Wu, F. C. Chen, Y. S. Hsiao, and F. C. Chien. Surface plasmonic effects of metallic nanoparticles on the performance of polymer bulk heterojunction solar cells. *ACS Nano*, 5(2):959–967, 2011.

[24] Luyao Lu, Zhiqiang Luo, Tao Xu, and Luping Yu. Cooperative plasmonic effect of Ag and Au nanoparticles on enhancing performance of polymer solar cells. *Nano Lett.*, 13(1):59–64, 2013.

[25] Linfang Qiao, Dan Wang, Lijian Zuo, Yuqian Ye, Jun Qian, Hongzheng Chen, and Sailing He. Localized surface plasmon resonance enhanced organic solar cell with gold nanospheres. *Appl. Energy*, 88(3):848–852, 2011.

[26] Fang Chung Chen, Jyh Lih Wu, Chia Ling Lee, Yi Hong, Chun Hong Kuo, and Michael H. Huang. Plasmonic-enhanced polymer photovoltaic devices incorporating solution-processable metal nanoparticles. *Appl. Phys. Lett.*, 95(1):93–96, 2009.

[27] Sheridan Few, Jarvist M. Frost, and Jenny Nelson. Models of charge pair generation in organic solar cells. *Phys. Chem. Chem. Phys.*, 17(17):2311–2325, 2015.

[28] Monishka Rita Narayan and Jai Singh. Roles of binding energy and diffusion length of singlet and triplet excitons in organic heterojunction solar cells. *Phys. Status Solidi*, 9(12):2386–2389, 2012.

[29] Askat E. Jailaubekov, Adam P. Willard, John R. Tritsch, Wai-Lun Chan, Na Sai, Raluca Gearba, Loren G. Kaake, Kenrick J. Williams, Kevin Leung, Peter J. Rossky, and X-Y Zhu. Hot charge-transfer excitons set the time limit for charge separation at donor/acceptor interfaces in organic photovoltaics. *Nat. Mater.*, 12(1):66–73, 2013.

[30] Hiroyuki Tamura and Irene Burghardt. Ultrafast charge separation in organic photovoltaics enhanced by charge delocalization and vibronically hot exciton dissociation. *J. Am. Chem. Soc.*, 135(44):16364–16367, 2013.

[31] Minh Trung Dang, Lionel Hirsch, and Guillaume Wantz. P3HT:PCBM, Best Seller in Polymer Photovoltaic Research. *Adv. Mater.*, 23(31):3597–3602, 2011.

[32] Bo Wu, Xiangyang Wu, Cao Guan, Kong Fai Tai, Edwin Kok Lee Yeow, Hong Jin Fan, Nripan Mathews, and Tze Chien Sum. Uncovering loss mechanisms in silver nanoparticle-blended plasmonic organic solar cells. *Nat. Commun.*, 4(2004):1–7, 2013.

[33] Holly F. Zarick, William R. Erwin, Abdelaziz Boulesbaa, Olivia K. Hurd, Joseph A. Webb, Alexander A. Puretzky, David B. Geohegan, and Rizia Bardhan. Improving Light Harvesting in Dye Sensitized Solar Cells using Hybrid Bimetallic Nanostructures. *ACS Photonics*, 3:385–394, 2016.

[34] William R. Erwin, Andrew Coppola, Holly F. Zarick, Poorva Arora, Kevin J. Miller, and Rizia Bardhan. Plasmon enhanced water splitting mediated by hybrid bimetallic Au-Ag core-shell nanostructures. *Nanoscale*, 6:12626–12634, 2014.

[35] P. F. Liao and A. Wokaun. Lightning rod effect in surface enhanced Raman scattering. *J. Chem. Phys.*, 76(1):751–753, 1982.

[36] J. Grand, M. Lamy De La Chapelle, J. L. Bijeon, P. M. Adam, A. Vial, and P. Royer. Role of localized surface plasmons in surface-enhanced Raman scattering of shape-controlled metallic particles in regular arrays. *Phys. Rev. B - Condens. Matter Mater. Phys.*, 72(3):1–4, 2005.

[37] William R. Erwin, Holly Zarick, Eric M. Talbert, and Rizia Bardhan. Light Trapping in Mesoporous Solar Cells with Plasmonic Nanostructures. *Energy Environ. Sci.*, 9:1577–1601, 2016.

[38] R. Kern, R. Sastrawan, J. Ferber, R. Stangl, and J. Luther. Modeling and interpretation of electrical impedance spectra of dye solar cells operated under open-circuit conditions. *Electrochim. Acta*, 47(26):4213–4225, 2002.

[39] Yuan Zhang, Xuan-dung Dang, Chunki Kim, and Thuc-quyen Nguyen. Effect of Charge Recombination on the Fill Factor of Small Molecule Bulk Heterojunction Solar Cells. *Adv. Energy Mater.*, 1:610–617, 2011.

[40] R. Alex Marsh, Justin M. Hodgkiss, and Richard H. Friend. Direct measurement of electric field-assisted charge separation in polymer: Fullerene photovoltaic diodes. *Adv. Mater.*, 22(33):3672–3676, 2010.

[41] V. I. Arkhipov and H. Bässler. Exciton dissociation and charge photogeneration in pristine and doped conjugated polymers. *Phys. Status Solidi*, 201(6):1152–1187, 2004.

[42] Matthias Muntwiler, Qingxin Yang, William A. Tisdale, and X. Y. Zhu. Coulomb barrier for charge separation at an organic semiconductor interface. *Phys. Rev. Lett.*, 101(19):1–4, 2008.

[43] James W. Kingsley, Adam Green, and David G. Lidzey. Fabrication and Optimization of P3HT:PCBM Organic Photovoltaic Devices James. *Proc. SPIE*, 7416:74160T–74160T–9, 2009.

[44] John R. Tumbleston, Doo Hyun Ko, Edward T. Samulski, and Rene Lopez. Electrophotonic enhancement of bulk heterojunction organic solar cells through photonic crystal photoactive layer. *Appl. Phys. Lett.*, 94(4):043305–1–3, 2009.

[45] John R. Tumbleston, Doo-Hyun Ko, Edward T. Samulski, and Rene Lopez. Absorption and quasiguided mode analysis of organic solar cells with photonic crystal photoactive layers. *Opt. Express*, 17(9):7670–7681, 2009.

Chapter 4

COMPUTATIONAL INVESTIGATION OF PLASMON ENHANCED OPVS

4.1 Summary

In this chapter, we use optical and electrical simulations to investigate silver nanosphere enhanced PCDTBT:PCBM OPVs. We find that in addition to improving light absorption in the visible region (λ = 450-650 nm), the spatial electric field distribution in the light absorbing layer is altered with the presence of Ag nanospheres adjacent hole transporting layer. Our results are in agreement with results in Chapter 3, where overall power conversion efficiency in an OPV is improved as a result of improved transport despite the overall light absorption in the active layer decreasing. This chapter provides a framework to guide simulations and experiments for further optimization of plasmon enhanced organic photovoltaics in the future.

4.2 Introduction

In this chapter, we use computational methods to quantitatively investigate the mechanism of plasmonic metal nanostructures for radiative enhancement of thin film poly[2,6-(4,4-bis-(2-ethylhexyl)-4H-cyclopenta[2,1-b;3,4-b']dithiophene)-alt-4,7-(2,1,3-benzothiadiazole)] (PCPDTBT):[6,6]-phenyl C_{61} butyric acid methyl ester (PCBM) OPVs. Due to its poor absorption in the visible spectrum (450-650 nm) typically, PCPDTBT is used in tandem solar cells in conjunction with another polymer, however in this chapter we investigate the use of a plasmonic nanoparticle sensitizer to improve the full spectrum light absorption. As we discuss briefly in Chapter 3, purely optical simulations are not sufficient to describe the enhancement effects in plasmon enhanced organic photovoltaics. Possible mechanisms for enhancement of OPVs via the incorporation of plasmonic nanoparticles have been sug-

gested, including hot carrier injection,[1] plasmon-exciton coupling,[2, 3] and purely optical enhancement.[4, 5, 6] As discussed in Chapter 3, improved performance in a variety of thin film OPV systems via plasmon enhancement has been observed, however the precise mechanism by which enhancement occurs merits further investigation. Likely, plasmon enhancement in organic photovoltaics results from a combinatorial effect resulting from improved absorption and in certain cases plasmon-exciton coupling and hot-carrier injection. In transport a limited system, distortion of the electric field such that enhancement occurs near active layer - hole conductor interface may lead to improvement of the power conversion efficiency because the system is no longer transport limited due to the high concentration of minority carriers near the interface; even in the case that the overall light absorption in the active layer is not improved. The overall power conversion efficiency, which we is proportional to the wavelength dependent external quantum efficiency (EQE) goes according to the following relation:[7, 8, 4]

$$EQE(\lambda) = \eta_{abs} \times \eta_{gen} \times \eta_{coll} \tag{4.1}$$

Where η_{abs} is the ratio of absorbed light to incident light, η_{gen} is the ratio of photoexcited excitons that are converted to free carriers, and η_{coll} is the carrier collection efficiency at the electrodes. According to relation 4.1, we cannot solely pay attention to increased absorption of light to justify improvements in EQE, but must also take into effect the exciton generation efficiency as well as the charge collection efficiency. This chapter is divided into two parts: *i)* Simulation of plasmonic nanoparticles for radiative enhancement of PCPDTBT:PCBM OPVs, and further optical simulation of plasmonic nanoparticles embedded in the hole conducting layer of a PCPDTBT:PCBM OPV, and *ii)* electrical simulation of plasmon enhanced PCPDTBT:PCBM OPVs. Optical simulations are carried out using the Lumerical's finite-difference time-domain (FDTD) optical solver, and electronic simulations are carried out using the general-purpose photovoltaic device model (GPVDM). Plasmon enhanced PCPDTBT:PCBM OPVs represented in Fig-

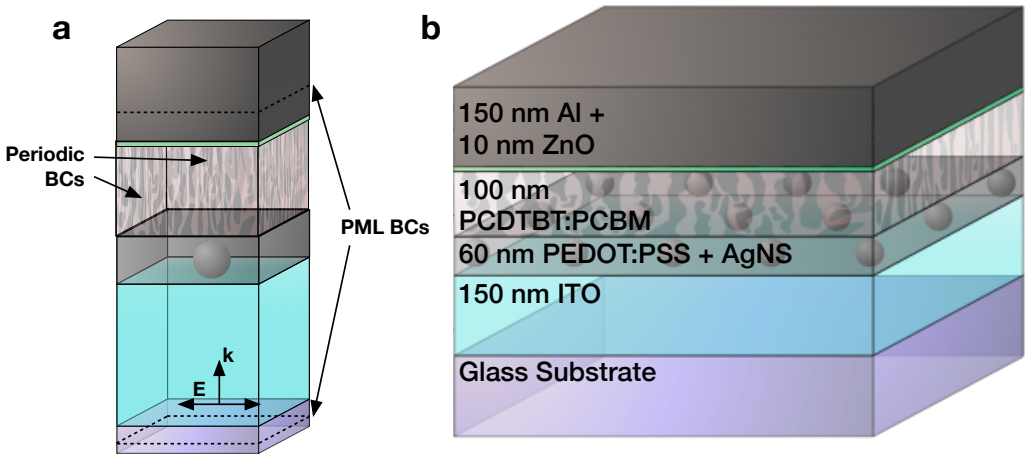

Figure 4.1: (a)Sketch of plasmon enhanced OPV system. (b) Simulation schematic of plasmon enhanced OPV setup.

ure 4.1 are based on systems in which enhancement has been observed experimentally in the literature.[9, 6]

4.3 Results and Discussion

In the PCDTBT:PCBM system, the hole mobility is an order of magnitude larger than the electron mobility - indicating that it is hole-limited, therefore the presence of AgNSs near the hole collection layer may provide an avenue to enhancement through the distortion of the electric field concentration and subsequent generation rate. Silver nanospheres (AgNS) are particularly suited for use in buffer layer enhancement of OPVs because *i)* Ag has relatively low losses when compared with other potential plasmonic metals(Au) (Figure 1.5), *ii)* AgNS are easily fabricated by colloidal synthesis, and *iii)* the resonance of Ag overlaps with the absorbance of PCPDTBT in the visible spectral range. Absorption and scattering are calculated in Lumerical FDTD solutions using the total-field scattered-field (TFSF) incident light source, as shown in Figure 4.3.

The function of the TFSF source is to inject a source frequency (in this case a pulse spanning the 350-800 nm frequency range) into a specific simulation volume where it interacts with a nanostructure. The injected incident field is then removed outside the TFSF

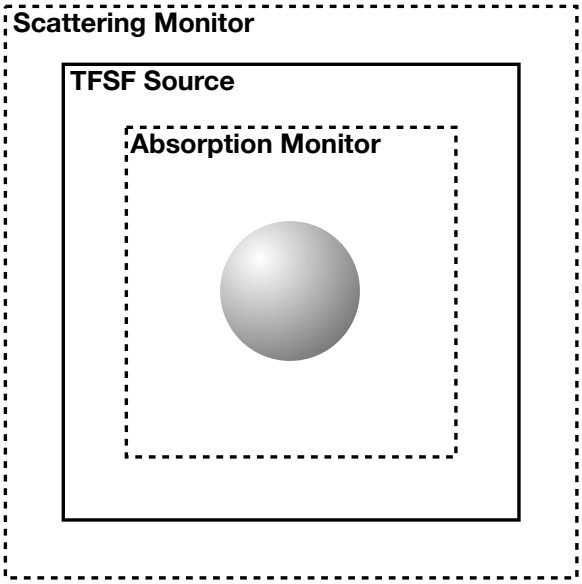

Figure 4.2: Total Field Scattered Field (TFSF) schematic.

boundaries, allowing us with a simple energy balance (scattering monitor) to measure the scattering cross section by calculating the net energy that crosses the scattering monitor boundary. Additionally, we calculate the absorption cross section using the absorption monitor, which records and calculates the net power that enters the nanoparticle boundary but is not re-radiated away from the nanoparticle. As discussed in Chapter 1, absorbed light may be converted to heat or hot carriers, however, the optical model we employ does not take into account hot carrier generation. Hot carrier generation is more prevalent in smaller nanostructures (<50 nm), as the mean free path of free carriers in Au and Ag is on the order of 50 nm.[10, 11, 12]

As the radius of the AgNS increases (Figure 4.3a), two notable effects occur *i)* The extinction spectrum red-shifts due to phase retardation effects i.e. the plasmon oscillation slows as a result of a larger volume and *ii)* the ratio of scattering to absorption increases as the volume increases due to the r^6 scaling, as discussed in Chapter 1, Equation 1.1 and shown in Figure 1.4. We limited the nanosphere radius to 25 nm in order to fit within the spatial limitations of the hole transport layer, which is typically <60 nm in thickness. The absorption and scattering cross sections of the 25 nm AgNS are shown in Figure 4.3b,

the scattering overlaps with poor absorption of PCPDTBT (Figure 4.3c) and will serve to enhance the electric fields in the vicinity of the nanoparticle. Because we are primarily interested in the optical effects of adding plasmonic nanoparticles to the buffer layer of an OPV, absorbed light is not accounted for in our simulations, additionally, absorption is minimal in comparison to scattering.

We conducted optical simulations of nanoparticles embedded into the hole transport layer of a PCPDTBT:PCBM OPV with a layer structure of 150 nm ITO/60 nm PEDOT:PSS/100 nm PCPDTBT:PCBM/10 nm ZnO/100 nm Al. The structure was adopted as a hybrid from the body of literature in plasmon enhanced OPVs, and is realistic for a high performance OPV.[9, 6] Optical coefficients for standard materials used in our model were taken from Lumerical's materials database, and coefficients for the active layer were adapted from the literature.[13, 14, 15] The simulation setup is shown in Figure 4.1, and constitutes an AgNS embedded in the hole transport layer (PEDOT:PSS), where radiated fields reach into the active layer and modulate absorption in the active material. Periodic boundary conditions are used in the lateral direction, as they provide a feasible route to realistic large scale simulations of thin film PVs. While it is unlikely that ordered arrays of nanoparticles, as are represented by periodic simulation boundary conditions, could cheaply and effectively be realized in large scale devices experimentally, it has been shown in other thin film systems that periodic structures do not necessarily present any advantage over random arrays, and the periodic results approximate the real world system.[16, 17] Perfectly matched layer (PML) absorbing boundary conditions are used in the z-dimension to simulate dissipation into free space (i.e. to avoid internal reflections which introduce error into the simulation). Upon simulation convergence, the electric field concentration in the active layer is recorded - this can be used to compute the spatially variant generation rate which can then be imported into an electrical solver to simulate solar cell performance under real world conditions.

We calculated the power absorbed (P_{abs}) by the active layer as a function of wavelength

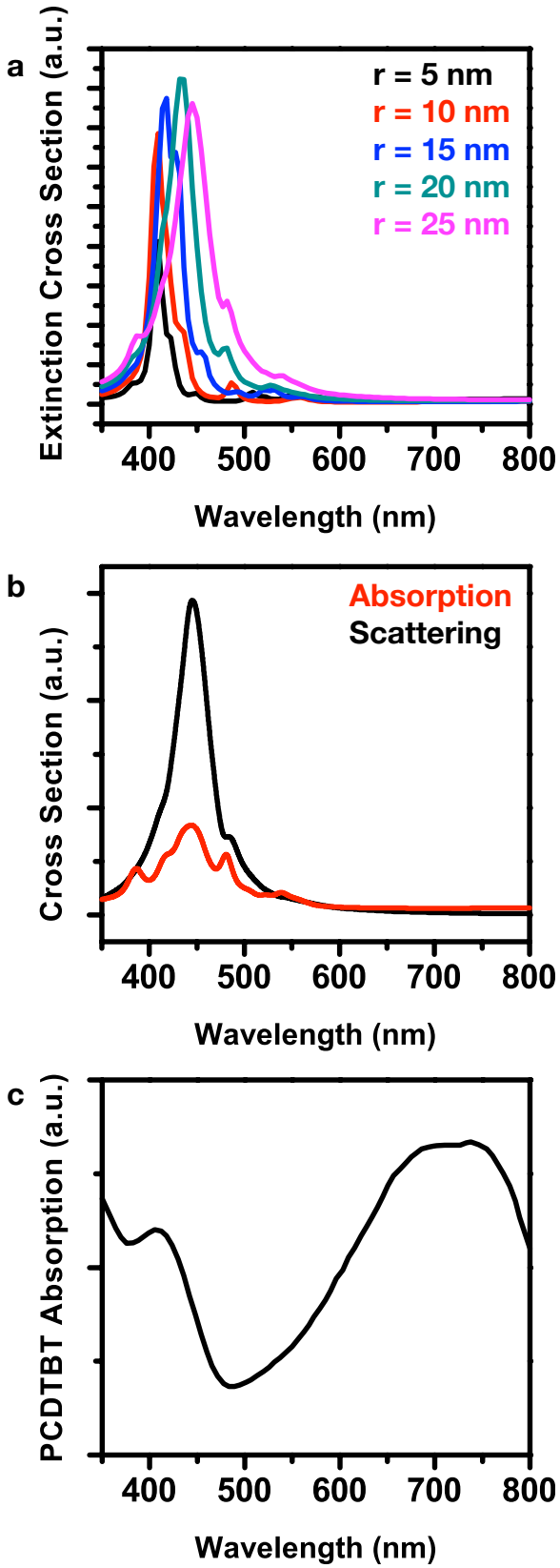

Figure 4.3: (a) Extinction spectra of 5-25 nm AgNS, (b) Absorption and scattering profiles of 25 nm AgNS and (c) the absorption of PCPDTBT .

for two series' of test: variable pitch (center-to-center distance between nanoparticles), and variable nanosphere radius. The input power was the AM 1.5G solar spectrum (100 mW/cm^2). The power absorbed in Figure 4.4 represents the fraction of power absorbed by the active layer of the total power injected into the simulation, as a function of wavelength or photon energy and is calculated according to Equation 4.2.

$$P_{abs} = \omega \left|E^2\right| \varepsilon_2 \tag{4.2}$$

where ω is the frequency, E is the electric field calculated via the FDTD method, and ε_2 is the imaginary part of the dielectric constant of the active material. As would be expected from absorption shown in Figure 4.3b, the power absorption minimum overlaps with the minimum in the extinction coefficient in the spectral range of 450-650 nm. With the presence of all Ag nanospheres, we see a decrease in active layer absorption $<$450 nm, which is compensated by an increase in absorption in the range of 450-650 nm. The decrease in absorption is caused by the combination of the absorption cross section (photons that are absorbed by the metal before they reach the active layer), and the portion of the scattering cross section that essentially reflects incident light away from the active layer. Interestingly, the increase in absorption in the active layer in the 450-650 nm range occurs at the low energy end of the scattering cross section, where only a small amount of light is being absorbed by the AgNS. The trend in Figure 4.4a goes as expected; smaller AgNS cause less light blocking due to it's overall small optical cross section, but increased absorption in the active layer is minimized due to the nanoparticle's small scattering cross section.

As the size of the AgNS increases, its extinction cross section increases, thus blocking more light from reaching the active layer in the high energy region of the spectrum, however, the portion of the scattering cross section resulting from light scattering increases in relation to the portion attributable to light absorption, thus increasing the light concentration in the active layer in the 450-650 nm range of the spectrum. Figure 4.4b shows the power absorbed vs. wavelength for 25 nm radius AgNSs in simulations with variable

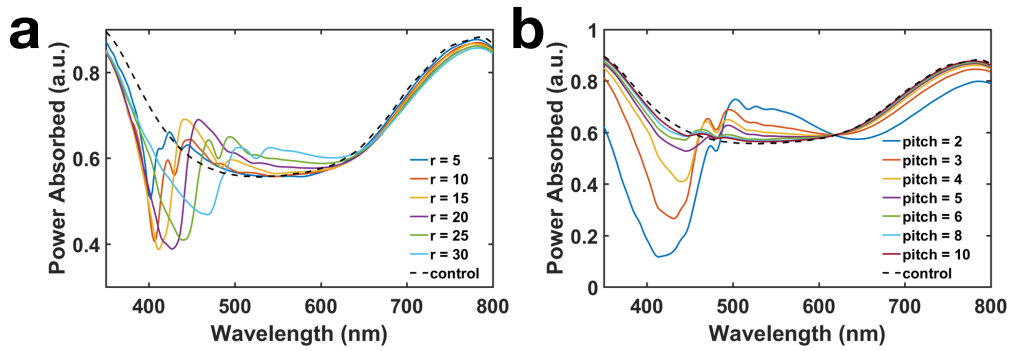

Figure 4.4: Power absorbed in plasmon enhanced PCPDTBT:PCBM OPVs sweeping over (a) nanosphere size with a constant pitch of 4 $\times$ D and (b) nanosphere pitch with a constant radius of 25 nm.

pitch from 2-10 (100 nm - 500 nm). At very low pitch, the light blocking overwhelms any positive effects that the presence of the AgNS may have, at very high pitch, the increase in absorption is minimized, however it is impossible to discern the effect on power conversion efficiency without electrical simulations.

While we have thus far looked only at the wholesale effect on absorption as a function of wavelength caused by the presence of AgNSs, the effects on the spatial electric field distribution in the active layer are important to consider. The introduction of plasmonic nanoparticles into layers adjacent to the active layer introduces non-homogeneity into the electric field in the active layer. One notable effect resulting from the addition of plasmonic nanoparticles into the hole-conducting layer is that intense near-fields emanating from nanoparticles tend to concentrate light near the interface of the hole-conducting layer and the active layer. As shown in Figure 4.4, the active layer absorption is not unilaterally increased with the presence of plasmonic nanoparticles. We integrated P_{abs} over the solar spectrum to determine the sum of light absorbed by the active layer. In the sweep over AgNS size and pitch light absorption in fact decreases rather than increases as one would expect.

In order to investigate the effect of field concentration near the active layer/buffer layer interface on the performance of the PCPDTBT:PCBM solar cell, we calculated the spatially

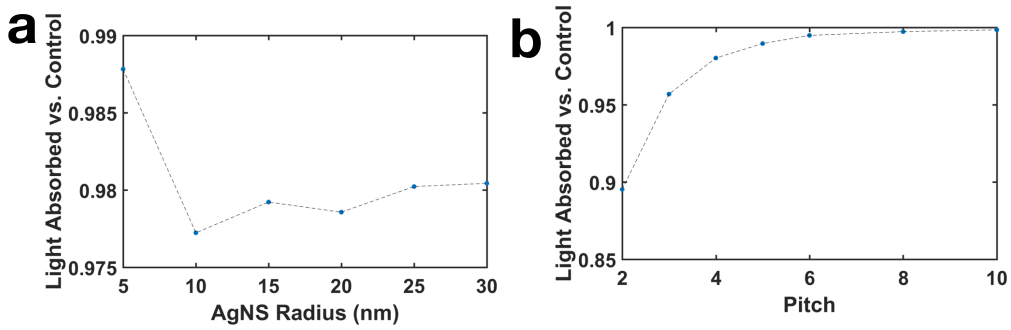

Figure 4.5: Fraction of light absorbed in relation to control OPV with (a) variable AgNS size and (b) variable AgNS pitch.

averaged carrier generation for solar cells with variable AgNS radius and pitch. We used Lumerical's solar generation rate calculation tool to use results from the optical simulation to calculate the exciton generation rate in the OPV. The generation rate is calculated by dividing P_{abs} by the energy per photon and integrating over the solar spectrum. The resulting carrier generation rate in Figure 4.6 is given as a function of x, the depth of the active layer (210 nm corresponds to the bottom of the active layer near the HTL, and 310 nm corresponds to the top of the active layer far from the embedded nanoparticle). It is notable that at high concentrations for each nanostructure, the region close to the HTL has a significantly increased generation rate when compared with the control device, however the spike in generation rate near the HTL/active layer interface is countered with a drop in generation rate in the region far (>15 nm) from the AgNS. Because the calculation method for exciton generation rate is directly proportional to the power absorbed, the overall generation rate follows the same trend seen in Figure 4.5.

While it is counter-intuitive that an overall reduction in electric field, and thus light absorption through the active layer can result in overall performance enhancement, it is important to note that an increased photocurrent may be resultant of improved charge collection, η_{coll} in Equation 4.1. One cause for poor carrier collection is an imbalance in charge mobility of electrons and holes. The electron mobility in PCPDTBT is an order of magnitude higher than the hole mobility, which may cause the device to be "hole

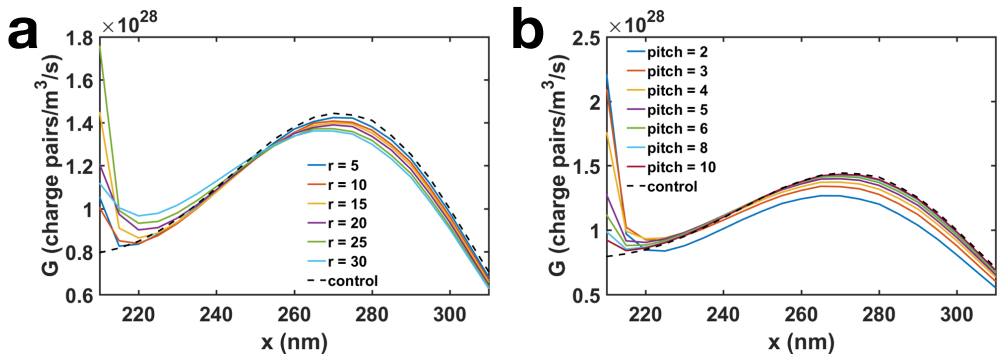

Figure 4.6: Generation rate in plasmonic and control device for sweeps over (a) AgNS radius and (b) AgNS pitch.

limited."[18, 13, 19, 20] By inserting nanoparticles into the hole transport layer, the strong electric field near the HTL/active layer interface provides an excess of holes that have a relatively short distance to diffuse to be collected. In addition to charge carrier mobility imbalance, charge trapping plays a detrimental role in the performance of polymer BHJ solar cells, as the distance that charge carriers diffuse decreases, the chance for charge trapping also decreases.

For electrical simulations, we employed the General-Purpose Photovoltaic Device Model (GPVDM).[21, 22] Upon inputting a generation rate profile into GPVDM, the model uses the finite difference method to solve electron and hole drift diffusion equations as well as the carrier continuity equations to describe the movement of charges in the device in one dimension. Recombination is taken into account by Langevin (free carrier) recombination, as well as Shockley-Read-Hall (free-to-trap) recombination.[23, 24] Using this approach, the carrier population is solved in both position and energy space.

Using GPVDM, we calculated the OPV performance over a potential range of -0.1V - 1V for the sweeps over AgNS radius and pitch, the results are shown in Figure 4.7. The results for the reference device are consistent with the literature for 100 nm PCPDTBT:PCBM devices.[13] Notably, the short circuit current densities shown in Tables 4.1 and 4.2 from the electrical simulations are higher than would be expected from the purely optical simulations and the results given in Figure 4.5. We attribute this improved current density to

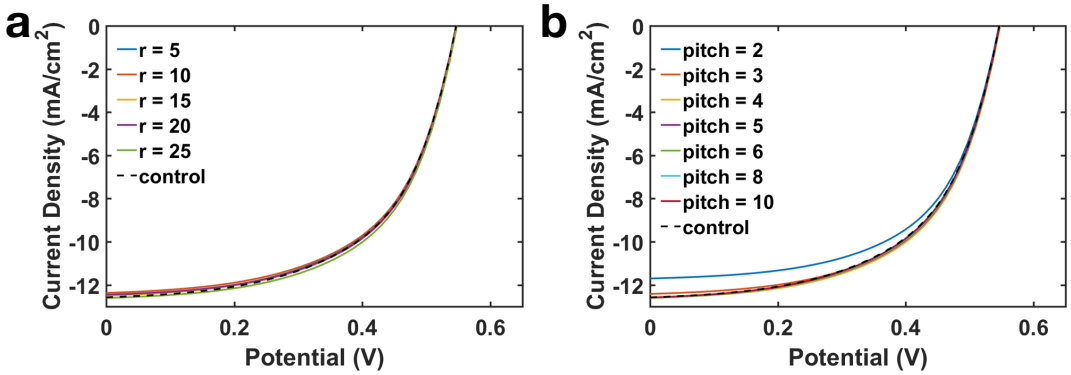

Figure 4.7: Calculated current-potential scans for sweeps over (a) AgNS radius and (b) AgNS pitch.

Table 4.1: Average plasmon enhanced PCPDTBT:PCBM device parameters (AgNS pitch sweep)

Pitch	J_{sc} (mA/cm^2)	V_{oc} (V)	FF	PCE (%)
0	12.58	0.55	0.57	3.93
2	11.71	0.55	0.59	3.78
3	12.42	0.55	0.58	3.98
4	12.61	0.55	0.58	4.01
5	12.59	0.55	0.58	3.98
6	12.61	0.55	0.57	3.97
8	12.59	0.55	0.57	3.95
10	12.59	0.55	0.57	3.94

the improved charge collection afforded by the highly concentrated electric field near the HTL/active layer interface.

We note that the short circuit current density shows minimal improvement, even with the optimal device (25 nm AgNS with a pitch of 4), improving from 12.58 mA/cm^2 to 12.61 mA/cm^2. As expected, the open circuit voltage is unaffected by the presence of AgNS, as the internal resistances are not affected by the modulation of optical properties. In future work, the addition hot carrier injection may provide a more realistic picture of solar cell enhancement. Perhaps most interestingly, we observe a 3.5% enhancement in the fill factor for the 25 nm AgNS with a pitch of 2, and a 1.6% enhancement in the fill factor for the devices with the optimized radius and pitch. The improvement in fill factor results from an improvement in transport - charge collection is not limited by charge traps because of the

Table 4.2: Average plasmon enhanced PCPDTBT:PCBM device parameters (AgNS radius sweep)

Radius	J_{sc} (mA/cm^2)	V_{oc} (V)	FF	PCE (%)
0	12.58	0.55	0.57	3.93
5	12.49	0.55	0.57	3.91
10	12.37	0.55	0.57	3.88
15	12.51	0.55	0.58	4.94
20	12.46	0.55	0.58	3.94
25	12.61	0.55	0.58	4.01

concentration of excitons near the HTL.[25]

4.4 Conclusions

In this chapter, we have shown that improvement in the power conversion efficiency in organic photovoltaics is not necessarily the result of optical enhancement via improved light capture in the active layer, but rather is a result of field intensity modulation near the hole-transport layer/active layer interface. Future work in this area should focus on modification of the geometry and composition of the plasmonic nanostructure to minimize the absorption cross section, while maintaining a strong scattering cross section, as discussed in Chapter 5, it is possible to modify nanostructure geometry to induce preferential directional scattering. By minimizing backwards scattering and improving forward scattering by plasmonic nanostructures in the spectral regions in which active materials absorb poorly, it may be possible to improve the overall light absorption, resulting in higher enhancement. Additionally, it is possible to further refine the simulation results by calculating drift-diffusion, recombination and electrostatic potential in two or three dimensions, though higher dimensional simulations will result in a significant trade-off in complexity and computation cost.

4.5 Bibliography

[1] Chen Wang, Chang Li, Shanpeng Wen, Pengfei Ma, Yang Liu, Roderick C. I. Mackenzie, Wenjing Tian, and Shengping Ruan. Combining plasmonic trap fi lling and optical backscattering for highly efficient third generation solar cells. *J. Mater. Chem. A Mater. Energy Sustain.*, 5:3995–4002, 2017.

[2] Fang Chung Chen, Jyh Lih Wu, Chia Ling Lee, Yi Hong, Chun Hong Kuo, and Michael H. Huang. Plasmonic-enhanced polymer photovoltaic devices incorporating solution-processable metal nanoparticles. *Appl. Phys. Lett.*, 95(1):93–96, 2009.

[3] J. L. Wu, F. C. Chen, Y. S. Hsiao, and F. C. Chien. Surface plasmonic effects of metallic nanoparticles on the performance of polymer bulk heterojunction solar cells. *ACS Nano*, 5(2):959–967, 2011.

[4] Chun-Hsien Chou and Fang-Chung Chen. Plasmonic nanostructures for light trapping in organic photovoltaic devices. *Nanoscale*, 6(15):8444–8458, 2014.

[5] Woo-Jun Yoon, Kyung-Young Jung, Jiwen Liu, Thirumalai Duraisamy, Rao Revur, Fernando L. Teixeira, Suvankar Sengupta, and Paul R. Berger. Plasmon-enhanced optical absorption and photocurrent in organic bulk heterojunction photovoltaic devices using self-assembled layer of silver nanoparticles. *Sol. Energy Mater. Sol. Cells*, 94(2):128–132, 2010.

[6] Se Woong Baek, Jonghyeon Noh, Chun Ho Lee, BongSoo Kim, Min Kyo Seo, and Jung Yong Lee. Plasmonic Forward Scattering Effect in Organic Solar Cells: A Powerful Optical Engineering Method. *Sci. Rep.*, 3:1–7, 2013.

[7] Andre Molitin and Jean-Michel Nunzi. How to model the behaviour of organic photovoltaic cells. *Polym. Int.*, 55:583–600, 2006.

[8] S. Matthew Menke and Russell J. Holmes. Exciton diffusion in organic photovoltaic cells. *Energy Environ. Sci.*, 7(2):499–512, 2014.

[9] Luyao Lu, Zhiqiang Luo, Tao Xu, and Luping Yu. Cooperative plasmonic effect of Ag and Au nanoparticles on enhancing performance of polymer solar cells. *Nano Lett.*, 13(1):59–64, 2013.

[10] Fuming Wang and Nicholas A. Melosh. Power-independent wavelength determination by hot carrier collection in metal-insulator-metal devices. *Nat. Commun.*, 4:1711, 2013.

[11] Fuming Wang and Nicholas A. Melosh. Plasmonic Energy Collection through Hot Carrier Extraction. *Nano Lett.*, 11(12):5426–5430, 2011.

[12] Stephan Link and Mostafa A. El-Sayed. Shape and size dependence of radiative, nonradiative and photothermal properties of gold nanocrystals. *Int. Rev. Phys. Chem.*, 19(3):409–453, 2000.

[13] Steve Albrecht, Sebastian Schäfer, Ilja Lange, Seyfullah Yilmaz, Ines Dumsch, Sybille Allard, Ullrich Scherf, Andreas Hertwig, and Dieter Neher. Light management in PCPDTBT:PC70BM solar cells: A comparison of standard and inverted device structures. *Org. Electron. Physics, Mater. Appl.*, 13(4):615–622, 2012.

[14] P. B. Johnson and R. W. Christy. Optical Constants of the Noble Metals, 1972.

[15] Ardalan Armin, Gytis Juska, Mujeeb Ullah, Marappan Velusamy, Paul L. Burn, Paul Meredith, and Almantas Pivrikas. Balanced carrier mobilities: Not a necessary condition for high-efficiency thin organic solar cells as determined by MIS-CELIV. *Adv. Energy Mater.*, 4(4):1–8, 2014.

[16] Corsin Battaglia, Ching-mei Hsu, Karin Söderström, Jordi Escarré, Franz-josef Haug, Mathieu Charrière, Mathieu Boccard, Matthieu Despeisse, Duncan Alexander, Marco Cantoni, Yi Cui, and Christophe Ballif. Light Trapping in Solar Cells : Can Periodic Beat Random? *ACS Nano*, 6(3):2790–2797, 2012.

[17] Vivian E. Ferry, Marc A. Verschuuren, Hongbo B. T. Li, Ewold Verhagen, Robert J. Walters, Ruud E. I. Schropp, Harry A. Atwater, and Albert Polman. Light trapping in ultrathin plasmonic solar cells. *Opt. Express*, 18(2):A237–45, 2010.

[18] Gon Namkoong, Patrick Boland, Keejoo Lee, James Dean, Gon Namkoong, Patrick Boland, Keejoo Lee, and James Dean. Design of organic tandem solar cells using PCPDTBT : PC 61 BM and P3HT : PC 71 BM. *J. Appl. Phys.*, 107:124515, 2010.

[19] Tracey Clarke, Amy Ballantyne, Fiona Jamieson, Christoph Brabec, Jenny Nelson, and James Durrant. Transient absorption spectroscopy of charge photogeneration yields and lifetimes in a low bandgap polymer/fullerene film. *Chem. Commun.*, 7345(1):89–91, 2009.

[20] Dong Hwan Wang, Do Youb Kim, Kyeong Woo Choi, Jung Hwa Seo, Sang Hyuk Im, Jong Hyeok Park, O. Ok Park, and Alan J. Heeger. Enhancement of Donor-Acceptor Polymer Bulk Heterojunction Solar Cell Power Conversion Efficiencies by Addition of Au Nanoparticles. *Angew. Chemie*, 123(24):5633–5637, 2011.

[21] Roderick C I Mackenzie, Christopher G Shuttle, Michael L Chabinyc, and Jenny Nelson. Extracting Microscopic Device Parameters from Transient Photocurrent Measurements of P3HT : PCBM Solar Cells COMMUNICATION. *Adv. Energy Mater.*, 2:662–669, 2012.

[22] Roderick C. I. Mackenzie, Thomas Kirchartz, George F. A. Dibb, and Jenny Nelson. Modeling Nongeminate Recombination in P3HT : PCBM Solar Cells. *J. Phys. Chem. C*, 115:9806–9813, 2011.

[23] Christopher M. Proctor, Martijn Kuik, and Thuc-Quyen Nguyen. Charge carrier recombination in organic solar cells. *Prog. Polym. Sci.*, 38(12):1941–1960, 2013.

[24] Fabian Etzold, Ian Howard, Ralf Mauer, Michael Meister, Tae Dong Kim, Kwang Sup Lee, Nam Seob Baek, and Frédéric Laquai. Ultrafast exciton dissociation followed by nongeminate charge recombination in PCDTBT:PCBM photovoltaic blends. *J. Am. Chem. Soc.*, 133(24):9469–79, 2011.

[25] Boyuan Qi and Jizheng Wang. Fill factor in organic solar cells. *Phys. Chem. Chem. Phys.*, 15(23):8972–82, 2013.

Chapter 5

APPLICATIONS FOR PLASMONICS BEYOND SOLAR ENHANCEMENT: DIRECTIONAL SCATTERING AND SENSING WITH BIMETALLIC FANOCUBES - A COMPLEX FANO-RESONANT PLASMONIC NANOSTRUCTURE

5.1 Summary

Concentric nanostructures provide a unique architecture to manipulate light by modification of their internal geometry with minimal changes to their overall size. In this chapter, we have theoretically examined, using finite difference time domain simulations, the plasmonic properties of a concentric cubic nanostructure consisting of a silver (Ag) core, silica (SiO_2) interlayer, and gold (Au) shell. These bimetallic fanocubes display two separate geometry dependent Fano resonances in the visible and in the near-infrared. We employed a plasmon hybridization model to understand the origin of the spectral features and observe distinct hybridized modes contributed by the edges and corners, which is unique to the cubic geometry. Specifically, we note that the nonbonding mode that is essentially dark and not observable in spherical concentric nanostructures is enhanced in the bimetallic fanocubes. We show the far-field properties, and Fano resonances of the fanocubes can be tuned by altering the thickness of the silica layer, the thickness of the Au shell, and by breaking symmetry. Further, we have examined the refractive index sensing and directional scattering abilities of the fanocubes to ultimately enable their use in a range of applications, harnessing their absorption and scattering properties.

5.2 Introduction

Subwavelength metal nanostructures have the unique ability to manipulate light enabled by the resonant oscillations of the conduction electrons defined as localized surface

plasmon resonances (LSPRs). By tuning the geometry and composition of metal nanostructures, their optical properties have been harnessed for a range of technological applications from light trapping in solar devices [1, 2, 3, 4, 5, 6, 7] to nanotherapeutics, [8, 9, 10, 11, 12] to ultrasensitive biosensing. [13, 14, 15, 16] Concentric metallodielectric nanostructures or nanomatryoshkas [17, 18] form an important class of plasmonic material where metallic layers are separated by dielectric spacers providing a highly tunable architecture [19, 20, 21, 22, 23, 24, 25, 26, 27, 28, 29] The LSPRs in this class of nanostructures are supported at the metal/dielectric interface, where the metal layers couple to form hybridized plasmons governed by the thickness of the dielectric spacer layer. [26, 30, 31, 32, 33] Such concentric nanostructures essentially behave as a collection of optical condensers concentrating incident light between the metal core and the adjacent, innermost metal shell generating intense localized near-fields.[34] In addition to their near-field characteristics, the far field properties of light absorption and scattering are also highly tunable in concentric nanostructures achieved by modulating the thickness of the dielectric interlayer with minimal alterations to their overall size. Recently, the plasmonic properties of the simplest concentric nanostructure, spherical gold/silica/-gold ($Au/SiO_2/Au$) metallodielectric nanoshells, have been extensively investigated both theoretically and experimentally.[22, 35, 36] The LSPRs of this simple nanomatryoshka have been examined with the plasmon hybridization model, and three distinct modes have been identified.[20, 23, 37, 38] The hybridization of the low-energy bonding Au nanoshell plasmon with the Au core plasmon gives rise to an antisymmetric bonding mode and a symmetric antibonding mode. Further, the hybridization of the high-energy antibonding nanoshell plasmon with the Au core plasmon results in a nonbonding mode, which is optically weak and essentially dark due to its small dipole moment. However, this nonbonding mode can either be completely turned-off or significantly enhanced when the composition of $Au/SiO_2/Au$ nanostructure is altered by either substituting the inner core or outer shell with Ag, respectively.[27] In addition to composition, these hybridized LSPRs can

also be tuned by changing the morphology of concentric nanostructure to nonspherical geometries[39, 32, 33, 40] or by breaking the symmetry of the nanostructure, essentially allowing optically dark modes to couple with bright modes and generate unique optical resonances.[28, 41, 42]

When bright plasmon modes, which are spectrally broad due to radiative damping, couple with spectrally narrow dark modes, this spectral interference gives rise to a characteristic asymmetric line shape described as a Fano resonance.[43, 44, 45, 46] Fano resonances in plasmonic nanostructures have been extensively studied in the past decade either driven by the interactions of adjacent nanoparticles such as in plasmonic oligomers,[47, 48, 49, 50, 51, 52] or by introducing asymmetry such as in ring/ disk systems,[53, 54, 55, 56]or by coupling a nanostructure with its adjacent substrate.[57, 58] Concentric metallodielectric nanostructures are specifically interesting, as they can be engineered to support multiple Fano resonances by manipulating their size, shape, composition, thickness of the dielectric layer, polar- ization of incident light, and breaking symmetry. Due to the intense near-field and far-field properties achieved at the Fano resonance, concentric nanostructures have been utilized in surface enhanced spectroscopies,[59, 36]optical sensing,[60, 61, 62, 63]as well as photothermal therapies.[64, 65]

In this work, we have theoretically investigated the optical characteristics of a bimetallic concentric nanostructure consisting of a cubic Ag core surrounded with a SiO_2 layer and outer cubic Au shell. These bimetallic fanocubes display multiple Fano resonances that are tunable by modulating the morphology, internal symmetry, and polarization of light. The plasmon hybridization model was employed to study the LSPRs of the fanocubes; we observed a strong contribution from corners and edges, which gives rise to additional hybridized plasmon modes not observable in spherical concentric nanostructures. Further, the cubic geometry of the fanocubes enhances the nonbonding mode that is essentially dark and not observable in spherical $Ag/SiO_2/Au$ nanostructures. The optical properties of fanocubes can be manipulated to preferentially absorb or scatter light with minimal mod-

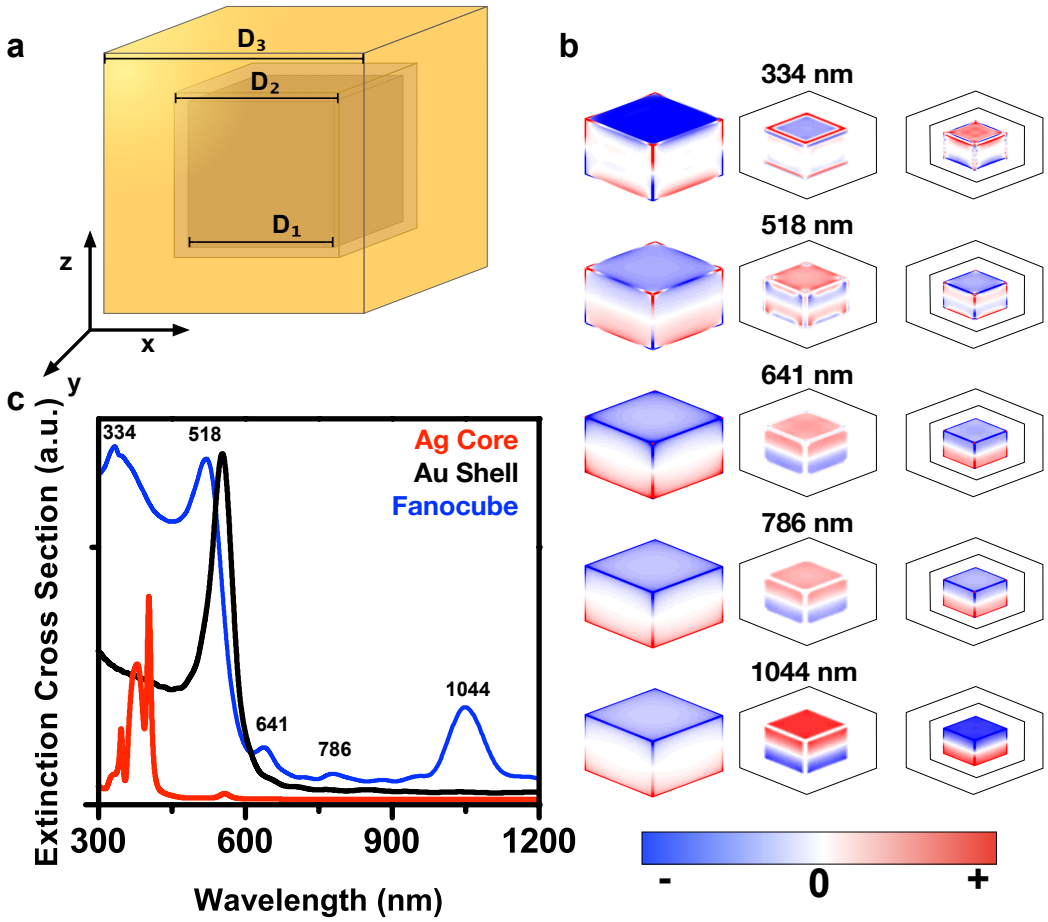

Figure 5.1: (a) Schematic of bimetallic fanocubes with relevant dimensions. (b) Surface charge plots of the fanocubes in quasi-static regime for the outer surface of Au shell (left), inner surface of Au shell (middle), and Ag surface (right) at various resonance energies. (c) Extinction of individual components, Ag nanocube core and Au cubic nanoshell, and the bimetallic fanocubes in the quasi-static regime simulated in nonabsorbing, index 1 media. The main resonant peaks of the fanocubes are labeled to correspond with the charge plots.

ifications of their overall size, a phenomenon highly useful in several applications including optical sensing. We studied the refractive index sensing capability of a 110 nm sized bimetallic fanocube yielding a high sensitivity of 300 nm/RIU and figure of merit ~4.55. Further we also studied the angular light scattering ability of the fanocubes demonstrating exceptional forward scattering in the visible and near-infrared, which can be potentially useful in directional color routing as well as light harvesting in solar devices.

5.3 Results and Discussion

The plasmon modes of the concentric bimetallic fanocube consisting of an Ag nanocube core, SiO_2 shell, and outer Au cubic nanoshell (Figure 5.1a), can be understood as a hybridization of the LSPRs of its individual components. To understand the origin of the resonance modes, we performed finite difference time domain (FDTD) electrodynamics simulations of bimetallic fanocubes in the quasi-static regime (edge length, $D << \lambda$) with a size of $[D_1, D_2, D_3]$ = [6, 7, 11] nm and a mesh size of 0.7 Åover a spectral range of 300-1200 nm. The quasi-static structure is a simplified version of the fanocube and neglects any higher order modes that arise from phase retardation effects observed in the realistic size-regime.[21, 22, 23, 31] When the optical modes of vicinal nanostructures interact, the plasmon modes couple either in-phase or out-of-phase, which gives rise to antibonding and bonding plasmon modes, respectively. In concentric nanostructures, the hybridization of the plasmon resonances is a function of the coupling strength, which is determined by the spacing between the individual metal layers supporting the resonant modes. However, unlike concentric spherical nanostructures, which only give rise to three hybridized modes, the plasmon hybridization of bimetallic fanocubes is highly complex due to the interactions of corners and edges in the cubic geometry. We calculated the charge density distribution in the fanocubes at discrete eigenmodes (Figure 5.1b), which can be understood by examining the resonances of the individual components of the bimetallic fanocube.

The Ag core has dipolar modes at 405, 380, and 347 nm, which have strong contribu-

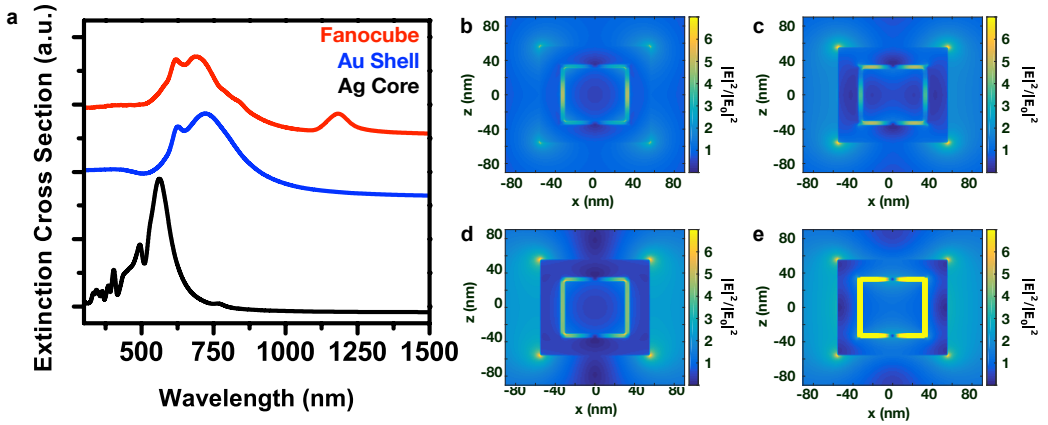

Figure 5.2: (a) Extinction spectra of 60 nm Ag Core, 110 nm Au shell, and [D1,D2,D3] = [60, 70, 110] nm bimetallic fanocube. Electric field profiles normal to the incident plane wave are shown at (b) 615 nm, (c) 687 nm, (d) 845 nm, and (e) 1172 nm

tions from the corners and edges (Figure 5.1c). The Au cubic nanoshell has strong bonding mode at 570 nm, an antibonding mode at 520 nm, and weak bonding modes at 640, 700, and 770 nm, which are contributed by the edges and corners. The bimetallic fanocube has five distinct hybridized modes; the peaks at 641 and 786 nm both have bonding characteristics contributed by the Au nanoshell edges and corners; however, there is a stronger localization of negative charge at the corners of the inner Au shell at 641 than at 786 nm. Further, there is significant antibonding character at the corners of the outer Au shell at 641 nm that is not present at 786 nm. The 1044 nm peak arises from the interactions of the bonding Au cubic nanoshell plasmon and the Ag nanocube plasmon, giving rise to asymmetric hybridized bonding mode $|\omega_{-}^{-}\rangle$ with strong contributions from the edges and corners of the Ag nanocube core. The peak at 518 nm is rather interesting with both bonding and antibonding characteristics. It results from the interactions of the bonding Au cubic nanoshell plasmon and Ag nanocube plasmon, giving rise to antisymmetric coupling ($|\omega_{-}^{-}\rangle$) with an admixture of symmetric coupling ($|\omega_{-}^{+}\rangle$) from the corners of the Ag core and Au shell. The peak at 334 nm is also a complex mode arising from the interactions of the antibonding Au cubic nanoshell plasmon and Ag nanocube plasmon, giving rise to symmetric coupling ($|\omega_{+}^{-}\rangle$) with an admixture of asymmetric coupling from the edges of the Ag core and shell

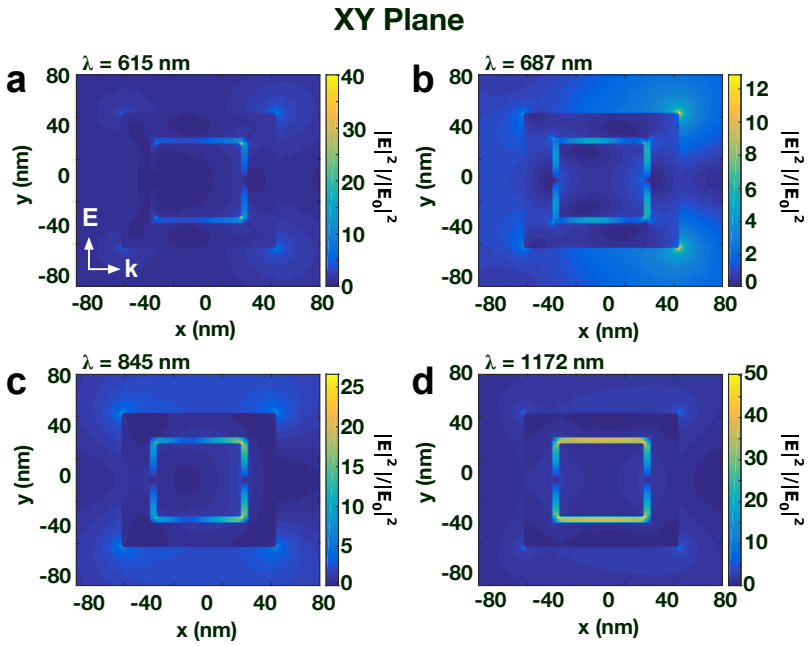

Figure 5.3: E-Field profiles for the [D1,D2,D3] = [60, 70, 110] nm bimetallic fanocube in the XY plane at (a) 615 nm, (b) 687 nm, (c) 845 nm adn (d) 1172 nm.

($|\omega_-^-\rangle$). In concentric spherical Au/SiO_2/Au nanomatroyushkas, this $|\omega_+^-\rangle$ mode has been described as nonbonding since it weakly interacts with incident light and is typically dark due to its appreciable antibonding character.[22, 20, 37] Zhu et al.[27] recently suggested that in an Ag core/SiO_2/Au shell bimetallic nanomatryoshka, the nonbonding mode completely disappears. However, our simulations show that in the bimetallic fanocubes, the nonbonding mode is enhanced by the strong intermetallic interactions of the edges and corners as a result of the cubic geometry. The insight from plasmon hybridization in the quasi- static regime is used throughout the manuscript to explain the spectral behavior in the realistic regime where Fano resonances appear for the bimetallic fanocubes.

We examined the LSPRs of the bimetallic fanocubes in the realistic size-regime by simulating fanocubes of size [D_1, D_2, D_3] = [60, 70, 110] nm and decoupling the observed resonance modes by examining its individual components (Figure 5.2a). The characteristic plasmon peaks in the realistic size regime is analogous to that observed in Figure 5.1a, with significant broadening and red-shifting of peaks due to phase retardation effects. Two

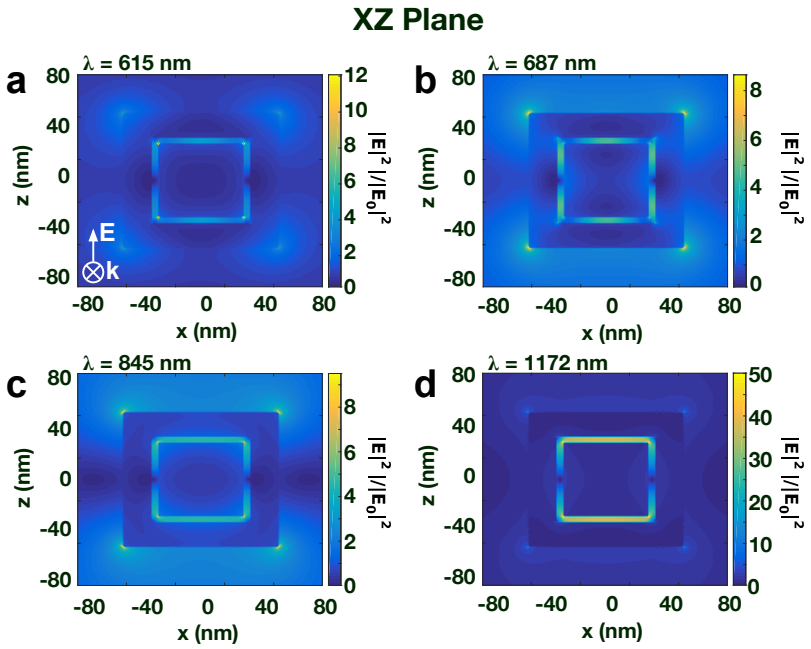

Figure 5.4: E-Field profiles for the [D1,D2,D3] = [60, 70, 110] nm bimetallic fanocube in the XZ plane at (a) 615 nm, (b) 687 nm, (c) 845 nm adn (d) 1172 nm.

distinct Fano resonances are observed in the fanocube geometry in this size regime characterized by their asymmetric line shape: a low energy infrared peak at 1172 nm as well as one in the visible at 615 nm. To further understand the origin of the Fano resonances, we calculated the electric field profiles and examined the field enhancement in the three planes bisecting the fanocube. The electric-field profiles of the fanocube in the YZ plane normal to the incident light k vector are shown in Figure 5.2b-e. The E-field profiles of the fanocube in the XY and XZ planes are provided in Figures 5.3 and 5.4. The field profiles show hybridization of the two metal layers result in charge localization at both the corners of the Ag cube and Au shell at 615 and 687 nm (Figure 5.2b-c). These field profiles clarify that the Fano resonance of bimetallic fanocubes in the visible results from the interference of the broad dipolar resonance of the Au nanoshell with narrow resonances of the Ag nanocube primarily contributed by their edges and corners. The shoulder peak at 845 nm shows strong fields localized along the edges and corners of the Ag nanocube, demonstrating that this peak originates from the inner core (Figures 2d, 5.3c, and 5.4c). The

strongest E-fields are observed at the 1172 peak and are localized within the inner Ag cube (Figure 5.2e) and the surrounding SiO_2 interlayer (Figures 5.3d and 5.4d). We therefore attribute the Fano character of this peak to the overlap of the broad superradiant bonding plasmon modes of the Au cubic nanoshell and narrow subradiant mode contributed by the Ag nanocube corners and edges.

The dual Fano resonances of the bimetallic fanocubes are highly tunable by altering the dimensions of the outer Au shell, inner Ag cube, and thickness of the SiO_2 interlayer. We varied the outer Au layer while keeping the dimensions of the Ag nanocube core and the silica interlayer constant at D_1 = 60nm and D_2 = 70 nm, respectively (Figure 5.5a). At D_3 = 80 nm, several dipolar, quadrupolar, and other higher modes appear throughout the UV and visible region and into the infrared. The low energy infrared peak monotonically blue-shifts as D_3 increases, and attains the asymmetric line shape characteristic of a Fano resonance when D_3 = 110 nm. Notably, the Fano resonance in the visible at 615 nm also emerges at D_3 = 110 nm and red-shifts and increases in strength with an increase in D_3. A shoulder peak is also observed at 750 nm, which red-shifts as D_3 increases and originates from the interaction of the bonding plasmon of Au shell corners and Ag core corners. Further, we also examined the evolution of the Fano resonances in the bimetallic fanocubes by varying the thickness of the silica interlayer (Figure 5.5b). The strength of the Fano resonance in concentric nanostructures is governed by the coupling of the two metal layers, which is dependent on the spacing between the metal core and outer metal shell. As the silica layer thickness increases from D_2 = 70 to 100 nm, the Fano resonance in the visible diminishes in strength and ultimately loses its asymmetric line shape and eventually dissipates attributable to the loss of coupling between the Ag nanocube and Au nanoshell plasmons, as indicated by electric field profiles in Figure 5.6. Notably, the Fano resonance at 1172 nm initially blue-shifts and gains in strength when D_2 increase from 70 to 80 nm. As the thickness of the outer Au shell decreases, this gives rise to strong hybridization of the nanoshell cavity modes with the core plasmons analogous to that described previously

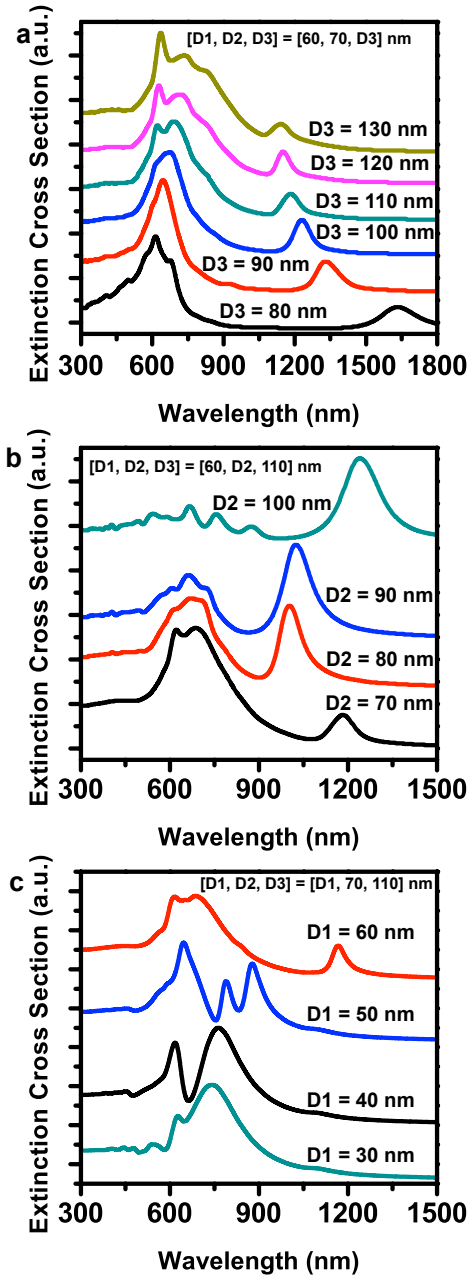

Figure 5.5: Extinction cross-section of bimetallic fanocubes with (a) dimensions of the Au shell varied while keeping dimensions of the Ag nanocube and SiO2 interlayer constant, (b) thickness of the SiO_2 shell, i.e., separation between inner Ag and outer Au, varied while keeping dimensions of the Ag nanocube and outer Au shell constant, and (c) dimensions of the inner Ag cubic core varied while keeping dimensions of the SiO_2 layer and Au shell constant.

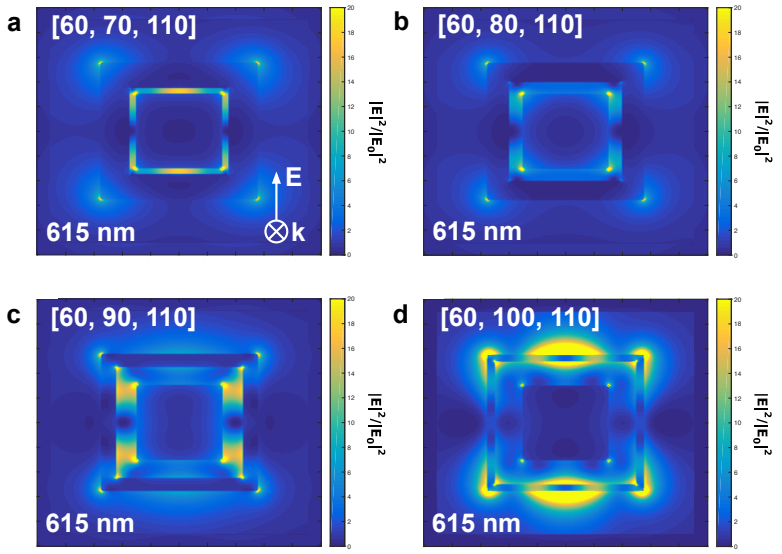

Figure 5.6: Electric field profiles of fanocubes with variable intermediate layer thickness at 615 nm (a) 70 nm SiO_2, (b) 80 nm SiO_2, (c) 90 nm SiO_2 and (d) 100 nm SiO_2.

for the nanomatryushkas.[17, 18] This results in a strong coupling between the Ag core and Au shell, which strengthens the Fano resonance. With further increase in the SiO_2 layer thickness, this low-energy Fano resonance red-shifts and broadens with a loss of its asymmetric line shape, and attains a dipolar resonance characteristic, which is attributable to the weak coupling between the two metallic layers, as indicated in electric field profiles in Figure 5.7. It is notable from the electric field profiles (Figure 5.6 and 5.7) that as the SiO_2 layer increases to 20 nm, i.e., [D_1, D_2, D_3] = [60, 100, 110] nm, the visible Fano resonance shows a complete decoupling of the Ag core and Au shell, whereas the near-infrared Fano resonance shows that the coupling between the core and shell weakens but never decouples. These trends in the field profiles correlate well with the spectral behavior shown in Figure 5.5b.

We also varied the dimensions of the Ag core and find an interesting trend where a 30 nm Ag nanocube gives rise to no interactions between the core and outer Au shell due to large silica (20 nm) spacer layer separating the two metallic layers. This results in an absence of Fano resonance at the smallest core dimensions. A strong Fano resonance

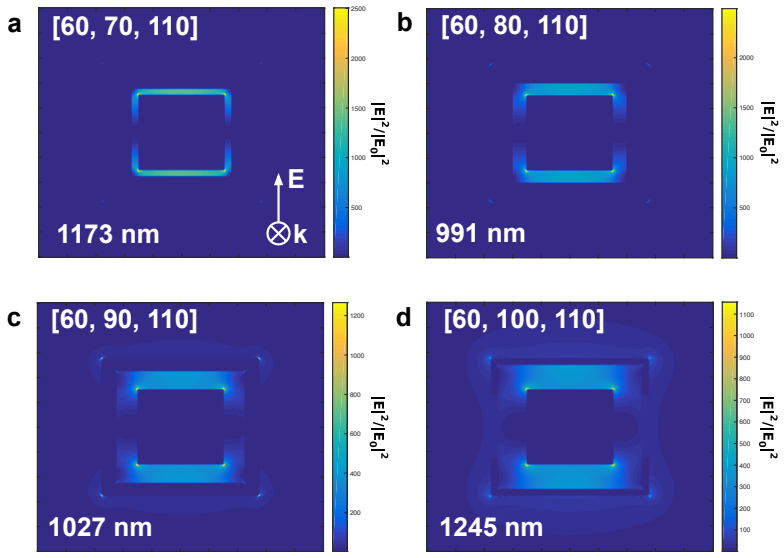

Figure 5.7: Electric field profiles of fanocubes with variable intermediate layer thickness at the peak wavelength of the near IR peak: (a) 1173 nm with 70 nm SiO_2, (b) 991 nm with 80 nm SiO_2, (c) 1027 nm with 90 nm SiO_2 and (d) 1245 nm with 100 nm SiO_2.

appears at the 40 nm Ag core size indicating SiO_2 layer thickness needs to be 15 nm to enable the broad Au nanoshell mode to interfere with the narrow Ag nanocube plasmons and give rise to a Fano dip. A further increase in the Ag core to 50 nm gives rise to a rather unique behavior where the broad peak red-shifts and splits into two Fano resonances. This unusual behavior likely stems from coupling between the edges and corners of the core and shell, which is enhanced when the separation between the layers reduces to 10 nm. When the Ag nanocube core increases to 60 nm, one of the split Fano peaks is observed to red-shift to the infrared, while the other Fano resonant mode merges with the peak in the visible to give rise to two distinct Fano resonances at 1172 and 615 nm. These results suggest, by varying the dimensions of each layer (Ag, SiO_2, and Au), the plasmonic modes of this complex nanostructure can be fine-tuned to achieve desired spectral behavior with either single or multiple Fano resonances.

In addition to tunable Fano behavior, the far-field optical properties of the bimetallic fanocubes can also be altered by varying the dimensions of the SiO_2 layer, Ag core, or Au

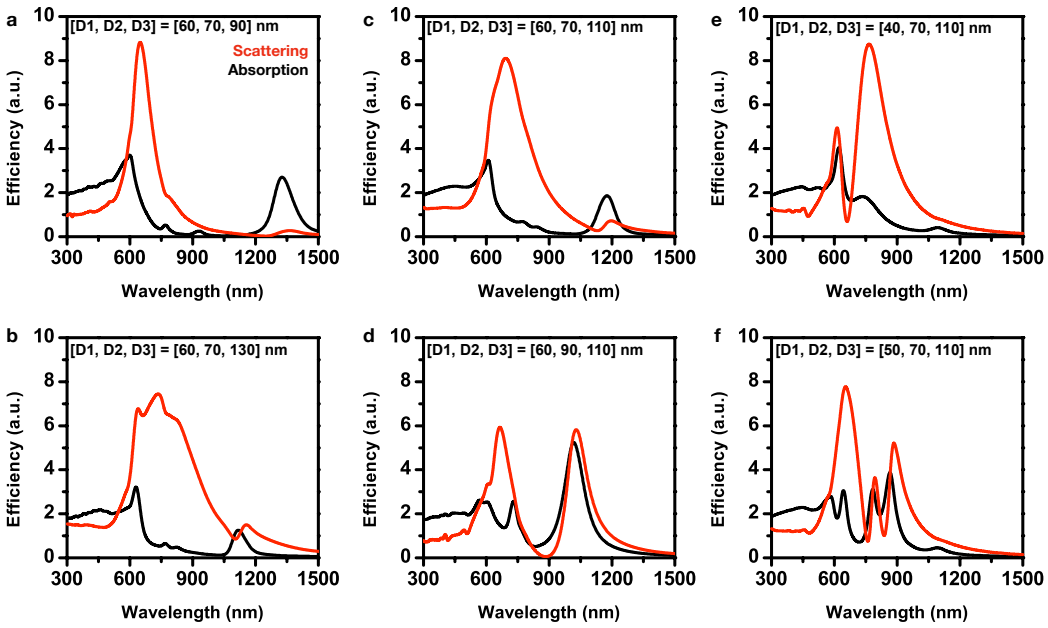

Figure 5.8: Absorption and scattering cross sections of fanocubes with (a,b) varying the Au shell size, (c,d) varying the SiO2 interlayer thickness, and (e,f) varying the Ag core size.

shell. Upon excitation with resonant light, metal nanostructures either scatter or absorb incident light or a combination of the two determined by the size and shape of the nanostructures. However, in three-layered concentric nanostructures, the absorption and scattering properties can be manipulated by modulating the separation between the two metal layers providing us with an additional degree of freedom to alter optical characteristics. These absorption and scattering proper- ties can then be harnessed for relevant technological applications. For example, in solar energy conversion and photovoltaics, highly scattering nanostructures will be advantageous, while in therapeutic applications where absorbed light needs to be converted to heat, highly absorptive nanostructures will be preferred. Here we calculated the absorption and scattering cross sections of the bimetallic fanocubes by varying both the dimensions of the Au shell (Figure 5.8a,b), thicknesses of the SiO_2 layer (Figure 5.8c,d), and size of the Ag core (Figure 5.8e,f). The bimetallic fanocubes with a thinner Au shell have strong absorption efficiency in the near-infrared overlapping with the second biological window, which will be highly relevant for photothermal therapies (Figure 5.8a). It is notable that the same geometry yields a strong scattering cross-section

in the visible region, which should be advantageous for plasmon-enhanced photovoltaics employing radiative enhancement. Conversely, fanocubes with thicker Au shells exhibit strong broadband scattering spanning the entire visible and near-infrared (Figure 5.8b), which can be harnessed for biosensing and biomedical imaging, as well as for radiative enhancement in solar devices. Further, the ratio of absorption to scattering can be drastically tuned in the bimetallic fanocubes by simply modulating the spacing between the Ag core and Au shell without altering the overall dimensions (Figure 5.8c,d). Whereas a thin silica layer of 5 nm (D_2 = 70 nm) gives rise to high scattering efficiency in the visible, a thicker silica layer of 15 nm (D_2 = 90 nm) results in equal contributions from absorption and scattering in the near-infrared (900-1100 nm). These calculations indicate that thinner SiO_2 interlayer (Figure 5.8c) results in a thicker Au shell, which weakens the coupling between the Ag core and Au shell and substantially suppresses the absorption efficiency. When the separation between the two metal layers is optimized to an ideal thickness of 15 nm (Figure 5.8d), a stronger coupling between the Ag and Au layers results in fanocubes, which will be highly useful for theranostic (therapeutic + diagnostic) applications where both scattering and absorption properties are necessary to combine imaging and therapy within a single platform.[66, 67] Modulating the dimensions of the Ag core also impacts its absorption and scattering properties. Whereas scattering is more dominant in the near-infrared for the smaller Ag core (Figure 5.8e), light scattering is more pronounced in the visible with the 50 nm Ag core size (Figure 5.8f). This shows that the scattering cross section can be significantly tuned in the fanocubes by altering the core size, facilitating their use in photovoltaics where the scattering cross section must be tuned to overlap with the absorber bandgap. However, note that scattering is also significantly suppressed at the Fano dip in all of the spectra shown in Figure 5.8 indicating that fanocubes when optimized to have strong Fano resonance can be highly useful in sensing applications where suppressed scattering and strong absorption are desirable.

Fano resonances in concentric nanostructures can also be tuned by breaking symmetry,

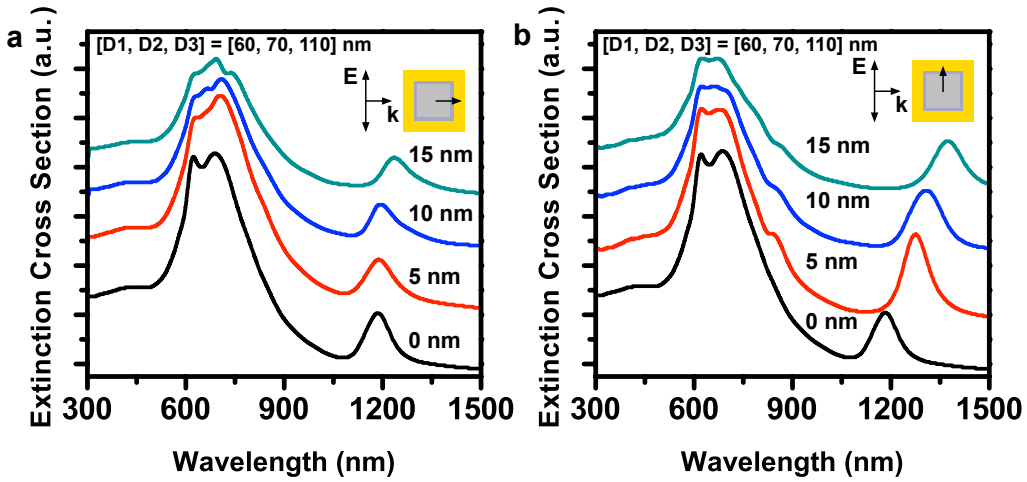

Figure 5.9: Symmetry breaking in bimetallic fanocube shown by offsetting the Ag core in the (a) transverse direction and (b) longitudinal direction with respect to the incoming plane wave. The distance the core offsets from the center is indicated in each spectrum.

which is achieved by offsetting the core with respect to the shell.[21, 26, 28] Whereas in concentric spherical nanostructures, the core offset in any direction yields the same spectral characteristics; in bimetallic fanocubes the cubic geometry allows core offset in either the transverse or longitudinal direction, resulting in distinct spectral shifts and Fano behavior. To investigate the effect of symmetry breaking, we simulated the extinction spectra of fanocubes by offsetting the Ag core with the SiO_2 layer together both in the transverse (Figure 5.9a) and longitudinal direction (Figure 5.9b) with respect to the incoming plane wave. Increasing core-offset in the fanocubes in both the transverse and longitudinal direction resulted in red-shift of the 1172 nm infrared Fano peak; however, stronger spectral shift was observable in the longitudinal direction. Notably the asymmetric line shape of this Fano peak was retained with core-offset in the transverse direction, but in the longitudinal direction, a loss of Fano characteristic to a simple dipolar mode was observed with increasing core-offset. Further, with increasing core-offset, the visible Fano resonance at 615 nm dissipates in both transverse and longitudinal directions; however, new Fano resonances emerge that are distinct in each direction. A weak Fano dip emerges at 700 nm when the Ag/SiO_2 core offsets by 10 nm in the transverse direction, which further

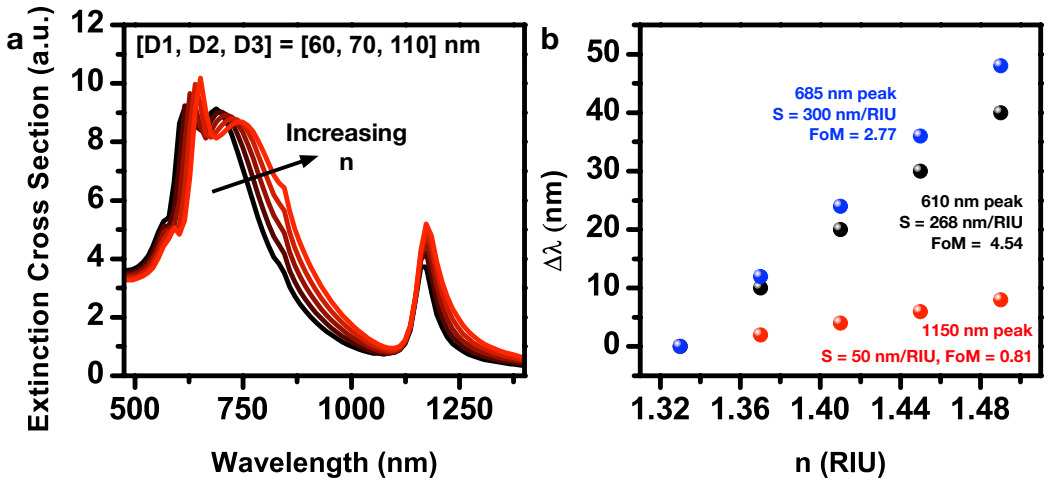

Figure 5.10: Refractive index sensing with bimetallic fanocubes. (a) Spectral shift in the extinction of fanocubes [D1, D2, D3] = [60, 70, 110] nm with increasing refractive index (RI) of surrounding medium indicated with an arrow. (b) Spectral shifts as a function of refractive index from 1.33 to 1.49 for three different peaks of the fanocubes. The sensitivity of each peak is indicated in the legend.

red-shifts with increasing symmetry-breaking (Figure 5.9a). A Fano resonance also appears at 825 nm when the core offsets by 5 nm in the longitudinal direction and red-shifts with increasing symmetry breaking. The reduced symmetry of the fanocubes with noncon-centric alignment of the Ag/SiO_2 core with the Au shell results in higher order modes to hybridize with the dipolar modes, which strongly enhances their brightness and results in their appearance in the extinction spectrum. This effect has been experimentally observed previously in the $Au/SiO_2/Au$ simple nanomatryoshka.[21, 28] Our results clearly indicate that symmetry breaking in bimetallic fanocubes can be systematically controlled by tuning both the degree of metal core-offset relative to the outer metal shell, and the direction of the core-offset.

Fano resonances in plasmonic nanostructures have been extensively harnessed for ultrasensitive biosensing enabled by their strongly dispersive character, which gives rise to the observed line width narrowing.[60, 61, 62, 68, 69] Engineered nanostructures with strong Fano resonances allow high quality factor plasmonic sensors, which exhibit significant spectral shifts to even small perturbations within their local environment. We have

therefore calculated the refractive index sensitivity (S)of bimetallic fanocubes of dimensions [D_1, D_2, D_3] = [60, 70, 110] nm by varying the refractive index of the surrounding medium from 1.331.49 for three different peaks (Figure 5.10). The narrow mode at 610 nm has S = 268 nm/RIU, the broad mode at 685 nm has S = 300 nm/RIU, and the infrared Fano peak at 1150 nm has S = 50 nm/RIU. While sensitivity is widely accepted as a metric for assessing the performance of a sensor, often ideal conditions are assumed when determining sensitivity experimentally such as negligible system noise and infinitely high spectral resolution. Therefore, the figure of merit (FOM), which is defined as sensitivity divided by the full width at half-maximum (fwhm) of the plasmon peak, is considered a more meaningful parameter for evaluating the performance of sensors. We calculated the FOM of each of these peaks at n = 1.33; the 610 nm peak has FOM = 2.77, the 685 nm peak has FOM = 4.54, and the 1150 nm peak has FOM = 0.81. While our FOM and S are lower than that reported for lithographically fabricated submicron plasmonic sensors supporting Fano resonances,[63, 69] they are comparable or higher than other wet-chemically synthesized nanostructures.[70, 71, 72, 73] However, we anticipate the sensitivity and FOM of fanocubes will likely decrease in experiments relative to the simulated results due to heterogeneities in synthesized nanostructures. In addition to the ability of fanocubes to monitor refractive index changes in the surrounding media, they also have the capability to directionally scatter light, a phenomenon highly useful for applications in color routing,[74] Yagi-Uda nano-antennas,[75, 76] and for solar light capture.[77]

We calculated the angular scattering intensity for [D_1,D_2,D_3] = [60, 70, 110] nm bimetallic fanocubes in aqueous media using a total-field scattered-field source, where the incident field is decoupled from the total field to determine far-field scattering intensity. The angular scattering direction in the XY and YZ direction is schematically represented in Figure 5.11a, where 0 $^\circ$ indicates the forward direction and 180 $^\circ$ indicates the backward direction in the planes normal to the incident field. For clarity, the scattering profiles in the planes normal to the incident light are shown here (Figure 5.11b,c); the parallel (XZ) plane

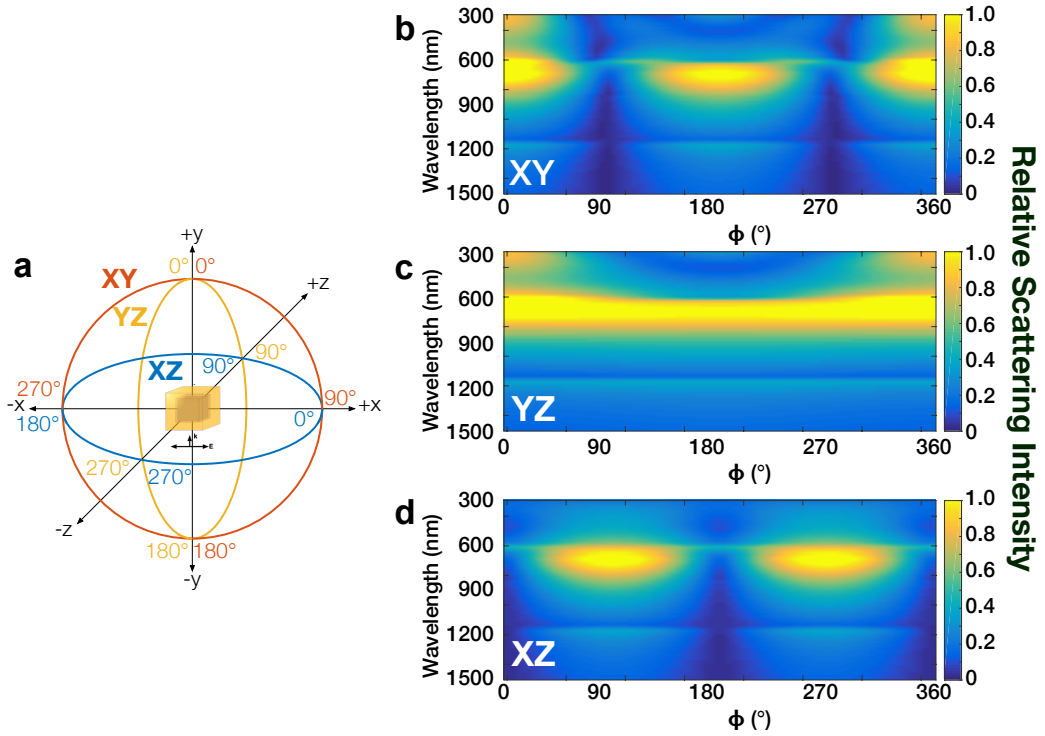

Figure 5.11: (a) Schematic representation of the orientation of the fanocube relative to incident electric field and scattering plane. Angular scattering intensity as a function of angle and wavelength in the (b) XY, (c) YZ and (d) XZ planes for bimetallic fanocubes.

is shown in Figure 5.11d. While scattering in the XZ plane remains symmetric through the spectrum, it is evident that fanocubes display directional scattering in the XY and YZ planes. In the wavelength range of 300-600 nm, preferential scattering occurs in the forward direction (Figure 5.11b,d), whereas in the range of 600-1200 nm, directional scattering is observed in the backward direction (Figure 5.11b,e). The ability to directionally scatter light is attributable to an internal phase shift approaching 180 $^{\circ}$ in overlapping dipolar elements within the fanocube,[74] whereas directional scattering in plasmonic nanostructures is typically achieved by both spectral tuning of the LSPR as well as spatial tuning of optical antennas which often require precise fabrication conditions. Here we demonstrate that the bimetallic material composition of fanocubes provides a new avenue to manipulate the phase of incoming light, which can potentially function as an optical color router.

5.4 Conclusions

In summary, in this work we present a theoretical investigation of a new concentric Fano resonant nanostructure, bimetallic fanocubes, with a Ag nanocube core separated from Au cubic nanoshell with a silica dielectric interlayer. The plasmon hybridization model of this complex structure reveals that in the nonbonding mode, which is typically dark in concentric spherical Au/SiO_2/Au nanostructures, in bimetallic fanocubes, the coupling between Ag and Au and strong contributions from the edges and corners significantly enhance this nonbonding peak. Our simulations show that bimetallic nanocubes generate multiple Fano resonances spanning the visible and near-infrared, which are tunable by altering the dimensions of the outer Au shell, Ag core, the thickness of the SiO_2 interlayer, and by symmetry breaking achieved by nonconcentric alignment of the core and shell. By examining the spectral shifts in bimetallic fanocubes with change in the refractive index of the surrounding media, our calculations also demonstrate high sensing performance with sensitivities and figure of merit comparable or higher than other nanostructures of similar size regime. Further, we also show wavelength-dependent directional light scattering

ability of the fanocubes, which can be optimized for specific applications such as photonic color routers as well as coupling to a substrate for solar light harvesting.

5.5 Bibliography

[1] Harry A. Atwater and Albert Polman. Plasmonics for improved photovoltaic devices. *Nat. Mater.*, 9(3):205–13, 2010.

[2] William R. Erwin, Andrew Coppola, Holly F. Zarick, Poorva Arora, Kevin J. Miller, and Rizia Bardhan. Plasmon enhanced water splitting mediated by hybrid bimetallic Au-Ag core-shell nanostructures. *Nanoscale*, 6:12626–12634, 2014.

[3] William R. Erwin, Holly Zarick, Eric M. Talbert, and Rizia Bardhan. Light Trapping in Mesoporous Solar Cells with Plasmonic Nanostructures. *Energy Environ. Sci.*, 9:1577–1601, 2016.

[4] Qiaoqiang Gan, Filbert J. Bartoli, and Zakya H. Kafafi. Plasmonic-enhanced organic photovoltaics: breaking the 10% efficiency barrier. *Adv. Mater.*, 25(17):2385–2396, 2013.

[5] Michael Saliba, Wei Zhang, Victor M. Burlakov, Samuel D. Stranks, Yao Sun, James M. Ball, Michael B. Johnston, Alain Goriely, Ulrich Wiesner, and Henry J. Snaith. Plasmonic-Induced Photon Recycling in Metal Halide Perovskite Solar Cells. *Adv. Funct. Mater.*, 25(31):5038–5046, 2015.

[6] Holly F. Zarick, William R. Erwin, Abdelaziz Boulesbaa, Olivia K. Hurd, Joseph A. Webb, Alexander A. Puretzky, David B. Geohegan, and Rizia Bardhan. Improving Light Harvesting in Dye Sensitized Solar Cells using Hybrid Bimetallic Nanostructures. *ACS Photonics*, 3(3):385–394, 2016.

[7] Holly F. Zarick, Olivia Hurd, Joseph A. Webb, Chanse Hungerford, William R. Erwin, and Rizia Bardhan. Enhanced Efficiency in Dye-Sensitized Solar Cells with Shape-Controlled Plasmonic Nanostructures. *ACS Photonics*, 1(9):806–811, 2014.

[8] Joseph A. Webb and Rizia Bardhan. Emerging advances in nanomedicine with engineered gold nanostructures. *Nanoscale*, 6(5):2502–30, 2014.

[9] Nardine S. Abadeer and Catherine J. Murphy. Recent Progress in Cancer Thermal Therapy Using Gold Nanoparticles. *J. Phys. Chem. C*, 120(9):4691–4716, 2016.

[10] Erik C. Dreaden, Alaaldin M. Alkilany, Xiaohua Huang, Catherine J. Murphy, and Mostafa A. El-Sayed. The golden age: gold nanoparticles for biomedicine. *Chem. Soc. Rev.*, 41(7):2740, 2012.

[11] Lev Dykman and Nikolai Khlebtsov. Gold nanoparticles in biomedical applications: recent advances and perspectives. *Chem. Soc. Rev.*, 41(6):2256–2282, 2012.

[12] Yu-chuan Ou, Joseph A. Webb, Shannon Faley, Daniel Shae, Eric M. Talbert, Sharon Lin, Camden C. Cutright, John T. Wilson, Leon M. Bellan, and Rizia Bardhan. Gold Nanoantenna-Mediated Photothermal Drug Delivery from Thermosensitive Liposomes in Breast Cancer. *ACS Omega*, 1:234–243, 2016.

[13] Kathryn M. Mayer and Jason H. Hafner. Localized surface plasmon resonance sensors. *Chem. Rev.*, 111(6):3828–57, 2011.

[14] Krishnendu Saha, Sarit S. Agasti, Chaekyu Kim, Xiaoning Li, and Vincent M. Rotello. Gold nanoparticles in chemical and biological sensing. *Chem. Rev.*, 112(5):2739–2779, 2012.

[15] Joseph A. Webb, Jayde Aufrecht, Chanse Hungerford, and Rizia Bardhan. Ultrasensitive analyte detection with plasmonic paper dipsticks and swabs integrated with branched nanoantennas. *J. Mater. Chem. C*, 2(48):10446–10454, 2014.

[16] Shuwen Zeng, Dominique Baillargeat, Ho-Pui Ho, and Ken-Tye Yong. Nanomaterials enhanced surface plasmon resonance for biological and chemical sensing applications. *Chem. Soc. Rev.*, 43(10):3426–52, 2014.

[17] C. Radloff and N. J. Halas. Plasmonic properties of concentric nano-shell. *Nano Lett.*, 4:1323–1327, 2004.

[18] E. Prodan, C. Radloff, N J. Halas, and P. Nordlander. A hybridization model for the plasmon response of complex nanostructures. *Science*, 302(5644):419–22, 2003.

[19] Ying Hu, Ryan C. Fleming, and Rebekah A. Drezek. Optical properties of gold-silica-gold multilayer nanoshells. *Opt. Express*, 16(24):19579–19591, 2008.

[20] Rizia Bardhan, Shaunak Mukherjee, Nikolay A. Mirin, Stephen D. Levit, Peter Nordlander, and Naomi J. Halas. Nanosphere-in-a-Nanoshell: A Simple Nanomatryushka. *J. Phys. Chem. C*, 114(16):7378–7383, 2010.

[21] Ying Hu, Sterling J. Noelck, and Rebekah A. Drezek. Symmetry Breaking in Gold-Silica-Gold Multipayer Nanoshells. *ACS Nano*, 4(3):1521–1528, 2010.

[22] Shaunak Mukherjee, Heidar Sobhani, J. Britt Lassiter, Rizia Bardhan, Peter Nordlander, and Naomi J. Halas. Fanoshells: Nanoparticles with built-in Fano resonances. *Nano Lett.*, 10(7):2694–2701, 2010.

[23] Zhu Jian, Li Jian-jun, and Zhao Jun-wu. Tuning the Dipolar Plasmon Hybridization of Multishell Metal-Dielectric Nanostructure: Gold Nanosphere in a Gold Nanoshell. *Plasmonics*, 6(3):527–534, 2011.

[24] Meng Wang, Min Cao, Xin Chen, and Ning Gu. Subradiant Plasmon Modes in Multilayer Metal-Dielectric Nanoshells. *J. Phys. Chem. C*, 115:20920–20925, 2011.

[25] Ovidio Peña Rodríguez, Antonio Rivera, Mariano Campoy-Quiles, and Umapada Pal. Tunable Fano resonance in symmetric multilayered gold nanoshells. *Nanoscale*, 5:209–216, 2012.

[26] Jin Fa Ho, Boris Luk'yanchuk, and Jing Bo Zhang. Tunable Fano resonances in silver-silica-silver multilayer nanoshells. *Appl. Phys. A Mater. Sci. Process.*, 107(1):133–137, 2012.

[27] Jian Zhu, Jian-jun Li, Lin Yuan, and Jun-wu Zhao. Optimization of Three-Layered Au Ag Bimetallic Nanoshells for Triple-Bands Surface Plasmon Resonance. *J. Phys. Chem. C*, 116:11734–11740, 2012.

[28] Jun Qian, Zongqiang Chen, Wudeng Wang, Yudong Li, Jingjun Xu, and Qian Sun. Dual Symmetry Breaking in Gold-Silica-Gold Multilayer Nanoshells. *Plasmonics*, 9(6):1361–1369, 2014.

[29] Li Lin, Mario Zapata, Min Xiong, Zhonghui Liu, Shanshan Wang, Hong Xu, Andrei G. Borisov, Hongchen Gu, Peter Nordlander, Javier Aizpurua, and Jian Ye. Nanooptics of Plasmonic Nanomatryoshkas: Shrinking the Size of a Core-Shell Junction to Subnanometer. *Nano Lett.*, 15(10):6419–6428, 2015.

[30] Jian Zhu, Jian jun Li, and Jun wu Zhao. Obtain Quadruple Intense Plasmonic Resonances from Multilayered Gold Nanoshells by Silver Coating: Application in Multiplex Sensing. *Plasmonics*, 8(3):1493–1499, 2013.

[31] Jian Zhu, Ying Juan Ren, Shu Min Zhao, and Jun Wu Zhao. The effect of inserted gold nanosphere on the local field enhancement of gold nanoshell. *Mater. Chem. Phys.*, 133(2-3):1060–1065, 2012.

[32] Adnan Daud Khan. Enhanced plasmonic Fano-like resonances in multilayered nanoellipsoid. *Appl. Phys. A Mater. Sci. Process.*, 122(4):300, 2016.

[33] Adnan Daud Khan, Muhammad Amin, Muhammad Yasir Iqbal, Amjad Ali, Rehan-Ullah U. Khan, and Sultan Daud Khan. Twin Dipole Fano Resonances in Symmetric Three-Layered Plasmonic Nanocylinder. *Plasmonics*, 10(4):963–970, 2015.

[34] Hongxing Xu. Multilayered metal core-shell nanostructures for inducing a large and tunable local optical field. *Phys. Rev. B*, 72(7):73405, 2005.

[35] Xiaohua Xia, Yang Liu, Vadim Backman, and Guillermo A. Ameer. Engineering sub-100 nm multi-layer nanoshells. *Nanotechnology*, 17(21):5435–5440, 2006.

[36] Yongping Gao, Yongsheng Li, Yao Wang, Yi Chen, Jinlou Gu, Wenru Zhao, Jian Ding, and Jianlin Shi. Controlled synthesis of multilayered gold nanoshells for enhanced photothermal therapy and SERS detection. *Small*, 11(1):77–83, 2015.

[37] Vikram Kulkarni, Emil Prodan, and Peter Nordlander. Quantum plasmonics: Optical properties of a nanomatryushka. *Nano Lett.*, 13(12):5873–5879, 2013.

[38] Jun Qian, Yudong Li, Jing Chen, Jingjun Xu, and Qian Sun. Localized hybrid plasmon modes reversion in gold-silica-gold multilayer nanoshells. *J. Phys. Chem. C*, 118(16):8581–8587, 2014.

[39] Shaoyan Gao, Pengbo Li, and Fuli Li. Geometrical parameters controlled focusing and enhancing near field in infinite circular metal-dielectric multilayered cylinder. *Appl. Phys. Lett.*, 102(12):123107, 2013.

[40] Adnan Daud Khan and Giovanni Miano. Higher Order Tunable Fano Resonances in Multilayer Nanocones. *Plasmonics*, 8(2):1023–1034, 2013.

[41] J. Qian, Y. D. Sun, Y. D. Li, J. J. Xu, and Q. Sun. Nanosphere-in-a-nanoegg: damping the high-order modes induced by symmetry breaking. *Nanoscale Res. Lett.*, 10:17, 2015.

[42] Jun Qian, Wudeng Wang, Yudong Li, Jingjun Xu, and Qian Sun. Optical extinction properties of perforated gold-silica-gold multilayer nanoshells. *J. Phys. Chem. C*, 116(18):10349–10355, 2012.

[43] Benjamin Gallinet and Olivier J. F. Martin. Ab initio theory of Fano resonances in plasmonic nanostructures and metamaterials. *Phys. Rev. B - Condens. Matter Mater. Phys.*, 83(23):1–6, 2011.

[44] Yong S. Joe, Arkady M. Satanin, and Chang Sub Kim. Classical analogy of Fano resonances. *Phys. Scr.*, 74(2):259, 2006.

[45] Boris Luk'yanchuk, Nikolay I. Zheludev, Stefan A. Maier, Naomi J. Halas, Peter Nordlander, Harald Giessen, and Chong Tow Chong. The Fano resonance in plasmonic nanostructures and metamaterials. *Nat. Mater.*, 9(9):707–15, 2010.

[46] Andrey E. Miroshnichenko, Sergej Flach, and Yuri S. Kivshar. Fano resonances in nanoscale structures. *Rev. Mod. Phys.*, 82(3):2257–2298, 2010.

[47] Wei Shun Chang, J. Britt Lassiter, Pattanawit Swanglap, Heidar Sobhani, Saumyakanti Khatua, Peter Nordlander, Naomi J. Halas, and Stephan Link. A plasmonic Fano switch. *Nano Lett.*, 12(9):4977–4982, 2012.

[48] Jonathan A. Fan, Chihhui Wu, Kui Bao, Jiming Bao, Rizia Bardhan, Naomi J. Halas, Vinothan N. Manoharan, Peter Nordlander, Gennady Shvets, and Federico Capasso. Self-assembled plasmonic nanoparticle clusters. *Science*, 328(5982):1135–1138, 2010.

[49] Jonathan A. Fan, Kui Bao, Chihhui Wu, Jiming Bao, Rizia Bardhan, Naomi J. Halas, Vinothan N. Manoharan, Gennady Shvets, Peter Nordlander, and Federico Capasso. Fano-like interference in self-assembled plasmonic quadrumer clusters. *Nano Lett.*, 10(11):4680–4685, 2010.

[50] Mario Hentschel, Daniel Dregely, Ralf Vogelgesang, Harald Giessen, and Na Liu. Plasmonic oligomers: The role of individual particles in collective behavior. *ACS Nano*, 5(3):2042–2050, 2011.

[51] Mario Hentschel, Martin Schäferling, Thomas Weiss, Na Liu, and Harald Giessen. Three-dimensional chiral plasmonic oligomers. *Nano Lett.*, 12(5):2542–2547, 2012.

[52] J. Britt Lassiter, Heidar Sobhani, Mark W. Knight, Witold S. Mielczarek, Peter Nordlander, and Naomi J. Halas. Designing and deconstructing the fano lineshape in plasmonic nanoclusters. *Nano Lett.*, 12(2):1058–1062, 2012.

[53] Feng Hao, Peter Nordlander, Yannick Sonnefraud, Pol Van Dorpe, and Stefan A. Maier. Tunability of subradiant dipolar and fano-type plasmon resonances in metallic ring/disk cavities: Implications for nanoscale optical sensing. *ACS Nano*, 3(3):643–652, 2009.

[54] Feng Hao, Yannick Sonnefraud, Pol Van Dorpe, Stefan A. Maier, Naomi J. Halas, and Peter Nordlander. Symmetry breaking in plasmonic nanocavities: Subradiant LSPR sensing and a tunable Fano resonance. *Nano Lett.*, 8(11):3983–3988, 2008.

[55] Yuan Hsing Fu, Jing Bo Zhang, Ye Feng Yu, and Boris Luk'Yanchuk. Generating and manipulating higher order Fano resonances in dual-disk ring plasmonic nanostructures. *ACS Nano*, 6(6):5130–5137, 2012.

[56] Niels Verellen, Yannick Sonnefraud, Heidar Sobhani, Feng Hao, V. Moshchalkov, Pol Van Dorpe, Peter Nordlander, Stefan A. Maier, Victor V. Moshchalkov, Pol Van Dorpe, and Peter Nordlander. Fano Resonances in Individual Coherent Plasmonic Nanocavities. *Nano Lett.*, 9(4):1663–1667, 2009.

[57] Shunping Zhang, Kui Bao, Naomi J. Halas, Hongxing Xu, and Peter Nordlander. Substrate-induced Fano resonances of a plasmonic nanocube: A route to increased-sensitivity localized surface plasmon resonance sensors revealed. *Nano Lett.*, 11(4):1657–1663, 2011.

[58] Huanjun Chen, Lei Shao, Tian Ming, Kat Choi Woo, Yat Cho Man, Jianfang Wang, and Hai-Qing Lin. Observation of the Fano Resonance in Gold Nanorods Supported on High-Dielectric constant substrates. *ACS Nano*, 5(8):6754–6763, 2011.

[59] Ciceron Ayala-Orozco, Jun G. Liu, Mark W. Knight, Yumin Wang, Jared K. Day, Peter Nordlander, and Naomi J. Halas. Fluorescence enhancement of molecules inside a gold nanomatryoshka. *Nano Lett.*, 14(5):2926–2933, 2014.

[60] Arif E. Cetin and Hatice Altug. Fano resonant ring/disk plasmonic nanocavities on conducting substrates for advanced biosensing. *ACS Nano*, 6(11):9989–9995, 2012.

[61] Anil K. Kodali, Xavier Llora, and Rohit Bhargava. Optimally designed nanolayered metal-dielectric particles as probes for massively multiplexed and ultrasensitive molecular assays. *Proc. Natl. Acad. Sci.*, 107(31):13620–5, 2010.

[62] Anil K. Kodali, Matthew V. Schulmerich, Rohun Palekar, Xavier Llora, and Rohit Bhargava. Optimized nanospherical layered alternating metal-dielectric probes for optical sensing. *Opt. Express*, 18(22):23302–13, 2010.

[63] Fernando Lopez-Tejeira, Ramon Paniagua-Domnguez, and Jose A. Sanchez-Gil. High-Performance Nanosensors Based on Plasmonic Fano-like Interference: Probing Refractive Index with Individual Nanorice and Nanobelts. *ACS Nano*, 6(10):8989–8996, 2012.

[64] Ciceron Ayala-Orozco, Cordula Urban, Mark W. Knight, Alexander Skyrme Urban, Oara Neumann, Sandra W. Bishnoi, Shaunak Mukherjee, Amanda M. Goodman, Heather Charron, Tamika Mitchell, Martin Shea, Ronita Roy, Sarmistha Nanda, Rachel Schiff, Naomi J. Halas, and Amit Joshi. Au nanomatryoshkas as efficient near-infrared photothermal transducers for cancer treatment: Benchmarking against nanoshells. *ACS Nano*, 8(6):6372–6381, 2014.

[65] Arash Ahmadivand and Nezih Pala. Analyzing Photothermal Heat Generation Efficiency in a Molecular Plasmonic Silver Nanomatryushka Dimer. *Plasmonics*, 11(2):493–501, 2016.

[66] Wenxue Chen, Ciceron Ayala-Orozco, Nrusingh C. Biswal, Carlos Perez-Torres, Marc Bartels, Rizia Bardhan, Gary Stinnet, Xian-De Liu, Baoan Ji, and Amit Deorukhkar. Targeting pancreatic cancer with magneto-fluorescent theranostic gold nanoshells. *Nanomedicine*, 9(8):1209–1222, 2014.

[67] Mi-Ran Choi, Rizia Bardhan, Katie J. Stanton-Maxey, Sunil Badve, Harikrishna Nakshatri, Keith M. Stantz, Ning Cao, Naomi J. Halas, and Susan E. Clare. Delivery of nanoparticles to brain metastases of breast cancer using a cellular Trojan horse. *Cancer Nanotechnol.*, 3(1-6):47–54, 2012.

[68] Chihhui Wu, Alexander B. Khanikaev, Ronen Adato, Nihal Arju, Ahmet Ali Yanik, Hatice Altug, and Gennady Shvets. Fano-resonant asymmetric metamaterials for ultrasensitive spectroscopy and identification of molecular monolayers. *Nat. Mater.*, 11(1):69–75, 2011.

[69] Ahmet Ali Yanik, Arif E. Cetin, Min Huang, Alp Artar, S. Hossein Mousavi, Alexander Khanikaev, John Connor, Gennady Shvets, and Hatice Altug. Ultrasensitive plasmonic fano sensor enables seeing protein monolayers with naked eye. *Proc. Natl. Acad. Sci.*, 108(29):425–426, 2011.

[70] Yuriy Khalavka, Jan Becker, and Carsten Sonnichsen. Synthesis of rod-shaped gold nanorattles with improved plasmon sensitivity and catalytic activity. *J. Am. Chem. Soc.*, 131(5):1871–1875, 2009.

[71] Joseph A. Webb, William R. Erwin, Holly F. Zarick, Jayde Aufrecht, Harris W. Manning, Matthew J. Lang, Cary L. Pint, and Rizia Bardhan. Geometry-Dependent Plasmonic Tunability and Photothermal Characteristics of Multibranched Gold Nanoantennas. *J. Phys. Chem. C*, 118(7):3696–3707, 2014.

[72] Huanjun Chen, Lei Shao, Kat Choi Woo, Tian Ming, Hai-Qing Lin, and Jianfang Wang. Shape-dependent refractive index sensitivities of gold nanocrystals with the same plasmon resonance wavelength. *J. Phys. Chem. C*, 113(41):17691–17697, 2009.

[73] Silvia Barbosa, Amit Agrawal, Laura Rodriguez-Lorenzo, Isabel Pastoriza-Santos, Ramón A. Alvarez-Puebla, Andreas Kornowski, Horst Weller, and Luis M. Liz-Marzán. Tuning size and sensing properties in colloidal gold nanostars. *Langmuir*, 26(18):14943–14950, 2010.

[74] Timur Shegai, Si Chen, Vladimir D. Miljković, Gülis Zengin, Peter Johansson, and Mikael Käll. A bimetallic nanoantenna for directional colour routing. *Nat. Commun.*, 2:481, 2011.

[75] Ivan S. Maksymov, Andrey E. Miroshnichenko, and Yuri S. Kivshar. Actively tunable bistable optical Yagi-Uda nanoantenna Abstract :. *Opt. Express*, 20(8):2819–2824, 2012.

[76] Daniel Dregely, Richard Taubert, Jens Dorfmüller, Ralf Vogelgesang, Klaus Kern, and Harald Giessen. 3D optical Yagi-Uda nanoantenna array. *Nat. Commun.*, 2:267, 2011.

[77] P. Spinelli, C. Van Lare, E. Verhagen, and A. Polman. Controlling Fano lineshapes in plasmon-mediated light coupling into a substrate. *Opt. Express*, 19:303–311, 2011.

Chapter 6

APPROACHES TO IMPROVEMENT TO LIGHT CAPTURE TECHNOLOGY BEYOND PLASMONICS: CARBON PASSIVATED POROUS SILICON AS A COUNTER ELECTRODE IN DYE-SENSITIZED SOLAR CELLS

6.1 Summary

In this chapter, we explore improvements to photoelectrochemical systems beyond efficiency improvement utilizing plasmonics. We demonstrate the use of porous silicon (P-Si) as counter electrodes in dye-sensitized solar cells (DSSCs) with efficiencies (5.38%) comparable to that achieved with platinum counter electrodes (5.80%). To activate the P-Si for triiodide reduction, few layer carbon passivation is utilized to enable electrochemical stability of the silicon surface. The success of our method largely results from the high surface area platform provided by the porous silicon substrate. Our results suggest porous silicon as a promising sustainable and manufacturable alternative to rare metals for electrochemical solar cells, following appropriate surface modification.

6.2 Introduction

Dye-sensitized solar cells (DSSCs) have emerged as a promising third generation solar cell due to efficiencies so far measured up to 12% [1, 2, 3, 4, 5, 6] and straightforward processes for solar cell manufacturing. A conventional DSSC functions based upon an anode interface between TiO_2 and dye molecules yielding dye photooxidation and charge transfer to an iodide/triiodide (I^-/I_3^-) redox couple under illumination. The redox couple is regenerated using a metal counter electrode. Platinum is used as the counter electrode due to its corrosion resistance to iodide species and its excellent electrocatalytic activity toward the iodide/triiodide redox couple.[7, 8, 9] However, evolution toward DSSCs that can be

cheaply manufactured with low-cost, sustainable materials provides a key incentive toward the development and widespread commercialization of DSSCs. [10]

In recent years, numerous reports have demonstrated the ability to utilize alternative counter-electrode materials for DSSCs with performance approaching Pt. This primarily involves the utilization of carbon nanotubes,[11, 12, 13] graphene,[11, 12, 13, 14, 15, 16] hybrid carbon nanotube-graphene materials, [17, 18] and other carbon nanostructures. [19, 20] Whereas such approaches yield excellent promise for the use of all-carbon counter-electrodes to replace Pt, cell-level integration of such materials are not aided by the high raw-materials cost of carbon nanostructures, which can often be greater than Pt (e.g. $>$\$100/gram), and the requirement to process such raw materials into usable architectures for electrodes that can add significant manufacturing-related costs. Other materials, such as Fe_2O_3 and TiN nanostructures, polymer films, and Cu-Zn-Sn-S have been demonstrated as effective counter-electrodes, [21, 22, 23, 24] even though challenges regarding stability, efficiency, and conduction properties can be compromised in such alternative systems.

We propose in this study that silicon is a viable candidate for DSSC electrodes. As the manufacturing of silicon materials is central to electronics and photovoltaics industries, large-scale processing of silicon is cost-effective in comparison to other material options where expensive process development routes are necessary. Furthermore, due to its earth abundance, metallurgical grade silicon materials, which are practical for such applications due to their lower purity requirements than electronics, can be obtained at \$2-5/kg. Based purely on raw materials cost, this provides over a $1000\times$ reduction over Pt if silicon could be a viable electrode material. Whereas the total cost of a DSSC is based on the combined materials and manufacturing costs, silicon is a unique alternative that is promising in both of these areas. Nonetheless, silicon is a material with surface properties strongly influenced by environmental factors, and is highly reactive with ambient air or electrochemical conditions. As a result, in industrial-scale applications where silicon is employed, a critical factor enabling usability is the controlled chemical passivation of exposed silicon surfaces

- an area of research which has thrived over the past few decades.[25] In the particular case of porous silicon (P-Si) materials produced from bulk silicon by electrochemical etching, such routes are especially important due to the significantly enhanced exposed surface area that could potentially provide more catalytically active sites for the I_3^-/I^- redox reaction as a DSSC electrode. [25] A variety of routes to passivate the P-Si surface have been described, which can mostly be characterized as involving a Si-O or Si-C surface termination.[26, 27] Whereas such routes have been utilized extensively in chemical or biological sensing,[28] controlled surface passivation of P-Si remains unexplored for applications in electrochemical energy conversion platforms. In this work, we specifically utilize a thermal route to passivate P-Si materials with few-layered coatings of carbon to provide an electrochemically stable DSSC electrode that exhibits performance comparable to Pt. We emphasize the importance of complete silicon surface passivation to enable optimized device performance, and the function of a 3D porous material to optimize the redox activity. As thermally-induced carbon passivation is one of many potential surface stabilization chemistries for silicon, we emphasize silicon as a manufacturable, low-materials cost, and chemically versatile platform for scalable surface modification and replacement of rare metals conventionally employed as DSSC electrodes.

6.3 Results and Discussion

Thermal passivation of P-Si materials was achieved consistent with our previous studies,[29] and building from efforts by Salonen et al.[30, 31] This involves exposure of P-Si to an environment containing a diluted C_2H_2 active species ($<0.1\%$) in H_2/Ar. In order to achieve full passivation and maintain structural integrity of the P-Si nanoscale features, we observed the passivation temperature to be important. Prolonged exposure to temperatures greater than 750 °C led to irreversible structural changes to the P-Si, which were alleviated by introducing temperature ramps from below 750 °C to temperatures above this, as the formation of a thin carbon coating passivated the surface from thermal degradation at high

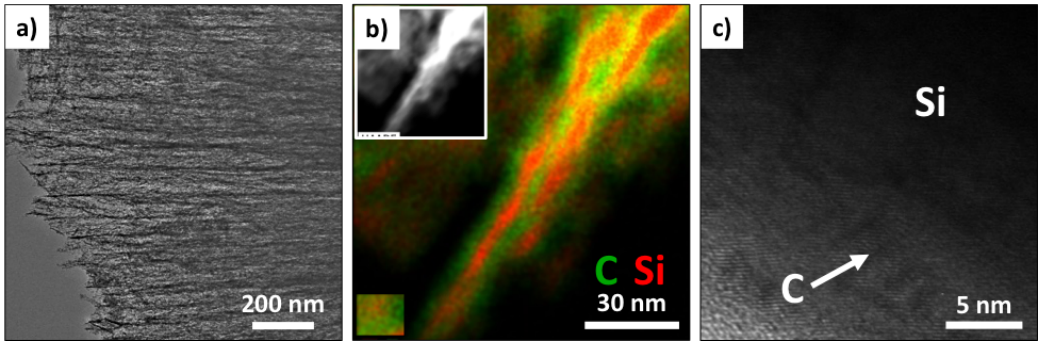

Figure 6.1: (a) Low resolution TEM image of carbon coated porous silicon. (b) Energy dispersive spectroscopy map of carbon coated porous silicon with a HAADF STEM image in the inset. (c) High resolution TEM image of few layer graphene on silicon surface.

temperatures. As discussed at a later point, our most ideal temperature ramp condition was obtained between 650-800 °C, which enabled complete catalytic surface passivation without thermal decomposition of the C_2H_2 species that was found to yield low-quality carbon materials. Whereas we chose thermal passivation for our work, progress in silicon surface passivation using wet chemical approaches, such as surface alkylation [32, 33], could ultimately enable a similar outcome to the results we discuss here.

The morphology of the carbon coated porous silicon is shown via low resolution TEM (Figure 6.1a). In order to confirm and assess the presence of carbon on the silicon surface after thermal passivation, a high angle annular dark field (HAADF) image was obtained with energy-dispersive x-ray (EDS) mapping of carbon and silicon (Figure 6.1b), the corresponding spectrum is shown in Figure 6.2). A high resolution TEM image showing the carbon-silicon interface and presence of few-layer carbon coatings is presented in Figure 6.1c. To assess the carbon material properties, fast Fourier transform analysis was used to determine the interlayer spacing, which was found to be between 0.35 and 0.37 nm (Figure 6.3). This spacing represents a graphene material with interlayer defects; it is greater than pristine defect-free graphene (~0.34 nm) [34, 35] but lower than most forms of chemically processed graphene, such as reduced graphene oxide (often >0.4 nm) [36]. Therefore, we emphasize under these conditions that the thermal surface passivation of P-Si leads to a

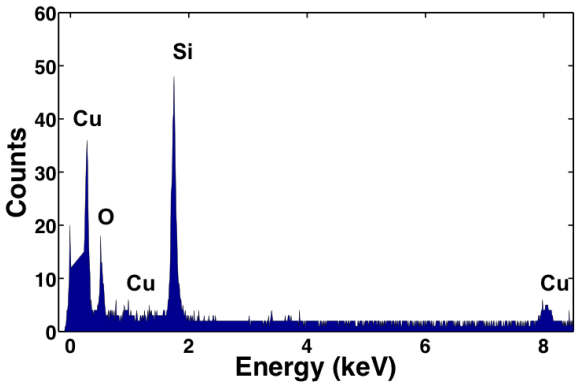

Figure 6.2: EDS spectrum corresponding to Figure 6.1b. This spectrum is an area average of an EDS mapped image. The carbon and silicon signals arise from the material being imaged, the copper signal originates from the TEM grid.

uniform, few-nm thick coating of conformal graphene layers catalyzed by the nanoscale silicon material.

DSSCs with C-passivated porous silicon counter electrodes were designed by depositing a TiO_2 active layer adsorbed with Di-tetrabutylammonium cis-bis(isothiocyanato)bis(2,2-bipyridyl-4,4-dicarboxylato)ruthenium(II) (N719) dye on the fluorine tin oxide (FTO) glass followed by a TiO_2 scattering layer. A liquid electrolyte consisting of I^-/I_3^- redox couple was utilized for electron transport between the electrodes. A schematic representation of a typical DSSC made with C-passivated porous silicon is illustrated in Figure 6.4a and the front and back view counter electrode is shown in Figure 6.4b.

The characteristics of the P-Si surface passivation are observed to directly correlate with DSSC performance. In order to study the effect of C-passivation on the catalytic properties of porous silicon, DSSCs were fabricated with pristine P-Si and thermal passivation at three different temperature ramp profiles including 550-700 °C, 650-800 °C, and 750-900 °C. The C-passivation layer was characterized by acquiring Raman spectra for all four samples (Figure 6.5a). Pristine P-Si has a single strong peak near 520 cm^{-1}, indicative of silicon. After thermal passivation, two distinctive peaks arise at 1325 cm^{-1} (D-band) and 1602 cm^{-1} (G-band) that are characteristic of graphitic carbon coatings.[37] The D/G peak height is indicative of the ratio of sp^3 to sp^2 hybridized carbon species, which is notably

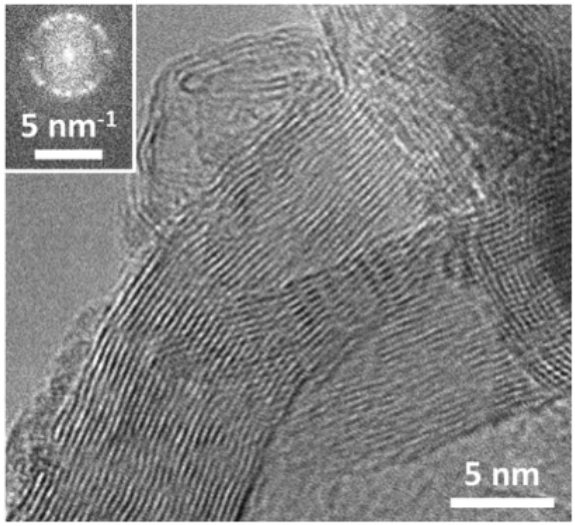

Figure 6.3: TEM and FFT of graphene oxide with d-spacing of 0.35-0.36 nm.

consistent at D:G = 0.76 until the highest temperature conditions (750-900 °C), where D:G is 1.22. We attribute this to a decrease in crystallinity of the C-passivation layer associated with higher temperature non-catalytic decomposition of C_2H_2 species. Notably, we do not observe the presence of a significant oxide layer on the silicon, which is evident in the Raman spectra through a bump near 800 cm^{-1}.

To better understand the properties of C-passivation, we measured conductance through the P-Si layer in the different C-passivated P-Si materials. It is known that P-Si materials exhibit defect induced surface traps that can reverse the effect of chemical doping and decrease the P-Si conductance by several orders of magnitude.[38] Measurements were carried out by sandwiching porous silicon electrodes between two plates connected with copper wires, and performing I-V curves. This forces the porous silicon layer to be a resistive component in series with the bulk silicon, enabling us to assess the effect of surface passivation on the porous silicon electrical properties. We find the conductance to increase between 3-5 orders of magnitude through C-passivation, calculated over the Ohmic region from current-voltage scans shown in Figure 6.5b. This observation is complimented by two additional observations, *(i)* post C-passivation Si etch experiments in KOH led to small, polydispersed flakes at 550-700 °C and coherent films at 650-800 °C (Figure 6.6), and *(ii)*

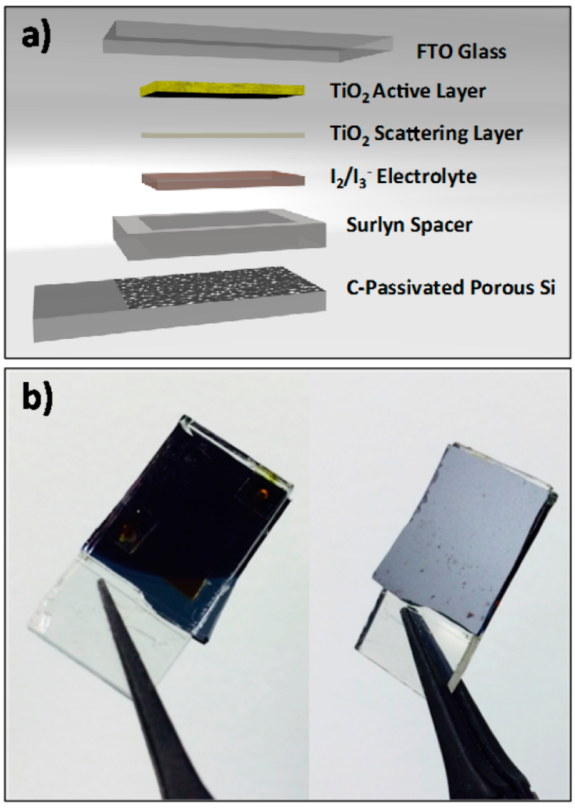

Figure 6.4: (a) Schematic of dye sensitized solar cells fabricated with C-passivated porous silicon counter electrode. (b) Front (left) and back (right) view of DSSC with C-passivated porous silicon counter electrode.

TEM imaging of C-passivated regions did not show a distinct layer thickness dependence between the different C-passivation temperatures. We do not anticipate that the formation of an oxide layer would affect this result since we observe no presence of an oxide layer in these materials (Raman and TEM analysis), and any effect of an oxide layer on the conductivity would be consistent across all samples. This leads us to conclude that *(i)* ramp conditions with terminal temperatures below 700 °C lead to incomplete surface passivation, in turn leading to exposed Si surface, *(ii)* ramp conditions from 650-800 °C lead to ideal surface passivation, and *(iii)* terminal temperatures in ramp conditions of 900 °C and above lead to thicker, less crystalline carbon passivation layers (Figure 6.5c).

DSSCs were constructed with the C-passivated porous silicon fabricated at the three conditions and compared to reference DSSCs constructed with standard Pt counter electrodes. Photocurrent spectra of DSSCs under AM 1.5 illumination are shown in Figure 6.7a. The short circuit current density (J_{sc}), open circuit voltage (V_{oc}), calculated efficiency, and fill factor (FF) are summarized in Table 1. DSSCs with a P-Si counter electrode exhibited an efficiency of 0.21 % relative to an efficiency of 5.80 % for the platinized FTO counter electrodes, which we can attribute to either the poor electrochemical stability native to unpassivated silicon that drives corrosion, the lack of conductivity (Figure 6.5b), or the lack of catalytically active sites for triiodide reduction that are developed through surface modification. DSSCs made with 650-800 °C C-passivated P-Si exhibited efficiency of 5.38 %, which is comparable to solar cells constructed using Pt counter electrodes. Comparatively, DSSCs constructed with C-passivation conditions of 550-700 °C and 750-900 °C exhibited efficiencies of 2.13 % and 3.95 % respectively. This indicates C-passivation at temperatures of 650-800 °C leads to ideal performance that seems to correlate with previous material charge-transport analysis shown in Figure 6.5. We also note that DSSCs fabricated with C-passivation at 750-900 °C had a relatively good efficiency and fill factor compared to P-Si and those constructed at 550-700 °C. This can be attributed to the full coverage and passivation of porous silicon by carbon which minimizes the charge recom-

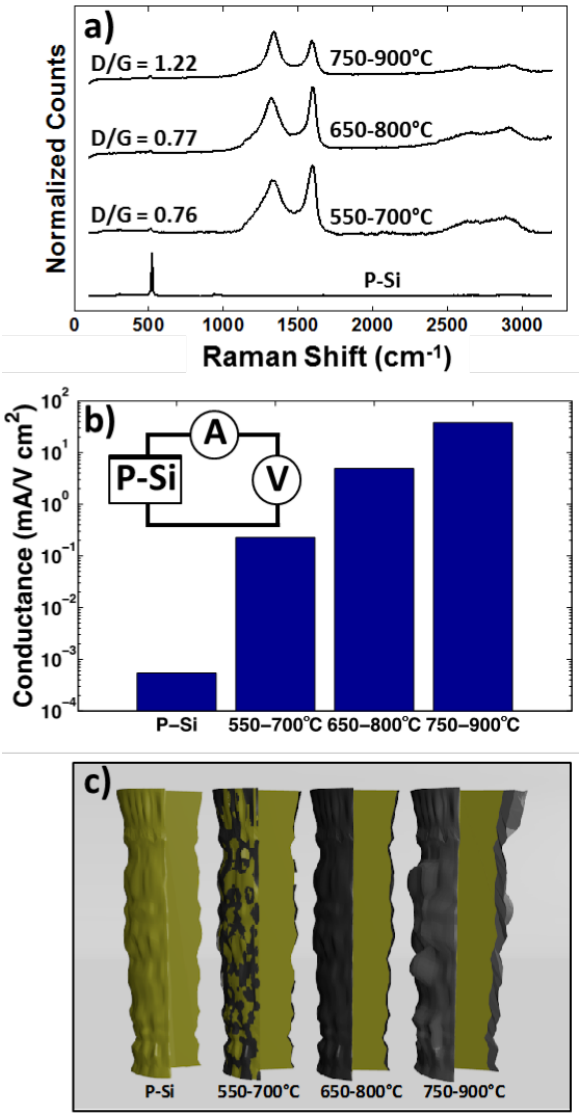

Figure 6.5: (a) Raman spectra of pristine porous silicon and porous silicon C-passivated at different temperatures, peaks are normalized to the 1602 cm-1 G-peak. (b) Calculated conductance values for porous silicon and C-passivated porous silicon at different temperatures with inset schematic of through plane measurement setup. (c) Schematic representation of carbon coating (black) on a section of porous silicon (yellow) for each sample type. The coating coverage and thickness were determined using data from cyclic voltammetry, electrochemical impedance spectroscopy and through plane conductivity. The structure on the right is shaded differently to indicate the higher ratio of sp^3 to sp^2 carbon.

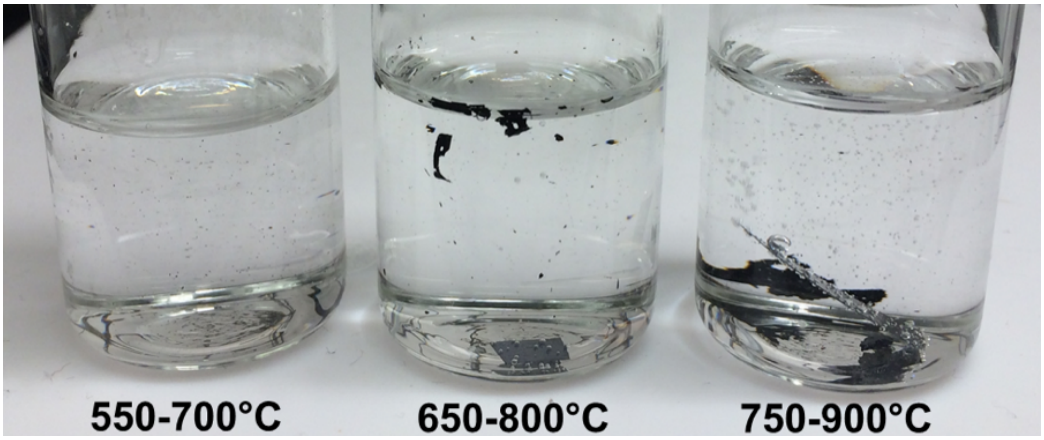

Figure 6.6: An image of the carbon coating when silicon has been dissolved away via KOH etching. C-passivated P-Si at 550-700 °C has no visible carbon while those passivated at 650-800 °C has some visible pieces of carbon and C-passivated P-Si at 750-900 °C has one large piece of carbon that did not break apart..

bination on the surface and lowers the charge transfer resistance. Long-term illumination studies of the passivated P-Si counter electrodes in comparison to Pt (SI, Figure S7) emphasize the ability for the passivation layer to enable long-term operation of this electrode material.

To understand these inherent differences in performance, the C-passivated P-Si counter electrodes were characterized with electrochemical impedance spectroscopy (EIS), and cyclic voltammetry. EIS was performed on symmetric counter electrode cells over a frequency range of 10-1-105 Hz in order to investigate the charge transfer properties in the system (Figure 6.7b). The first semicircle is representative of the charge transfer resistance and double layer capacitance at the cathode. The second, low frequency semicircle is indicative of electrolyte diffusion between electrodes. The observed differences in the impedance between the DSSCs constructed with Pt counter electrode and the C-passivated P-Si at 650-800 °C (Figure 6.7b) is attributed to a combination of *(i)* higher resistance to electron transfer, stemming from the insulating porous silicon interface between the carbon coating and conductive silicon substrate, and *(ii)* slower ionic diffusion likely due to the poor reduction of triiodide species at the C-passivated P-Si relative to the planar Pt. To

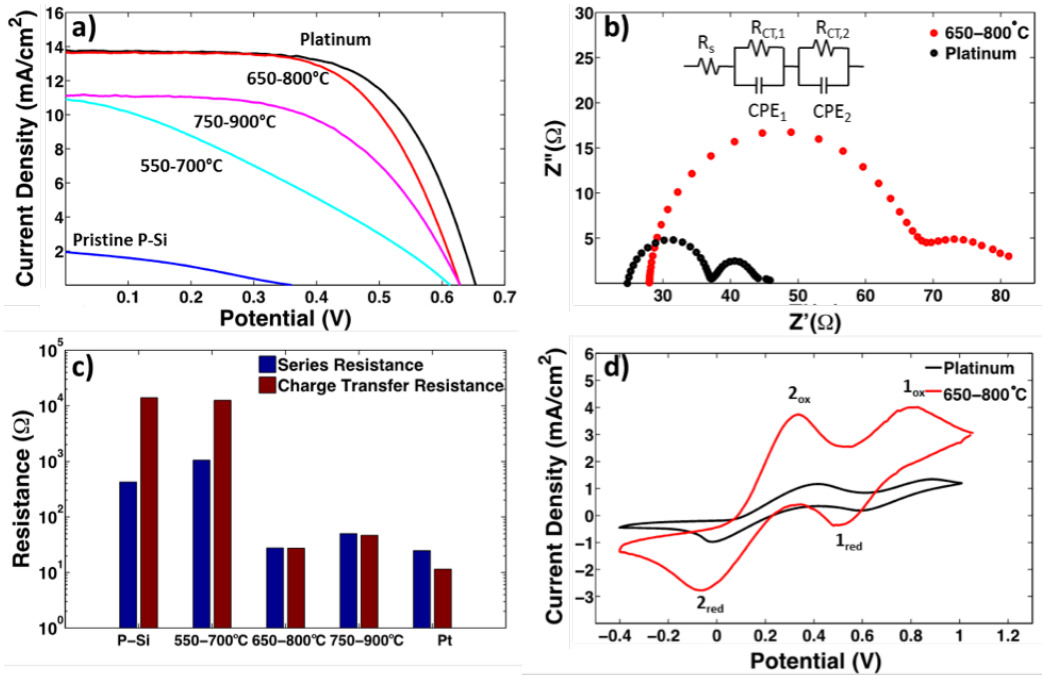

Figure 6.7: (a) J-V curves of DSSCs designed with the C-passivated porous silicon fabricated at different temperatures under AM 1.5 G illumination. The J-V curve of the Pt counter electrode is included as well. (b) Nyquist plots of symmetric cells made from carbon coated porous silicon and platinum under zero voltage bias over a frequency range of 10^{-1} to 10^{5} Hz with equivalent circuit diagram provided (inset). Here CPE refers to constant phase element, R_{ct} refers to charge transfer resistance, and R_s refers to series resistance. (c) Calculated series and charge transfer resistances of different counter electrodes measured over identical P-Si sample areas of 0.12 cm^2. (d) Cyclic voltammograms of carbon coated porous silicon fabricated at 650 °800 °C and Pt. Reaction 1 refers to $3I_2 + 2e^- \longrightarrow 2I_3^-$ and reaction 2 refers to $I_3^- + 2e^- \longrightarrow 3I^-$, the latter occurring at the counter electrode.

further elucidate these mechanisms, an appropriate equivalent circuit model was fit to the system [39] provided in the inset of Figure 6.7b. Series (R_s) and charge transfer (R_{ct}) resistances were calculated from the circuit model shown in Figure 6.7c. The model reveals that the series and charge transfer resistances of both pristine P-Si and C-passivated P-Si thermally treated at 550-700 °C are orders of magnitude higher than the corresponding resistances of samples treated at 650-800 °C, 750-900 °C, and Pt. The magnitude of the resistances found with P-Si and the 550-700 °C sample is attributed to corrosion occurring on exposed Si surface.[32, 33] Series resistance varies with C-passivation thickness,[36, 37] and is lowest for the platinum sample, and increases for the 650-800 °C sample and 750-900 °C sample.[40, 41] It should be noted that this is qualitatively in agreement with through-plane conductivity measurements (Figure 6.5b), even though this value of Rs is more relevant to the electrode-limited resistance of the full device with the porous silicon-electrolyte interface. The lower R_{ct} of Pt is a result of less recombination at the cathode relative to C-passivated P-Si, and hence slightly faster kinetics of triiodide reduction that is indicative of an efficient counter electrode material. The 750-900 °C treated P-Si sample has a higher R_{ct} than the 650-800 °C treated samples due to its reduced ability for triiodide reduction - a result of its highly defective carbon coating. These effects enhance the interfacial charge transfer events, lower the overall resistance, and augment the efficiencies and fill factor. Nyquist plots of only Pt counter electrodes and C-passivated P-Si thermally treated at 650-800 °C are shown in Figure 6.7b. In order to further understand the electrochemical properties of the different C-passivated porous silicon samples, cyclic voltammetry (CV) measurements were carried out in a three electrode setup. The CV curve of the Pt counter electrode (Figure 6.7d) is similar to that found in the literature.[42] Two sets of peaks were observed corresponding to the reduction of iodine to triiodide given by redox reactions 6.1 and reduction of triiodide to iodide ions given by reaction 6.2,

$$3\,I_2 + 2\,e^- \longrightarrow 2\,I_3^- \tag{6.1}$$

$$I_3^- + 2\,e^- \longrightarrow 3\,I^- \tag{6.2}$$

The separation of the reduction and oxidation peaks, Epp, is indicative of the electrochemical catalytic activity of the counter electrodes which is independent of their surface area.[14, 42] Values for E_{pp} of 0.40 and 0.43 V were found for the samples passivated at 650-800 °C and Pt, respectively, which indicates that the catalytic ability of C-passivated P-Si for the I^-/I_3^- redox couple is on par with Pt. Porous-Si samples passivated at 750-900 °C exhibited an E_{pp} value of 0.54, indicating that the surface passivation at the higher temperatures is not as effective of a catalyst, due to the high defect ratio.[43] Due to the high surface area of porous silicon, the redox peaks are much larger for the C-passivated P-Si than for the planar Pt, which explains the comparable efficiencies of the DSSCs. CV measurements of both P-Si and the C-passivated samples at 550-700 °C (Figure 6.8) show their poor catalytic activity for I^-/I_3^- oxidation reaction. The incomplete passivation achieved at 550-700 °C likely gives rise to high charge recombination on the exposed Si and inadequate redox chemistries resulting in low efficiencies and poor fill factor. We note that we also performed a control experiment using planar silicon as a counter electrode for DSSC (Figure 6.9) and did not observe a measurable photocurrent.

Overall, whereas we emphasize in this work that passivated Si materials are viable candidates for the replacement of Pt in DSSCs, our results indicate a synergistic co-dependence of the passivation layer and silicon material properties that dictate overall behavior. In regimes of incomplete passivation, poor device performance is indicative of poor charge-transport properties and a high R_{ct} that inhibits redox activity. However, in regimes of complete passivation with poor quality coatings, inefficient redox activity inhibits performance matching Pt reference cells. The benefit of silicon in such a material platform is the tun-

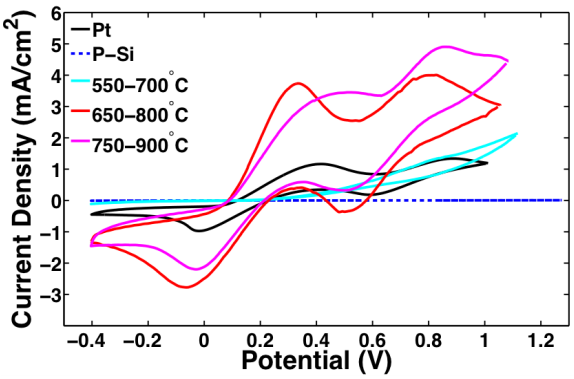

Figure 6.8: Cyclic voltammograms of all samples carried out in a three electrode setup using nitrogen bubbled acetonitrile which contained 0.1 M LiClO4, 10 mM LiI and 1 mM I2 as an electrolyte over a potential range of 1 to -0.8 V. Metallic platinum was used as the counter electrode and Ag/AgCl reference electrode was used

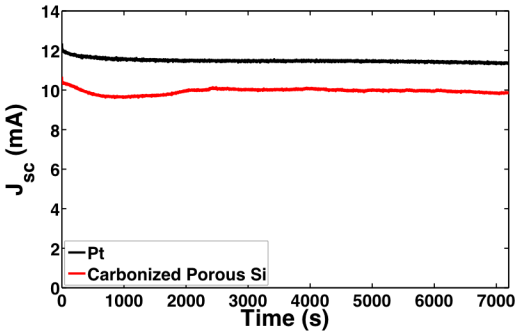

Figure 6.9: Stability tests of DSSCs with Pt and C-passivated P-Si counter electrodes over two hours. Results indicate that porous silicon stability is comparable to Pt on the observed timescale

able surface chemistry between the silicon and carbon that can enable optimal performance as a counter electrode in a DSSC. Whereas we demonstrate this to be a viable platform that can be utilized in the context of an on-chip system, we emphasize the versatility of this technique to scale to a diverse scope of microscale and nanoscale silicon heterogeneous materials that can provide a new, sustainable alternative material for efficient DSSC fabrication. In comparison to other solar energy conversion systems using silicon, where processing and interface optimization are necessary to enable efficient device performance, we demonstrate heterogeneous porous silicon materials that natively exhibit the capability to be electrodes for DSSCs with appropriate surface modification.

6.4 Conclusions

While our specific work is focused on thermally applied carbon passivation layers resembling graphene, the use of silicon reflects a versatile chemical platform for optimizing the electrode-electrolyte interface in a DSSC using scalable routes such as wet-chemical, thermal, and electrochemical passivation. Compared to other homogenous materials employed as counter electrodes in DSSCs, this approach represents the utilization of a heterogeneous material interface that we propose provides enhanced flexibility in achieving scalable device optimization. As silicon exists in nearly all applications as a heterogenous material in some form, and these applications represent the majority of our current technological infrastructure, we see this approach as directly building upon a material platform already-integrated into scalable industrial manufacturing processes. Furthermore, as DSSCs involve a native low-cost cell design with promise for versatility and cost that could ultimately replace silicon photovoltaics, we emphasize the fascinating notion of silicon to empower such a transition for DSSCs. As raw material costs of silicon are only a minor portion of commercial PV costs, the low-cost assembly of Si-based DSSCs to replace conventional PV platforms could build upon, instead of compete with, aggressive worldwide government-corporate investments aimed to improve upon silicon manufacturing for solar

applications.

6.5 Methods

TiO_2 Anode Preparation. Anodes were fabricated by first drilling holes in FTO glass (MTI Corp.). FTO glass slides were then sonicated in successive baths of isopropanol/acetone with 1% Triton-X100 and isopropanol/acetone for 30 minutes each, respectively. Glass slides were then rinsed with isopropanol then acetone and dried with nitrogen. Glass slides were treated with 40 mM $TiCl_4$ in water for 30 min at 70 °C and then dried in air. A 10 micron thick layer of 20 nm TiO_2 nanoparticles (Dyesol Inc., MS002010) was applied via the doctor blade technique onto the FTO glass using one layer of scotch tape (3M) to control the thickness of the layer. TiO_2 coated anodes were annealed at 500 °C for 30 minutes in air followed by another 40 mM $TiCl_4$ treatment for 12 hours at 35 °C. This treatment is crucial to cell performance as a TiO_2 sol gel is formed and fills gaps in the mesoporous TiO_2 nanoparticle layer preventing recombination of e^-/h^+ pairs. A scattering layer comprised of 300 nm TiO_2 nanoparticles (Dyesol Inc., MS002260) is added on top of the active layer and annealed at 500 °C. Finally, anodes were immersed in 0.6 mM cis-bis(isothiocyanato) bis(2,2-bipyridyl-4,4-dicarboxylato)ruthenium(II) (N-719 Dye) in ethanol overnight (Sigma, 703206).

C-Passivation of Porous Silicon. Highly boron-doped (0.01-0.2 Ωcm) silicon wafers (University Wafer) were etched in an electrochemical cell using a spiral Pt counter electrode according to our previously published procedure.[29] A 180 second etch process was utilized with a current density of 45 mA/cm^2 in a 3:8 v/v HF (50% H_2O by volume) and ethanol solution. This produces porous silicon materials with ~75% porosity, confirmed by optical reflectrometry, and an average pore size just under 25 nm.[44] Porous silicon was stored under N_2 until carbonization. For C-passivation, a porous silicon wafer was placed into a tube furnace at room temperature and the furnace was evacuated to 2 mTorr. Next, 1000 sccm of Ar and 200 sccm of H_2 were introduced to the system and the furnace

was ramped to T_1. T_1 was equal to 550 °C, 650 °C and 750 °C for the three different C-passivated P-Si samples respectively. The purpose of the H_2 is to maintain a reducing environment that preserves the surface stability of the unpassivated porous silicon from oxidation. Acetylene was introduced and the temperature was ramped to T_1 + 100. Ten minutes after C_2H_2 introduction, the temperature was ramped to T_1+150 for 10 minutes. This process was chosen since our observations in preliminary experiments demonstrated *(i)* porous silicon is not thermally stable without passivation above 750 °C, *(ii)* carbon coating thermally stabilizes the porous silicon up to ~1000 °C or higher, and *(iii)* the best quality of carbon materials based on Raman spectroscopy analysis were formed in the temperature range between 550-850 °C. Therefore, these conditions are able to optimize both the reactivity of the silicon for coating, the quality of carbon material, and the preservation of the nanoscale structure of the porous silicon after treatment. Following the second 10 minute step, C_2H_2 flow was discontinued and the sample was allowed to cool to 50 °C in an Ar and H_2 atmosphere. Samples were stored in an N_2 atmosphere until use to prevent oxidation.

DSSC Fabrication. Platinum cathodes were prepared by brushing 25 mM H_2PtCl_6 (Sigma 254029) in isopropanol onto clean FTO glass substrates. Samples were then calcined at 450-C for one hour. The cathode and anode were heat sealed with surlyn film (McMaster Carr, 7622A41) and filled with the electrolyte comprised of 50 mM I_2, 500 mM LiI and 500 mM tertbuylpyridine (TBP) in acetonitrile, and heat sealed.

Electrochemical Testing. Dye sensitized solar cells were tested over a potential range of -1 to 1 V at a scan rate of 50 mV/s under AM 1.5 illumination (100 mW/cm^2) with a Newport solar simulator and power supply. An area of 0.12 cm^2 was illuminated, the remainder was covered with a shadow mask. Cyclic voltammetry measurements were carried out in a three electrode setup using nitrogen bubbled acetonitrile which contained 0.1 M $LiClO_4$, 10 mM LiI and 1 mM I_2 as an electrolyte over a potential range of 1 to -0.8 V. A Pt foil was used as the counter electrode, Ag/AgCl was used as a reference electrode. Electro-

chemical impedance spectroscopy measurements were performed over a frequency range of 10^{-1}-10^{5} Hz. A MetroOhm PGSTAT101 potentiostat was used for all electrochemical measurements.

Material Characterization. An FEI Osiris TEM was used with an accelerating voltage of 200 kV for all TEM imaging. Raman spectra were gathered using a 532 nm DPSS laser in which the output power was limited to 10% (maximum output power and 50mW). The Raman scattered photons were dispersed by a 1200 lines/mm grating monochromator and collected by a CCD camera with a 50$\times$ objective lens.

6.6 Bibliography

[1] A. Yella, H. W. Lee, H. N. Tsao, C. Yi, A. K. Chandiran, M. K. Nazeeruddin, E. W. D. Diau, C. Y. Yeh, S. M. Zakeeruddin, and M. Grätzel. Porphyrin-Sensitized Solar Cells with Cobalt (II/III)Based Redox Electrolyte Exceed 12 Percent Efficiency. *Science*, 334:629–634, 2011.

[2] Aravind Kumar Chandiran, Nicolas Tetreault, Robin Humphry-baker, Florian Kessler, Etienne Barano, Chenyi Yi, Mohammad Khaja Nazeeruddin, Michael Gra, Khaja Nazeeruddin, Michael Grätzel, Etienne Baranoff, Chenyi Yi, Mohammad Khaja Nazeeruddin, and Michael Grätzel. Sub-nanometer Ga2O3 tunnelling layer by atomic layer deposition to achieve 1.1V open-circuit potential in dye-sensitized solar cells. *Nano Lett.*, 12(8):3941–, 2012.

[3] Nicolas Tétreault, Éric Arsenault, Leo Philipp Heiniger, Navid Soheilnia, Jérémie Brillet, Thomas Moehl, Shaik Zakeeruddin, Geoffrey A. Ozin, and Michael Grätzel. High-efficiency dye-sensitized solar cell with three-dimensional photoanode. *Nano Lett.*, 11(11):4579–4584, 2011.

[4] Tao Chen, Longbin Qiu, Zhenbo Cai, Feng Gong, Zhibin Yang, Zhongsheng Wang, and Huisheng Peng. Intertwined aligned carbon nanotube fiber based dye-sensitized solar cells. *Nano Lett.*, 12(5):2568–2572, 2012.

[5] Ladislav Kavan, Jun Ho Yum, and Michael Grätzel. Graphene nanoplatelets outperforming platinum as the electrocatalyst in co-bipyridine-mediated dye-sensitized solar cells. *Nano Lett.*, 11(12):5501–5506, 2011.

[6] Martin A. Green, Keith Emery, Yoshihiro Hishikawa, Wilhelm Warta, and Ewan D. Dunlop. Solar cell efficiency tables (version 48). *Prog. Photovoltaics Res. Appl.*, 24:905–913, 2016.

[7] Helmut Bonnemann, Guram Khelashvili, Silke Behrens, Andreas Hinsch, Krzysztof Skupien, and Eckhard Dinjus. Role of the platinum nanoclusters in the iodide/triiodide redox system of dye solar cells. *J. Clust. Sci.*, 18(1):141–155, 2007.

[8] Anneke Hauch and Andreas Georg. Diffusion in the electrolyte and charge-transfer reaction at the platinum electrode in dye-sensitized solar cells. *Electrochim. Acta*, 46(22):3457–3466, 2001.

[9] N. Papageorgiou. An Iodine/Triiodide Reduction Electrocatalyst for Aqueous and Organic Media. *J. Electrochem. Soc.*, 144(3):876, 1997.

[10] Jason B. Baxter. Commercialization of dye sensitized solar cells: Present status and future research needs to improve efficiency, stability, and manufacturing. *J. Vac. Sci. Technol. A Vacuum, Surfaces, Film.*, 30(2012):020801, 2012.

[11] Pei Dong, Cary L. Pint, Mel Hainey, Francesca Mirri, Yongjie Zhan, Jing Zhang, Matteo Pasquali, Robert H. Hauge, Rafael Verduzco, Mian Jiang, Hong Lin, and

Jun Lou. Vertically aligned single-walled carbon nanotubes as low-cost and high electrocatalytic counter electrode for dye-sensitized solar cells. *ACS Appl. Mater. Interfaces*, 3(8):3157–61, 2011.

[12] Jung Gyu Nam, Young Jun Park, Bum Sung Kim, and Jai Sung Lee. Enhancement of the efficiency of dye-sensitized solar cell by utilizing carbon nanotube counter electrode. *Scr. Mater.*, 62(3):148–150, 2010.

[13] Won Jae Lee, Easwaramoorthi Ramasamy, Dong Yoon Lee, and Jae Sung Song. Efficient dye-sensitized solar cells with catalytic multiwall carbon nanotube counter electrodes. *ACS Appl. Mater. Interfaces*, 1(6):1145–1149, 2009.

[14] Joseph D. Roy-Mayhew, David J. Bozym, Christian Punckt, and Ilhan A. Aksay. Functionalized Graphene as a Catalytic Solar Cells. *ACS Nano*, 4(10):6203–6211, 2010.

[15] Yuhua Xue, Jun Liu, Hao Chen, Ruigang Wang, Dingqiang Li, Jia Qu, and Liming Dai. Nitrogen-doped graphene foams as metal-free counter electrodes in high-performance dye-sensitized solar cells. *Angew. Chemie*, 51(48):12124–7, 2012.

[16] Ladislav Kavan, Jun Ho Yum, and Michael Gra. Optically Transparent Cathode for Dye- Nanoplatelets. *ACS Nano*, 5(1):165–172, 2011.

[17] Jie Ma, Lu Zhou, Cheng Li, Jinhu Yang, Tao Meng, Huiming Zhou, Mingxuan Yang, Fei Yu, and Junhong Chen. Surfactant-free synthesis of graphene-functionalized carbon nanotube film as a catalytic counter electrode in dye-sensitized solar cells. *J. Power Sources*, 247:999–1004, 2014.

[18] Josef Velten, Attila J. Mozer, Dan Li, David Officer, Gordon Wallace, Ray Baughman, and Anvar Zakhidov. Carbon nanotube/graphene nanocomposite as efficient counter electrodes in dye-sensitized solar cells. *Nanotechnology*, 23(8):085201, 2012.

[19] Tao Peng, Weiwei Sun, Xiaohua Sun, Niu Huang, Yumin Liu, Chenghao Bu, Shishang Guo, and Xing-Zhong Zhao. Direct tri-constituent co-assembly of highly ordered mesoporous carbon counter electrode for dye-sensitized solar cells. *Nanoscale*, 5(1):337–341, 2013.

[20] Takurou N. Murakami, Seigo Ito, Qing Wang, Md. Khaja Nazeeruddin, Takeru Bessho, Ilkay Cesar, Paul Liska, Robin Humphry-Baker, Pascal Comte, Peter Pechy, and Michael Gratzel. Highly Efficient Dye-Sensitized Solar Cells Based on Carbon Black Counter Electrodes. *J. Electrochem. Soc.*, 153(12):A2255, 2006.

[21] Yu Hou, Dong Wang, Xiao Hua Yang, Wen Qi Fang, Bo Zhang, Hai Feng Wang, Guan Zhong Lu, P. Hu, Hui Jun Zhao, and Hua Gui Yang. Rational screening low-cost counter electrodes for dye-sensitized solar cells. *Nat. Commun.*, 4:1583, 2013.

[22] Q. W. Jiang, G. R. Li, and X. P. Gao. Highly ordered TiN nanotube arrays as counter electrodes for dye-sensitized solar cells. *Chem. Commun.*, pages 6720–6722, 2009.

[23] Xukai Xin, Ming He, Wei Han, Jaehan Jung, and Zhiqun Lin. Low-cost copper zinc tin sulfide counter electrodes for high-efficiency dye-sensitized solar cells. *Angew. Chemie*, 50(49):11739–11742, 2011.

[24] Kun-Mu Lee, Po-Yen Chen, Chih-Yu Hsu, Jen-Hsien Huang, Wen-Hsien Ho, Hung-Chang Chen, and Kuo-Chuan Ho. A high-performance counter electrode based on poly(3,4-alkylenedioxythiophene) for dye-sensitized solar cells. *J. Power Sources*, 188(1):313–318, 2009.

[25] Neergaard Waltenburg and John Yates. Surface chemistry of silicon. *Chem. Rev.*, 95(5):1589–1673, 1995.

[26] Rolfe C. Anderson, Richard S. Muller, and Charles W. Tobias. Chemical Surface Modification of Porous Silicon. *J. Electrochem. Soc.*, 140(5):1396–1396, 1993.

[27] Jae Hee Song and Michael J. Sailor. Chemical Modification of Crystalline Porous Silicon Surfaces. *Comments Inorg. Chem.*, 21(1-3):69–84, 1999.

[28] Selena Chan, Yi Li, Lewis J. Rothberg, Benjamin L. Miller, and Philippe M. Fauchet. Nanoscale silicon microcavities for biosensing. *Mater. Sci. Eng. C*, 15(1-2):277–282, 2001.

[29] Landon Oakes, Andrew Westover, Jeremy W. Mares, Shahana Chatterjee, William R. Erwin, Rizia Bardhan, Sharon M. Weiss, and Cary L. Pint. Surface engineered porous silicon for stable, high performance electrochemical supercapacitors. *Sci. Rep.*, 3:3020, 2013.

[30] J. Salonen, E. Laine, and L. Niinistö. Thermal carbonization of porous silicon surface by acetylene. *J. Appl. Phys.*, 91(1):456–461, 2002.

[31] J. Salonen, V. P. Lehto, M. Björkqvist, E. Laine, and L. Niinistö. Studies of thermally-carbonized porous silicon surfaces. *Phys. Status Solidi Appl. Res.*, 182(1):123–126, 2000.

[32] Dhiraj Prasai, Juan Carlos Tuberquia, Robert R. Harl, G. Kane Jennings, and Kirill I. Bolotin. Graphene: Corrosion-inhibiting coating. *ACS Nano*, 6(2):1102–1108, 2012.

[33] R. K. Singh Raman, P. Chakraborty Banerjee, Derrek E. Lobo, Hemtej Gullapalli, Madusha Sumandasa, Ashwin Kumar, Lokesh Choudhary, Rachel Tkacz, Pulickel M. Ajayan, and Mainak Majumder. Protecting copper from electrochemical degradation by graphene coating. *Carbon N. Y.*, 50(11):4040–4045, 2012.

[34] Alfonso Reina, Xiaoting Jia, John Ho, Daniel Nezich, Hyungbin Son, Vladimir Bulovic, Mildred S. Dresselhaus, and Jing Kong. Large Area , Few-Layer Graphene Films on Arbitrary Substrates by Chemical Vapor Deposition. *Nano Lett.*, 9(1):30–35, 2009.

[35] Changgu Lee, Xiaoding Wei, Jeffrey W. Kysar, and James Hone. Measurement of the Elastic Properties and Intrinsic Strength of Monolayer Graphene. *Science*, 321:385–388, 2008.

[36] In Kyu Moon, Junghyun Lee, Rodney S. Ruoff, and Hyoyoung Lee. Reduced graphene oxide by chemical graphitization. *Nat. Commun.*, 1(6):73, 2010.

[37] A. C. Ferrari, J. C. Meyer, V. Scardaci, C. Casiraghi, M. Lazzeri, F. Mauri, S. Piscanec, D. Jiang, K. S. Novoselov, S. Roth, and A. K. Geim. Raman Spectrum of Graphene and Graphene Layers. *Phys. Rev. Lett.*, 97(18):187401, 2006.

[38] V. Lehmann, F. Hofmann, F. Moller, and U. Gruning. Resistivity of Porous Silicon: A Surface Effect. *Thin Solid Films*, 255(1-2):20–22, 1995.

[39] M. Liberatore, F. Decker, L. Burtone, V. Zardetto, T. M. Brown, A. Reale, and A. Di Carlo. Using EIS for diagnosis of dye-sensitized solar cells performance. *J. Appl. Electrochem.*, 39(11):2291–2295, 2009.

[40] Kiyoaki Imoto, Kohshin Takahashi, Takahiro Yamaguchi, Teruhisa Komura, Jun-ichi Nakamura, and Kazuhiko Murata. High-performance carbon counter electrode for dye-sensitized solar cells. *Sol. Energy Mater. Sol. Cells*, 79(4):459–469, 2003.

[41] Prakash Joshi, Yu Xie, Mike Ropp, David Galipeau, Shelia Bailey, and Qiquan Qiao. Dye-sensitized solar cells based on low cost nanoscale carbon/TiO2 composite counter electrode. *Energy Environ. Sci.*, 2(4):426, 2009.

[42] Mingxing Wu, Xiao Lin, Tonghua Wang, Jieshan Qiu, and Tingli Ma. Low-cost dye-sensitized solar cell based on nine kinds of carbon counter electrodes. *Energy Environ. Sci.*, 4(6):2308, 2011.

[43] Christian Punckt, Michael A. Pope, Jun Liu, Yuehe Lin, and Ilhan A. Aksay. Electrochemical Performance of Graphene as Effected by Electrode Porosity and Graphene Functionalization. *Electroanalysis*, 22(23):2834–2841, 2010.

[44] Girija Gaur, Dmitry S. Koktysh, and Sharon M. Weiss. Immobilization of quantum dots in nanostructured porous silicon films: Characterizations and signal amplification for dual-mode optical biosensing. *Adv. Funct. Mater.*, 23(29):3604–3614, 2013.

Chapter 7

SUMMARY AND OUTLOOK

In this work we investigated the use of shape controlled noble metal nanostructures for improvement to photovoltaic and photoelectrochemical light harvesting devices. This work provides key insights into the mechanisms which enable plasmon enhancement of light harvesting devices, and provides a guide for future enhancement schemes. Additionally, we used the expertise gained through our studies to pursue further advancements in light manipulation with shape controlled metal nanostructures, as well as alternative materials solutions for redox electrodes in dye-sensitized photoelectrochemical cells.

We achieved a 14$\times$ enhancement in external quantum efficiency of TiO_2 photoanodes, when comparing plasmon enhanced versus control photoanodes using bimetallic Au-Ag nanocrystals. Experiments and calculations have shown that the shape and composition of nanostructures play strong roles in the localized surface plasmon resonant enhancement of TiO_2 in water splitting systems; however, nanostructures in the ~80 nm size range are too large to accomplish the level of sensitization achievable by small (~1 nm) dye molecules such as N719. Future directions for plasmon enhancement of photoelectrochemical systems should exploit non-radiative effects by harnessing hot carrier injection in small ($<$30 nm) nanostructures. Additionally, plasmonic nanoparticles may provide a platform for enhancement in spectral regions unaccessible by commercially available dyes - essentially acting as a dual sensitizer system.

In OPV systems, strong near field enhancement plays a significant role in PCE improvement, up to 11%. Our experiments, supported by electrodynamic simulations indicate that PCE enhancement results from a distortion of the electric field in the active layer, rather than overall light absorption enhancement. Future experiments should focus on elucidation of the effect of non-radiative energy transfer in the nanoparticle enhanced OPV system via

ultrafast spectroscopy and modeling. The conclusions of our study can also be applied to a variety of OPV systems and are important to consider for any optoelectronic devices which are limited by charge transport.

Finally, the use of high surface area carbon coated porous silicon substrates as a redox electrode in dye sensitized solar cells enabled us to design a platinum-free photoelectrochemical device with only a 7% drop in PCE. It was found that defects in the carbon passivation layer actually played a large role in inducing catalytic activity. By using a similar high surface area passivated substrate, it is possible to improve the activity such that the PCE remains the same or is improved. This may be achieved by tailoring the activity of the carbon passivation layer by doping with nitrogen atoms.

The work herein has elucidated mechanisms and schemes for improvement of the efficiency and economic feasibility of light capture devices using plasmonic nanostructures among other innovative materials. The potential to apply these materials and methods to a variety of energy conversion devices is strong and moves us one step closer to realizing a future of renewable energy.

Appendix A

Chemical Synthesis of Nanostructures

A.1 Au Nanocube Synthesis

A.1.1 List of Materials

- 100 mM Hexadecyltrimethylammonium bromide (CTAB) (Sigma-Aldrich 855820) (547 mg + 15 mL H_2O)
- 10 mM Sodium borohydride (Sigma-Aldrich 8.18823) (38 mg + 10 mL H_2O) *freshly made, ice cold
- 10 mM Chloroauric acid (Sjgma-Aldrich 254169) (0.15 mL of 100 mM stock + 1.35 mL H_2O)
- 100 mM Ascorbic acid (Sigma-Aldrich A0278) (352 mg + 20 mL H_2O) *freshly made

A.1.2 Synthesis Protocol

1. **Mix Precursor Solution**
   To a 20 mL vial with small egg shaped stir bar add, 7.5 mL of 100 mM CTAB, 2.75 mL H_2O and 250 μL of 10 mM $HAuCl_4$. Mix together by inversion, then place in a 35 °C pre-heated H_2O bath for enough time to allow temperature to equilibrate in solution (Approximately 10 minutes).

2. **Prepare Au Seed Solution**
   While stirring vigorously, inject 600 μL of ice cold 10 mM $NaBH_4$, let stir for one minute. Transfer vial to 35 °C water bath and let sit for one hour. After one hour, remove solution and dilute 10:1 with Milli-Q water.

3. **Au Nanocube Synthesis**
   Measure 32 g of ultrapure water by weight into a 50 mL conical tube. To the 32 mL of water, add sequentially: 6.4 mL of 100 mM CTAB, 0.8 mL of 10 mM $HAuCl_4$ and 3.8 mL of 100 mM ascorbic acid, 20 μL of the 10x diluted seed solution. Mix with several gentle inversions, then place back in conical tube at 35 °C in water bath for five hours.

4. **Storage and Washing**
   Nanocrystals are coated with CTAB and are stable for up to 30 days when stored in the dark at 40 °C. In order to wash nanoparticles, CTAB in solution must be decrystallized by heating solution to 35 °C in a water bath. To wash, centrifuge at 1100 rcf and redisperse in water 3×.

A.2 Au@Ag Bimetallic Nanocrystal Synthesis

A.2.1 List of Materials

- 20 mM Hexadecyltrimethylammonium chloride (CTAC) (Sigma-Aldrich 52366) (384 mg CTAC + 120 mL H_2O)
- 10 mM Potassium bromide (Sigma-Aldrich 449962) (6 mg + 5 mL H_2O) *freshly made, ice cold
- 10 mM Silver nitrate (Sigma-Aldrich 209139) (5 mg + 3 mL H_2O)
- 100 mM Ascorbic acid (Sigma-Aldrich A0278) (35 mg + 2 mL H_2O) *freshly made
- AuNC seed (from previous section)

A.2.2 Synthesis Protocol

1. **Preparation of Au Seeds**
   Pre-heat water bath to 65 °C, decrystallize CTAB AuNCs, centrifuge 10 mL of AuNCs at 1100 RCF for 15 min. Remove supernatant and redisperse in 5 mL 20 mM CTAC; let sit for 15 minutes. Repeat centrifugation step twice, after the final centrifugation redisperse in 660 μL of MQ H_2O.

2. **Prepare growth solution**
   To a 50 mL centrifuge tube, add: 30 mL 20 mM CTAC, 1.2 mL concentrated AuNC seeds, 300 μL 10 mM KBr. Place in 65 °C water bath to equilibrate for 10 min.

3. **Begin Ag growth**
   Remove centrifuge tube from water bath and immediately add: 300 μL 10 mM $AgNO_3$ and 900 μL 100 mM Ascorbic Acid. Mix by inversion and place in 65 °C water bath for two hours.

4. **Storage and Washing**
   Nanocrystals are coated with CTAB and are stable for up to 30 days when stored in the dark at 40 °C. In order to wash nanoparticles, CTAB in solution must be decrystallized by heating solution to 35 °C in a water bath. To wash, centrifuge at 1100 rcf and redisperse in water 3×.

A.3 Au Nanosphere Synthesis

A.3.1 List of Materials

- 62.5 mg Potassium carbonate (Sigma Aldrich 791776)
- 3.75 mL 1wt.% Chloroauric acid (Sjgma-Aldrich 254169)
- 250 mL Milli-Q water
- 1.25 mL 37% formaldehyde (Sigma-Aldrich 252549)

1. **Potassium carbonate solution preparation**
   Add 0.25 L Milli-Q water, 62.5 mg potassium carbonate and 3.75 mL 1% Chloroauric acid ($HAuCl_4$) to a dark glass bottle and allow solution to age for 24-48 hours in the dark.

2. **Nanoparticle synthesis**
   Pour potassium carbonate/$HAuCl_4$ solution into a clear glass container and place a stir bar in the solution. Begin stirring at around 1000 rpm. Add 1.25 mL 37% formaldehyde. Wait until solution turns colors. First, it will turn a light purple, and progressively get darker as the particles grow in size. The synthesis is finished when particles have been scattering light for two minutes.

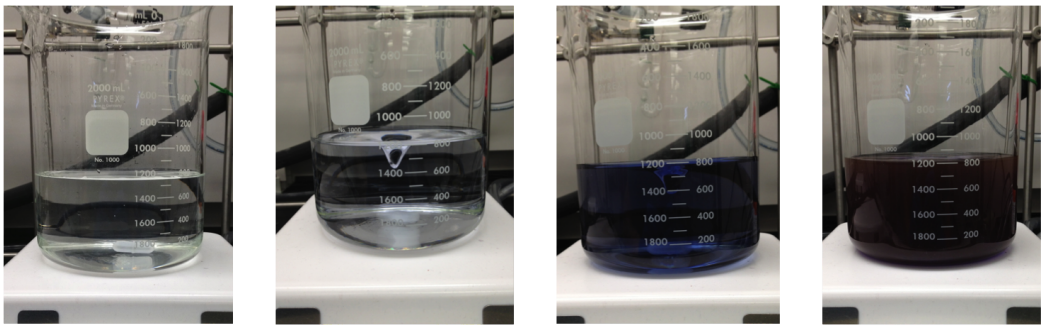

0 min ~7 min ~10 min ~15 min

3. **Washing**
   Add particles to 50 mL centrifuge tubes and centrifuge them at 1000-1200 rcf for 15 minutes. Decant, redisperse in 15 mL and repeat.

A.4 Silica Coating

A.4.1 List of Materials

- Hydrochloric acid (Sigma-Aldrich 320331)
- 0.54 wt. % aqueous sodium silicate (Sigma-Aldrich 338443)
- 1 mM (3-aminopropyl)triethyloxysilane (Sigma-Aldrich 440140)
- 30 mL washed metal nanoparticle solution (from previous section)

A.4.2 Synthesis Protocol

1. **Oil bath preparation**
   Pour silicone oil into an open top glass dish. Place the oil bath into a heating mantle, making sure that the oil bath walls make good contact with the mantle. If necessary, use heat-conducting tape. Place thermocouple in oil bath so that the tip is in solution, but not touching the glass. Set temperature controller to 90 °C. Be careful that the controller does not overshoot. If it does, stop heating until the temperature returns to approximately 90 °C. Stabilization of the oil bath at 90 °C may take up to an hour.

2. **Sodium silicate preparation (0.54 wt%)**
   Calibrate pH meter with pH 10 and pH 7 buffers. Add 2 mL of 27 wt% sodium silicate solution to a 100 mL beaker while stirring. Add 96.8 mL Milli-Q water and 1.2 mL 5 N HCl. The pH of the as prepared solution should be 10.2. If it is in the range of 10.0-10.4 use the solution as is. If it is not, use 5 N HCl (100 μL drops) to adjust the pH to 10.2. The resulting solution is 0.54 wt% sodium silicate. This solution must be freshly prepared before use. If pH is too high, ^{OH} will dissolve the silica layer, if it is too low, silica layers will grow too thick.

3. **APTES solution preparation (1 mM)**
   Mix 18.3 μL 97 wt% APTES with 100 mL milli-Q water and stir briefly. This solution must be freshly prepared before use.

4. **Gold solution preparation**
   In a 50 mL round bottom flask (single neck or three neck) add 30 mL of washed gold nanoparticle solution. The solution should be at a concentration such that the absorption peak intensity is between 1.5 and 2.5. Place a 1" stir bar in the flask as well. Make sure that all flask openings are plugged.

5. **Addition of APTES solution**
   Mount 50 mL flask above stir plate and begin stirring at roughly 300 rpm - just enough so that you can tell the gold solution is being well mixed. Add 0.4 mL of 1 mM APTES and stir for 15 minutes. Very important: Too high stirring speeds will not allow the silica to stick to the gold nanoparticles. Too low stirring will not provide the mixing required for the reaction.

6. **Addition of sodium silicate solution**
   Add 3.2 mL of 0.54 wt% sodium silicate solution to the flask and stir at room temperature for 3 minutes. Place in oil bath and continue stirring at low speed until desired thickness is reached.

   - Twenty minutes of heating results in a silica shell with a thickness of approximately 2 nm.
   - One hour of heating results in a shell with a thickness of approximately 5 nm.
   - Eight hours of heating results in a shell of approximately 10 nm thickness.

7. **Quenching the reaction**
   Once the desired silica thickness is reached, remove the flask from the oil bath. Pour the contents of the flask into two 15 mL centrifuge tubes and place in ice for five minutes.

8. **Washing and storage**
   Centrifuge for 15 minutes at 1500 rcf. Remove supernatant and redisperse in 15 mL milli-Q water. Centrifuge again for 15 minutes at 1500 rcf.

Appendix B

Fabrication of Photovoltaic Devices

B.1 Fabrication of P3HT:PCBM Organic Photovoltaics

B.1.1 List of Materials

- Indium doped tin oxide (ITO) coated glass (Thin Film Devices Inc.)
- Poly(3,4-ethylenedioxythiophene) Polystyrene sulfonate (PEDOT:PSS) in water (Heraeus)
- 0.45 micron PVDF filter (Fisher Scientific HVLP01300)
- Regio-regular poly(3-hexylthiophene-2,5-diyl) (P3HT), MW ~30,000 (Sigma-Aldrich 698989)

6,6 -Phenyl C61 butyric acid methyl ester (PCBM) (Nano-C Inc.)

- 1,2-Dichlorobenzene, anhydrous (Sigma-Aldrich 240664)
- Vacuum grade lithium fluoride
- Vacuum grade aluminum

B.1.2 Equipment

- Spin coater in normal atmospheric conditions
- Spin coater in inert atmosphere
- Hot plate
- Resistive evaporation deposition system with sample mask
- AM 1.5 solar simulator and power source
- Potentiostat or sourcemeter
- Sample mask and electrical contacts for testing

B.1.3 Fabrication Protocol

1. **Substrate Preparation**
   Begin by using as purchased 1 inch square ITO glass. Because the glass is clean upon arrival, the cleaning steps are limited to ten minutes in a plasma cleaner at medium power. This plasma treatment removes adventitious carbon from the ITO surface making the surface more hydrophilic for PEDOT:PSS deposition and improving the work function of the ITO. When purchasing ITO, pay special attention to the surface roughness; if the surface roughness is too high, it may cause shorting in the device.

2. **Buffer Layer Deposition**
   Using as purchased PEDOT:PSS, pass the solution through a 0.45 micron PVDF filter using a syringe. Before deposition, blow the substrate off with nitrogen to remove any particulate. For a 40-50 nm layer, drop 250 microliters of solution onto glass and spin coat at 500 rpm for 15 seconds to allow the liquid to spread, followed by a 30 second spin at 3000 rpm. Following deposition, anneal the film on a hot plate at 150 °C for 10 minutes to remove any water from the film. Immediately place substrate into tightly fitting petri dish, and move to an nitrogen atmosphere for further processing. The anneal and subsequent transfer to an inert atmosphere serve to ensure that all water is forced from the PEDOT:PSS film.

3. **Active Layer Deposition**
   The active layer consists of P3HT and PCBM (1:1 by mass) in 1,2-dichlorobenzene at a total concentration of 40 mg/mL. The blend should be stirred at 40 °C in the glove box overnight. Prior to spin coating, pass the mixture through a 0.45 micron PVDF filter. Drop 200 microliters of the solution onto the substrate and allow it to spread across the substrate. Spin coat using a two step process: 2000 rpm for 2 s followed by 800 rpm for 15 s. The first step removes bulk solvent, increasing overall uniformity of the film, while the second step allows for partial solvent evaporation. Immediately after spin coating, transfer the sample into a well sealed petri dish and allow it to solvent anneal. During the solvent anneal, the film turns from purple to orange, indicating that solvent is evaporating from the film. The solvent anneal is of crucial importance, as it allows for the formation of an ordered bulk heterojunction between the donor (P3HT) and acceptor (PCBM) phases. If spin coating is too long, and no solvent is left for a solvent anneal, the morphology will be finely mixed, inhibiting charge transport. If too much solvent is left after spin coating, pinholes may form in the active layer, increasing shorting in the device. After solvent anneal, thermally anneal the sample at 140 °C for 10 minutes in an inert atmosphere. Store in a dark, inert atmosphere until cathode deposition.

4. **Cathode Deposition**
   Place sample face down into evaporation mask. Using a resistive evaporator evaporate 1 nm LiF at a rate of 0.1 Å/s, followed by a 100 nm layer of Al at a rate of 1.5 Å/s.

5. **Device Characterization**

Test devices over a desired potential range (-1V:1V) under AM 1.5 conditions. Typical devices should exhibit short circuit current densities of 5-15 mA/cm^2, open circuit voltages in the range of 0.6-0.7 V and a fill factor between 0.5 and 0.7, resulting in efficiencies up to ~4%.

B.2 Fabrication of TiO_2 Water Splitting Anodes

B.2.1 List of Materials

- P25 TiO_2 powder (Sigma-Aldrich 718467)
- FTO Glass (MTI Inc.)
- Silicone paste (Sigma-Aldrich 804002)
- Triton X-100 (Sigma-Aldrich 234729)
- Isopropanol
- Acetone

B.2.2 Equipment

- Spin coater in normal atmospheric conditions
- Hot plate
- Glass flask with quartz window
- AM 1.5 solar simulator and power source
- Potentiostat or sourcemeter
- Ag/AgCl reference electrode
- Pt foil

B.2.3 Fabrication Protocol

1. **Substrate Preparation**
   Begin by using as purchased 1/2" $\times$ 1" FTO glass. Submerge FTO glass pieces in IPA/Acetone with 1wt.% Triton-X and sonicate for 30 minutes, followed by a second cycle with IPA/Acetone. Sequentially rinse with Acetone and IPA, respectively and dry under a stream of nitrogen.

2. **Calculate Metal Nanoparticle Concentration**
   A Varian Cary 5000 UV-vis NIR spectrophotometer (Agilent Technologies) with dual beam capability was used to measure the extinction of the AuNPs and Au-Ag NSs in aqueous media using a 1 cm path length cuvette. The nanoparticle size, geometry, and composition were characterized using Osiris TEM at 200 keV. In order to correlate the absorbance of nanoparticle solutions with the weight percent metal, nanoparticles of a known absorbance and volume were first dried in an oven at 70 $^{\circ}$C overnight. The mass left over from dried nanoparticles was then determined via thermogravimetric analysis (TGA), and the sample composition was analyzed. More

volatile substances (reducing agents and surfactants) evaporated, leaving only metal behind. Therefore, the fraction of mass remaining after drying was all due to the metal. TGA was conducted on Instrument Specialists TGA-1000; all nanostructures were heated to 600 °C at the rate of 20 °C min^{-1}.

3. **TiO_2 Solution Preparation**
   A solution was prepared with 3 mL ethanol, 0.1 g of P25 and varied amounts of metal nanostructures according to the previous step.

4. **TiO_2 Anode Deposition**
   The TiO_2 solution from the previous step was spin coated onto the substrate for 30 seconds at 600 rpm, followed by 60 seconds at 800 rpm. Following spin coating, anodes were annealed at 450 °C for 45 minutes to ensure that TiO_2 was fully converted to anatase phase. Any exposed FTO was coated with silicone paste to prevent any interaction with the electrochemical system.

5. **Electrochemical Characterization**
   Photocatalytic water splitting capability of anodes was tested over a potential range of -1 to 1 V at a scan rate of 50 mV s^{-1} under AM 1.5G illumination (100 mW cm^{-2}) with a Newport solar simulator and power supply. An average area of 0.2 cm^2 was illuminated. Electrochemical measurements were conducted in a three electrode setup. A Pt foil was used as the counter electrode, Ag/AgCl was used as a reference electrode. A MetroOhm PGSTAT101 potentiostat was used for all electrochemical measurements. Chronoamperometry experiments were performed at zero bias voltage, and light chopping experiments were performed by blocking the solar simulator at intervals of 10 seconds. Incident photon to charge carrier efficiency (IPCE) measurements were conducted with a Newport system with a 300W Xe light source, monochromator, and Si detector.

B.3 Fabrication of Dye Sensitized Solar Cells

B.3.1 Materials

- N-719 Dye (cis-bis(isothiocyanato) bis(2,2-bipyridyl-4,4-dicarboxylato)ruthenium(II)) (Sigma-Aldrich 703206)
- 20 nm TiO_2 Paste (Dyesol Inc. MS002010)
- 300 nm TiO_2 Paste (Dyesol Inc. MS002060)
- Scotch Tape (3M)
- FTO glass (MTI Inc.)
- Surlyn (McMaster Carr 7622A41)
- Triton X-100 (Sigma-Aldrich 234729)
- Anhydrous ethanol
- Highly boron doped Si (University Wafer)
- Titanium tetrachloride (Sigma-Aldrich 254312)
- Isopropanol
- Acetone
- Chloroplatinic acid hydraate (Sigma 254029)

B.3.2 Equipment

- Am 1.5G solar simulator
- Tube Furnace with mass flow controllers and access to Ar, H_2 and C_2H_2
- Glovebox ($<$0.5 ppm O_2)
- Electrochemical silicon etcher

B.3.3 Fabrication Protocol

1. **TiO_2 Anode Preparation**
   Anodes were fabricated by first drilling holes in FTO glass (MTI Corp.). FTO glass slides were then sonicated in successive baths of isopropanol/acetone with 1% Triton-X100 and isopropanol/acetone for 30 minutes each, respectively. Glass slides were then rinsed with isopropanol then acetone and dried with nitrogen. Glass slides were treated with 40 mM $TiCl_4$ in water for 30 min at 70 °C and then dried in air. A 10 micron thick layer of 20 nm TiO_2 nanoparticles was applied via the doctor blade

technique onto the FTO glass using one layer of scotch tape (3M) to control the thickness of the layer. TiO_2 coated anodes were annealed at 500 °C for 30 minutes in air followed by another 40 mM $TiCl_4$ treatment for 12 hours at 35 °C. This treatment is crucial to cell performance as a TiO_2 sol gel is formed and fills gaps in the mesoporous TiO_2 nanoparticle layer preventing recombination of e^-/h^+ pairs. A scattering layer comprised of 300 nm TiO_2 nanoparticles is added on top of the active layer and annealed at 500 °C. Finally, anodes were immersed in 0.6 mM N-719 Dye in ethanol overnight.

2. **Electrochemical Etching**
   Porous silicon (P-Si) etching was performed in a homemade electrochemical cell using a spiral Pt counterelectrode. Highly boron- doped (0.01-0.02Vcm) silicon wafers were utilized in an etch process of duration 180 seconds with a current density of 45 mA/cm^2 in a 3:8 v/v HF (50%H_2O by volume) and ethanol solution. The etch condition yielded ~75% porosity P-Si films confirmed by optical reflectivity measurements. Following the P-Si etch process, the samples were washed in ethanol and stored in a N_2 glove box until gas phase carbonization.

3. **C-Passivation of Porous Silicon**
   A 180 second etch process was utilized with a current density of 45 mA/cm^2 in a 3:8 v/v HF (50% H_2O by volume) and ethanol solution. This produces porous silicon materials with ~75% porosity, confirmed by optical reflectrometry, and an average pore size just under 25 nm. Porous silicon was stored under N_2 until carbonization. For C-passivation, a porous silicon wafer was placed into a tube furnace at room temperature and the furnace was evacuated to 2 mTorr. Next, 1000 sccm of Ar and 200 sccm of H_2 were introduced to the system and the furnace was ramped to T_1. T_1 was equal to 550 °C, 650 °C and 750 °C for the three different C-passivated P-Si samples respectively. The purpose of the H_2 is to maintain a reducing environment that preserves the surface stability of the unpassivated porous silicon from oxidation. Acetylene was introduced and the temperature was ramped to T_1 + 100. Ten minutes after C_2H_2 introduction, the temperature was ramped to T_1+150 for 10 minutes. This process was chosen since our observations in preliminary experiments demonstrated *(i)* porous silicon is not thermally stable without passivation above 750 °C, *(ii)* carbon coating thermally stabilizes the porous silicon up to ~1000 °C or higher, and *(iii)* the best "quality" of carbon materials based on Raman spectroscopy analysis were formed in the temperature range between 550-850 °C. Therefore, these conditions are able to optimize both the reactivity of the silicon for coating, the quality of carbon material, and the preservation of the nanoscale structure of the porous silicon after treatment. Following the second 10 minute step, C_2H_2 flow was discontinued and the sample was allowed to cool to 50 °C in an Ar and H_2 atmosphere. Samples were stored in an N_2 atmosphere until use to prevent oxidation.

4. **Electrolyte Preparation**
   The electrolyte was comprised of 50 mM I_2, 500 mM LiI and 500 mM tertbuylpyridine (TBP) in acetonitrile. The elecrtrolyte was replaced monthly and stored in a dark, inert environment.

5. **Pt Electrode Fabrication**
   Platinum cathodes were prepared by brushing 25 mM H_2PtCl_6 in isopropanol onto clean FTO glass substrates. Samples were then calcined at 450 °C for one hour

6. **DSSC Fabrication**
   The cathode and anode were heat sealed with a miniature iron and surlyn film and subsequently filled with the electrolyte. It is important that the electrode has two holes, one to inject electrolyte and the other to allow air to escape.

7. **Electrochemical Testing**
   Dye sensitized solar cells were tested over a potential range of -1 to 1 V at a scan rate of 50 mV/s under AM 1.5 illumination (100 mW/cm^2) with a Newport solar simulator and power supply. An area of 0.12 cm^2 was illuminated, the remainder was covered with a shadow mask. Cyclic voltammetry measurements were carried out in a three electrode setup using nitrogen bubbled acetonitrile which contained 0.1 M $LiClO_4$, 10 mM LiI and 1 mM I_2 as an electrolyte over a potential range of 1 to -0.8 V. A Pt foil was used as the counter electrode, Ag/AgCl was used as a reference electrode. Electrochemical impedance spectroscopy measurements were performed over a frequency range of 10^{-1}-10^5 Hz. A MetroOhm PGSTAT101 potentiostat was used for all electrochemical measurements.

8. **Material Characterization**
   An FEI Osiris TEM was used with an accelerating voltage of 200 kV for all TEM imaging. Raman spectra were gathered using a 532 nm DPSS laser in which the output power was limited to 10% (maximum output power and 50mW). The Raman scattered photons were dispersed by a 1200 lines/mm grating monochromator and collected by a CCD camera with a 50× objective lens.